



---

Graduate Theses, Dissertations, and Problem Reports

---

2025

## **Machine Learning and UASs for Managing Autumn Olive (*Elaeagnus umbellata*) on Reclaimed Surface Mines**

Sean Michael Keane

Follow this and additional works at: <https://researchrepository.wvu.edu/etd>

 Part of the [Agricultural Science Commons](#), [Forest Management Commons](#), [Other Forestry and Forest Sciences Commons](#), and the [Weed Science Commons](#)

---

Machine Learning and UASs for Managing Autumn Olive (*Elaeagnus umbellata*) on Reclaimed Surface Mines

Sean Keane

Thesis submitted to the  
Davis College of Agriculture and Natural Resources  
at West Virginia University

In partial fulfillment of the requirements for the degree of  
Master of Science in  
Energy Environments

Paul Kinder, Ph.D. (Chair)

Michael Strager, Ph.D.

Walter Veselka, M.S.

Division of Land-Grant Engagement

Morgantown, West Virginia

2025

Keywords: UAS, Remote Sensing, Machine Learning, Autumn Olive, Invasive Species, Surface Mining, Reclamation, Herbicide, Early Detection and Rapid Response (EDRR)

Copyright 2025 Sean Keane

## **Abstract**

### Machine Learning and UASs for Managing Autumn Olive (*Elaeagnus umbellata*) on Reclaimed Surface Mines

Sean Keane

This research introduces an innovative approach for managing autumn olive (*Elaeagnus umbellata*) on reclaimed surface mines through the integration of machine learning algorithms and unmanned aerial systems. The proliferation of autumn olive presents significant ecological challenges on disturbed landscapes, necessitating more efficient detection and control methods. This study evaluated Random Forest classification and deep learning approaches using the U-Net architecture for identifying autumn olive across four phenological stages using high-resolution imagery. The RGB U-Net model achieved F1-scores of 0.927, 0.912, and 0.871 for autumn olive detection during peak, late, and senescence stages respectively, outperforming both multispectral and vegetation index composite models. Temporal analysis revealed optimal detection windows during peak and late growing seasons when autumn olive characteristics diverge the most from native vegetation. Feature importance analyses identified NIR and red-edge indices as valuable for early and peak detection, while visible-band and soil-adjusted indices became important during senescence. Unmanned aerial herbicide applications demonstrated effective control with minimal impact on surrounding vegetation and reduced labor requirements. This integrated technological approach represents a promising framework for invasive species management on reclaimed mine lands, offering enhanced accuracy, efficiency and cost-effectiveness compared to traditional management practices.

## **Acknowledgements**

This graduate research was funded by the United States Department of Interior's Office of Surface Mining and Reclamation Enforcement under the Applied Science Program Cooperative Agreements Related to Coal Mining and Reclamation (Project No. S23AC00041-00).

Computational resources were provided by the WVU Research Computing Dolly Sods HPC cluster, which is funded in part by NSF OAC-2117575. I would like to thank Dr. Guillermo Avendano Franco for his assistance with using and accessing the HPC resources.

I would like to thank my committee, Dr. Paul Kinder, Dr. Michael Strager, and Walter Veselka, for their guidance and support throughout this project and my graduate studies. Their mentorship as I explored different projects and research directions laid the foundation for my graduate education.

I would also like to thank the Natural Resource Analysis Center team, past and present, Lucas, Kylie, Donnie, Isaac, Kenzie, and Matt, for their support and insights. I believe that collaboration is the true driver of progress in academic research. Working together to tackle problems and develop strategies has provided invaluable lessons. The work done at NRAC is something very special. I am grateful for my time here and I feel that our work has a meaningful impact on our state and conserving the environment around us. Additionally, I would like to thank Dr. Bob Eli, a pillar of NRAC and WVU, for his long talks and inspiring me to be a lifelong learner, a gift I greatly appreciate.

Lastly, I would like to thank my family and friends for their unwavering support throughout this journey. Their understanding of my absences, patience with my schedule, and the constant encouragement they provided pushed me to the finish line.

## Table of Contents

Abstract .....	ii
Acknowledgements .....	iii
Table of Contents .....	iv
List of Tables .....	vii
List of Figures .....	ix
Introduction .....	1
Problem Statement .....	7
Literature Review .....	9
Surface Mining .....	9
Production and Extent .....	9
Impacts .....	10
Reclamation .....	15
Forestry Reclamation Approach .....	17
Early Detection and Rapid Response .....	19
Autumn Olive .....	20
Unmanned Aerial Systems .....	22
Image Sensors .....	23
Light Detection and Ranging .....	26
Unmanned Aerial Agricultural Systems .....	28
Machine Learning .....	30
Machine Learning in Remote Sensing .....	31
Random Forest Classification .....	32
Convolutional Neural Networks .....	33
Time Series Analysis and Phenological Approaches .....	35
Explainable AI and Feature Importance .....	36
Emerging Trends .....	38
Methods .....	40
Study Area .....	40
Goshen Road .....	40
Little Indian Creek .....	41
Site Selection .....	42

Data Collection.....	43
UAS Platform and Sensors .....	43
UAS Data Collection .....	44
Image Processing.....	46
Radiometric Corrections and Photogrammetry .....	46
Vegetation Indices .....	46
Data Collection and Annotation.....	48
GPS Data Collection.....	48
Image Annotation and Datasets .....	48
Random Forest Classification .....	52
Data Preparation and Preprocessing .....	52
Multicollinearity Assessment .....	53
Phenological Stage-Specific Models .....	53
Feature Importance Analysis .....	54
Model Evaluation .....	55
Convolutional Neural Network Classification .....	56
U-Net Model Architecture and Modifications.....	56
Model Variants and Input Data .....	57
Training Process and Hyperparameter Tuning .....	59
Model Evaluation and Comparison .....	60
UAAS Treatment.....	61
Equipment and Site Selection.....	61
Flight Planning .....	62
Application Rate Testing .....	62
Herbicide Formulation.....	63
Treatment Implementation .....	64
Equipment.....	65
Results.....	67
Multispectral Reflectance.....	67
Vegetation Index Comparison.....	70
Normalized Vegetation Indices .....	70
Pearson Correlation of Vegetation Indices .....	75

Random Forest Classification .....	79
Permutation Importance .....	83
Shapley Additive Explanations .....	88
Feature Selection .....	93
U-Net Classification .....	94
Multispectral U-Net Classification .....	94
VI-Comp U-Net Classification .....	103
RGB U-Net Classification .....	112
U-Net Model Comparison .....	121
UAAS Treatment .....	124
Discussion .....	128
Conclusion .....	139
Code and Data Availability .....	143
References .....	144

## List of Tables

Table 1: Sensor Specifications .....	43
Table 2: Flight Log.....	45
Table 3: Vegetation Indices .....	47
Table 4: DJI Agras T-40 <i>Elaeagnus umbellata</i> treatment .....	63
Table 5: Early-stage random forest confusion matrix (top); Early-stage random forest performance metrics (bottom).....	81
Table 6: Peak-stage random forest confusion matrix (top); Peak-stage random forest performance metrics (bottom).....	81
Table 7: Late-stage random forest confusion matrix (top); Late-stage random forest performance metrics (bottom).....	82
Table 8: Senescence-stage random forest confusion matrix (top); Senescence-stage random forest performance metrics (bottom).....	82
Table 9: Selected vegetation indices for VI-Composite U-Net.....	93
Table 10: Early-stage Multispec U-Net confusion matrix (top); Early-stage Multispec U-Net performance metrics (bottom).....	97
Table 11: Peak-stage Multispec U-Net confusion matrix (top); Peak-stage Multispec U-Net performance metrics (bottom).....	97
Table 12: Late-stage Multispec U-Net confusion matrix (top); Late-stage Multispec U-Net performance metrics (bottom).....	98
Table 13: Senescence-stage Multispec U-Net confusion matrix (top); Senescence-stage Multispec U-Net performance metrics (bottom).....	98
Table 14: Early-stage VI-Comp U-Net confusion matrix (top); Early-stage VI-Comp U-Net performance metrics (bottom).....	106
Table 15: Peak-stage VI-Comp U-Net confusion matrix (top); Peak-stage VI-Comp U-Net performance metrics (bottom).....	106
Table 16: Late-stage VI-Comp U-Net confusion matrix (top); Late-stage VI-Comp U-Net performance metrics (bottom).....	107
Table 17: Senescence-stage VI-Comp U-Net confusion matrix (top); Senescence-stage VI-Comp U-Net performance metrics (bottom).....	107

Table 18: Early-stage RGB U-Net confusion matrix (top); Early-stage RGB U-Net performance metrics (bottom).....	115
Table 19: Peak-stage RGB U-Net confusion matrix (top); Peak-stage RGB U-Net performance metrics (bottom).....	115
Table 20: Late-stage RGB U-Net confusion matrix (top); Late-stage RGB U-Net performance metrics (bottom).....	116
Table 21: Senescence-stage RGB U-Net confusion matrix (top); Senescence-stage RGB U-Net performance metrics (bottom).....	116

## List of Figures

Figure 1: Goshen Road Reclaimed Surface Mine (left) and Little Indian Creek Wildlife Management Area (right) .....	42
Figure 2: Deep learning annotated training data .....	51
Figure 3: Deep learning 256 x 256 image and mask .....	51
Figure 4: U-Net Model Architecture .....	58
Figure 5: DJI Matrice 200 UAS .....	65
Figure 6: DJI Matrice 300 UAS .....	65
Figure 7: Sentera 6X Multispectral Sensor .....	66
Figure 8: Spectra Precision SP80 RTK GNSS Receiver .....	66
Figure 9: DJI Agras T-40 UAAS .....	66
Figure 10: Early-stage mean multispectral reflectance .....	68
Figure 11: Peak-stage mean multispectral reflectance .....	68
Figure 12: Late-stage mean multispectral reflectance .....	69
Figure 13: Senescence-stage mean multispectral reflectance .....	69
Figure 14: Early-stage mean vegetation index values .....	73
Figure 15: Peak-stage mean vegetation index values .....	73
Figure 16: Late-stage mean vegetation index values .....	74
Figure 17: Senescence-stage mean vegetation index values .....	74
Figure 18: Early-stage vegetation index correlation .....	77
Figure 19: Peak-stage vegetation index correlation .....	77
Figure 20: Late-stage vegetation index correlation .....	78
Figure 21: Senescence-stage vegetation index correlation .....	78
Figure 22: Early-stage permutation importance .....	86
Figure 23: Peak-stage permutation importance .....	86
Figure 24: Late-stage permutation importance .....	87
Figure 25: Senescence-stage permutation importance .....	87
Figure 26: Early-stage SHAP importance .....	91
Figure 27: Peak-stage SHAP importance .....	91
Figure 28: Late-stage SHAP importance .....	92
Figure 29: Senescence-stage SHAP importance .....	92

Figure 30: Early-stage Multispec U-Net loss.....	99
Figure 31: Peak-stage Multispec U-Net loss .....	99
Figure 32: Late-stage Multispec U-Net loss .....	100
Figure 33: Senescence-stage Multispec U-Net loss.....	100
Figure 34: Early-stage Multispec U-Net classification (4/13/2023).....	101
Figure 35: Peak-stage Multispec U-Net classification (7/19/2023).....	101
Figure 36: Late-stage Multispec U-Net classification (9/26/2024) .....	102
Figure 37: Senescence-stage Multispec U-Net classification (11/8/2023).....	102
Figure 38: Early-stage VI-Comp U-Net loss .....	108
Figure 39: Peak-stage VI-Comp U-Net loss .....	108
Figure 40: Late-stage VI-Comp U-Net loss .....	109
Figure 41: Senescence-stage VI-Comp U-Net loss .....	109
Figure 42: Early-stage VI-Comp U-Net classification (4/13/2023).....	110
Figure 43: Peak-stage VI-Comp U-Net classification (7/19/2023) .....	110
Figure 44: Late-stage VI-Comp U-Net classification (9/26/2024) .....	111
Figure 45: Senescence-stage VI-Comp U-Net classification (11/8/2023).....	111
Figure 46: Early-stage RGB U-Net loss .....	117
Figure 47: Peak-stage RGB U-Net loss .....	117
Figure 48: Late-stage RGB U-Net loss .....	118
Figure 49: Senescence-stage RGB U-Net loss.....	118
Figure 50: Early-stage RGB U-Net classification (4/13/2023).....	119
Figure 51: Peak-stage RGB U-Net classification (7/19/2023) .....	119
Figure 52: Late-stage RGB U-Net classification (9/26/2024) .....	120
Figure 53: Senescence-stage RGB U-Net classification (11/8/2023).....	120
Figure 54: U-Net Model accuracy .....	123
Figure 55: Autumn Olive U-Net F1-score .....	123
Figure 56: UAAS water and dye treatment (12.5 GPA) .....	126
Figure 57: UAAS Goshen Road treatment NDVI (red boxes mark targeted canopies) .....	127



## **Introduction**

Surface mining has profoundly transformed landscapes across the Appalachian region, creating extensive environmental disturbances that require careful reclamation and long-term management. These post-mining landscapes face numerous challenges, among which invasive species colonization stands as a persistent obstacle to successful ecological restoration. Autumn olive (*Elaeagnus umbellata*), an invasive shrub originally introduced for erosion control and wildlife habitat enhancement, has become particularly problematic on reclaimed mine lands throughout the region. Its aggressive growth patterns and nitrogen-fixing capabilities give it competitive advantages over native vegetation, resulting in monocultures that diminish biodiversity and hinder the development of productive post-mine land uses (Zipper et al., 2011a). Despite considerable efforts to restore these landscapes to functional ecosystems, current management approaches for invasive species like autumn olive remain labor-intensive, costly, and often ineffective over the long term.

Over the last decade, technological advancements have been developed that offer promising solutions to environmental management challenges. Unmanned aerial systems (UAS) have emerged as versatile platforms for environmental monitoring, providing high-resolution spatial and temporal data at costs considerably lower than traditional aerial or satellite remote sensing (Cromwell et al., 2021). Simultaneously, rapid developments in artificial intelligence and machine learning have transformed our capacity to analyze complex environmental data, enabling automated detection and classification of landscape features with increasing accuracy and efficiency. The convergence of these technologies presents novel opportunities for developing innovative approaches to invasive species management on reclaimed mine lands.

This research investigates the integration of UAS technology and machine learning algorithms for the detection and management of autumn olive on reclaimed surface mines in West Virginia. The study explores a comprehensive approach to invasive species management that spans from detection to treatment, combining multispectral imagery acquisition, advanced image classification techniques, and semi-autonomous UAS-based herbicide application. By leveraging the spatial, spectral, and temporal dimensions of UAS imagery through sophisticated machine learning models, this research aims to develop more accurate, efficient, and cost-effective methods for identifying autumn olive across heterogeneous post-mining landscapes. Furthermore, the study evaluates the feasibility and efficacy of unmanned aerial agricultural systems (UAAS) for targeted herbicide applications. This research explores the nexus between precision agriculture and natural resource management, potentially offering a transformative approach to invasive species control that minimizes environmental impacts while maximizing treatment effectiveness.

The significance of this research extends beyond the immediate goal of autumn olive management on reclaimed mine lands. The methods developed and evaluated in this study represent a broader paradigm shift in environmental monitoring and management, moving from labor-intensive ground surveys and manual spot treatments toward precision approaches that capitalize on cutting-edge technologies. As reclamation practitioners and land managers face increasing pressure to achieve positive restoration outcomes amid resource constraints, such technological innovations may prove critical for addressing the complex challenges of post-mining land management. Additionally, the principles and workflows established through this research may inform similar applications across different invasive species and ecological contexts, contributing to the growing field of technology-enabled environmental management.

The foundation of this research draws from multiple disciplines, including remote sensing, computer vision, machine learning, and invasive species ecology. It builds upon established frameworks such as the Early Detection and Rapid Response (EDRR) approach, which emphasizes the importance of timely identification and control of invasive species before they become widely established (Reaser et al., 2019). By enhancing the detection capabilities within the EDRR framework through advanced machine learning techniques, this research seeks to improve the operational effectiveness of invasive species management. Similarly, by evaluating UAS-based herbicide application as a rapid response mechanism, the study explores innovative technological solutions that align with existing management paradigms while addressing their limitations.

Central to this investigation is the premise that autumn olive exhibits distinctive spectral, spatial, and temporal characteristics that can be captured through multispectral UAS imagery and identified through sophisticated classification algorithms. The research explores various machine learning approaches, including traditional methods like Random Forest classification and advanced deep learning techniques such as Convolutional Neural Networks (CNNs), to determine the most effective approach for autumn olive detection across different phenological stages. This temporal dimension is particularly important given autumn olive's extended leaf-on period relative to native deciduous species, which creates potential temporal windows of opportunity for enhanced detection (Riffe, 2018).

This approach builds upon the work by Oliphant et al., 2016, who documented autumn olive's presence and proliferation on former surface mines in the Appalachian region, which highlights the need for improved detection methods as the species' presence increases. Furthermore, Huelsman et al. (2023) has demonstrated that high resolution UAS imagery significantly improves detection of invasive species as it does not require large stands of

homogenous infestation. The integration of phenological timing into our detection methods addresses the critical need for temporal flexibility in invasive species monitoring systems, particularly in heterogenous landscapes where invasive species are often interspersed within a matrix of other vegetation (Singh et al., 2024). By combining both detection and treatment capabilities, this study addresses what is recognized as the critical research gap between technological monitoring capabilities and applied field management for effective early detection and rapid response (Martinez et al., 2019).

The study is conducted at two reclaimed mine sites in Monongalia County, West Virginia. The Goshen Road site and the Little Indian Creek Wildlife Management Area. These sites represent different stages of reclamation and vegetation development, providing complementary environments for evaluating detection and treatment methodologies. By conducting research across multiple seasons and varying ecological contexts, the study aims to develop robust approaches that can be applied across the diverse conditions found on reclaimed mine lands throughout the Appalachian region.

The methodological framework of this research encompasses several interconnected components. First, extensive UAS data collection missions capture multispectral imagery across different phenological stages, creating a comprehensive temporal dataset. Second, field surveys provide ground reference data for model training and validation, ensuring the accuracy of the developed classification approaches. Third, various machine learning models are developed and compared to identify the most effective approach for autumn olive detection, with particular attention to the influence of phenological stage on detection accuracy. Finally, experimental treatments using a UAS-based herbicide application system demonstrate and evaluate the feasibility and effectiveness of this novel approach for autumn olive control.

Beyond its methodological contributions, this research addresses several practical challenges facing reclamation practitioners and land managers. The high costs and labor requirements of traditional invasive species management often limit the scale and frequency of control efforts, resulting in persistent invasions that undermine reclamation success. By developing more efficient detection methods and exploring automated treatment approaches, this research seeks to enhance the cost-effectiveness and scalability of autumn olive management. Furthermore, these targeted treatments minimize herbicide use and environmental impacts, this study aligns with growing emphasis on environmentally safe and sustainable land management practices.

The findings of this research have potential applications across multiple domains. For reclamation practitioners, the developed methods offer new tools for monitoring and managing invasive species on post-mining landscapes. For regulatory agencies, improved detection capabilities can enhance compliance monitoring and assessment of reclamation success. For ecological researchers, the high-resolution temporal data and classification results provide insights into invasion dynamics and species interactions on disturbed landscapes. Additionally, the technical workflows and algorithms developed through this research contribute to the rapidly evolving fields of environmental remote sensing and applied machine learning.

Through this comprehensive investigation of UAS and machine learning applications for autumn olive management, this research contributes to the ongoing evolution of post-mining land management approaches. By bridging technological innovation with ecological understanding, the study aims to enhance our capacity to address one of the most persistent challenges facing reclaimed mine lands, which is the control of invasive species that impede the development of diverse, functional, and sustainable post-mining ecosystems. In doing so, it exemplifies how

emerging technologies can be harnessed to address long-standing environmental challenges, potentially transforming how we approach ecological restoration in human-altered landscapes.

## **Problem Statement**

Surface mining operations have dramatically transformed landscapes across the Appalachian region, creating extensive environmental disturbances that require ongoing management. In the Central Appalachian region alone, surface mining has affected approximately 5,900 km<sup>2</sup> of land between pre-1976 and 2015, representing 7.1% of the regional area (Pericack, 2018). Despite reclamation efforts mandated by the Surface Mining Control and Reclamation Act of 1977, these altered landscapes remain vulnerable to invasive species colonization, which threatens the long-term success of restoration initiatives.

Autumn olive (*Elaeagnus umbellata*), originally introduced for erosion control and wildlife habitat enhancement, has become particularly problematic on reclaimed mine lands (Franke et al., 2018). Studies have documented autumn olive coverage reaching 12.6% of surface-mined areas in southwestern Virginia (Oliphant et al., 2016), with volumes exceeding five times that of all other tree species combined in some locations (Evans et al., 2013). Its nitrogen-fixing capabilities, extended growing season, and prolific seed production give it competitive advantages over native species in the nutrient-poor conditions common on reclaimed sites (Brym et al., 2011). Once established, autumn olive forms dense monocultures that inhibit native forest regeneration and diminish the ecological and economic value of reclaimed lands.

Current management approaches for autumn olive are labor-intensive, costly, and often ineffective (Byrd et al., 2012). These substantial financial and logistical burdens are compounded by the challenges of detecting and monitoring autumn olive across extensive, steep, and often remote mine lands. Traditional ground surveys miss early-stage invasions in inaccessible areas, while conventional remote sensing typically lacks the spatial resolution necessary to identify individual shrubs or small patches in heterogeneous post-mining landscapes.

Recent technological advancements in Unmanned Aerial Systems (UAS) and machine learning offer promising opportunities to address these challenges. UAS platforms equipped with high-resolution multispectral sensors can capture detailed imagery at centimeter-level resolution, potentially enabling the detection of individual autumn olive shrubs across large areas. Machine learning algorithms can analyze this imagery to automatically identify invasion patterns, particularly when leveraging spectral differences or temporal changes in vegetation characteristics. Furthermore, UAS-based herbicide application systems could enable targeted treatment with reduced labor requirements and drift to non-targeted or desired species.

This research addresses critical knowledge gaps by developing and evaluating an integrated approach for autumn olive detection and management on reclaimed surface mines. By investigating the performance of various machine learning algorithms with multispectral UAS imagery across different phenological stages, this study aims to identify optimal detection methods to inform management decisions. Additionally, by testing UAS-based herbicide application, the research explores a novel treatment approach that could significantly reduce the costs and environmental impacts of autumn olive control, ultimately supporting the restoration of these disturbed landscapes to functional, diverse ecosystems.

## **Literature Review**

### **Surface Mining**

Surface mining, the process of extracting minerals near the Earth's surface by removing the soil and rock overlying the mineral deposits, is the most widely employed and extensive methods of coal extraction in the United States (EIA, 2024). The first reported coal production using surface mining in the U.S. occurred in 1914 (Zipper, 2020), though it was not until after World War II that it became more widely adopted. Following the advances in machinery during World War II, surface mining became more efficient, and machines were able to traverse difficult terrain, expanding its use, especially in the eastern U.S. (Zipper et al., 2020). Mountaintop removal (MTR) is a particularly impactful form of surface mining commonly used in the Appalachian region, where entire mountaintops are removed to access coal seams. This often involves deforesting, blasting, and then excavating soil and rock, shaving down the ridgeline to expose the underlying coal seam. From its inception, surface mining and MTR proved to be more efficient than underground mining, with the ability to recover more than 90% of the coal seam (National Research Council, 2007) and mitigates many risks that miners are exposed to underground (MSHA, 2022). Additionally, surface mining operations can be conducted more rapidly and cost-effectively compared to underground mining.

### *Production and Extent*

As of 2022, surface mining produced over 372 million short tons of coal, or 62% of the total U.S. coal production (EIA, 2024, Table ES-1). It has surpassed annual U.S. underground coal mining production since 1974 and peaked in 2008, producing a total of 814 million short tons of bituminous, subbituminous, lignite, and anthracite coal (EIA, 2024, Table ES-1). During the peak years of U.S. coal production, the total area of surface mines in the U.S. increased from 8,324 km<sup>2</sup>

in 2001 to 9,181 km<sup>2</sup> in 2006. This is an expansion rate of ~2% annually (Soulard et al., 2016), an increase from the ~1% annual rate measured from 1973 to 2000 (Sleeter et al., 2013).

Much of the coal production through surface mining occurs in the Powder River Basin of northeast Wyoming and southeast Montana, where 15 surface mines extracted 258.4 million short tons of coal in 2022 (EIA, 2024, Table 1). In contrast, the Appalachian region, despite having 296 surface mines, produced a total of 32.5 million short tons in 2022 (EIA, 2024, Table 1). This difference is due to the presence of thick coal seams in the Powder River Basin, such as the 19.5-meter thick Wyodak coalbed. The Appalachian region has much thinner seams, like the 2-meter-thick Pittsburgh coalbed (EIA, 2024, Table 5). Thin seams require more extensive mining operations to extract through the region's complex geology, which increases extraction costs and reduces productivity per mine. However, the increase in costs is offset by the presence of more valuable metallurgic bituminous coal. The footprint of this quantity of surface mines has altered a large extent of the Central Appalachian region, an area comprised of parts of West Virginia, Virginia, Kentucky, and Tennessee (Zipper et al., 2020). This region had an average of 87 km<sup>2</sup> of unmined land that was converted into a surface mine annually between 1985 and 2015, a total of 2,900 km<sup>2</sup>. From pre-1976 to 2015, the cumulative area of the Central Appalachian region that has been surface mined is 5,900 km<sup>2</sup>, or 7.1% of the 83,000 km<sup>2</sup> study area (Pericack et al., 2018).

### *Impacts*

Surface mining activities cause profound adverse environmental impacts, including extensive deforestation and fragmentation, disruption of carbon and nutrient cycling, degradation of watershed quality, and risks to public health (Palmer et al., 2010; Bernhardt and Palmer, 2011). These issues are particularly acute in the Appalachian region, as it is host to the world's most extensive deciduous forest (Riitters et al., 2000) that is amongst the most biodiverse in the

temperate regions (Ricketts et al., 1999). In the Central Appalachian region, the temperate climate and varied topography resulting from differential erosion of sedimentary rock supports nearly 40 commercially important tree species and a diverse understory of grasses and herbs (Ricketts et al., 1999). The region is characterized by interior forests, which are extensive and relatively undisturbed by other land uses (Riitters et al., 2002). These forests are not only rich in biodiversity, but also provide carbon storage, watershed and water quality protection, and habitat for flora and fauna (Wickham et al., 2013). However, the fragmentation of interior forests and subsequent creation of edge forests change the structure, composition, and ecological processes of ecosystems (Wickham et al., 2006). Edge forests exhibit increased rates of atmospheric decomposition (Weathers et al., 2001) and have a higher proportion of non-native, invasive species (Harper et al., 2005). The impact of surface mining on interior forests has been disproportionate relative to the direct forest loss caused by the practice, with interior forest loss occurring at rates 1.75 to 5 times greater than the direct forest loss between 1992 and 2001 (Wickham et al., 2006).

Mountaintop removal method can reduce the elevation of ridgelines by over 100 meters (Ross et al., 2016). During the excavation of the topsoil and overburden (rock and soil overlying the coal seam), some of the material is used in an attempt to rebuild the original contour or some alternative for designated post-mine land use. Additional excess overburden is used to create valley fills, a wedge-shaped feature that is constructed in valleys that are adjacent to and topographically below the mine site (Skousen and Zipper, 2020). Valley fills can range in sizes, depending on the use of the overburden extracted. One valley fill was identified in West Virginia as  $2.9 \text{ km}^2$  in area and a max depth of 184 meters, holding over 200 million  $\text{m}^3$  of overburden (Ross et al., 2016). They are constructed in such a way that large boulders or rock drains create a porous structure and allows water to drain into containment ponds (Hester et al., 2019). This method of managing excess

overburden buries aquatic ecosystems and has led to a net loss of 4,000 km of headwater streams, significantly impairing their ecological and hydrological functions downstream (U.S. EPA, 2011)

The natural topography of the Central Appalachian region is formed by dissected step slopes and valleys. The soil on these steep slopes is thin and often less than 1 meter in depth (Haering et al., 2004). Following MTR, the mined land is dramatically transformed into upper slopes, moist flats, and flat summits. This is a significant reduction in the topographic complexity and creates plateau-like environments, reducing the median slope within one area of the Central Appalachian region by 10 degrees (Maxwell and Strager, 2013; Ross et al., 2016). In the mining and construction of these plateau environments, surface soils may be constructed from salvaged native soils, but it is more common for weathered soils and course fragments to be used as a substitute in the Appalachian region (Zipper et al., 2011a). These soils can become highly variable on site with both compaction and loose, porous material (Greer et al., 2017) with a change in bulk density from 1.1-1.5 g/cm<sup>3</sup> measured in natural soils to greater than 2 g/cm<sup>3</sup> in mined soils (Zipper et al., 2011a). While compaction may be necessary for post-mine development, it is a significant inhibitor to post-mine lands that are designated for forestry and ecosystem development. Excessive compaction can impede root extension of vegetation and restrict movement of water and air, leading to a state of arrested succession (Skousen et al., 2020).

The presence of both highly compacted and porous surfaces on MTR sites can cause precipitation to either infiltrate the surface or be routed overland along new flow paths. This variability in compaction leads to variable infiltration, with rates of 10 meters an hour to less than one meter per day (Hester et al., 2019). On compacted surfaces, slow infiltration of precipitation can increase flow peaks and delay hydrologic response time. This behavior is more similar to impervious urban areas than unmined soils (Evans et al., 2015). On porous surfaces, water can

infiltrate into unconsolidated aquifers or cavities created by large boulders. This abundance of groundwater retention results in higher baseflows that are sustained even through drought (Nippgen et al., 2017). However, minerals present in overburden, such as pyrite and other metal sulfides, can leach into the groundwater and negatively impact downstream water quality, leading to acid mine drainage. Acid mine drainage severely degrades water quality by lowering pH to as acidic as 2.8 and increasing the concentration of metals. These effects can cause a decline or local extinction of macroinvertebrate and fish populations (Daniels et al., 2020).

Further impacted by compaction, the re-establishment of vegetation on post-mine lands can be difficult and slow. Amongst other variables, such as topsoil substitutes, depletion of seed banks, and introduction of non-native ground cover, can cause re-establishing forests to experience a chronic state of arrested succession (Cavender et al., 2014). The choice of overburden material used for topsoil substitutes, weathered brown sandstone or unweathered gray sandstone, can have a significant impact on forest succession. In an 11-year study, red oak (*Quercus rubra*), white oak (*Quercus alba*), and tulip poplar (*Liriodendron tulipifera*) planted in gray sandstone exhibited little to no growth. Whereas red and white oaks in brown sandstone grew at about 50% of the new growth in unmined, native soils. Tulip poplar had 30-40% of the growth rate of unmined, native soils (Dallaire and Skousen, 2019). This is largely due because of the lowered pH, similar to native soils, and increased water retention properties in brown sandstone, which is caused by the higher amount of clay present (Sena et al., 2014). When vegetation growth was compared in Central Appalachian mined and unmined forests from 1985 to 2015, only 7.9% of surface mines recovered during this period, and less than 1% is expected to continue to recover (Thomas et al., 2022). Surface mining is the leading cause of deforestation in the Appalachian region (Drummond et al., 2010), and the resulting loss and stunted growth of forests have significant ecological impacts. On

mine sites, carbon pools can shrink and reduce carbon sequestration by 30-44% (Amichev et al., 2008). Furthermore, the altered landscapes are highly susceptible to colonization by non-native grasses and shrubs, reducing native biodiversity and hindering re-establishment of desired and native vegetation species (Wickham et al., 2013).

Non-native and invasive species colonization is extremely prevalent on former surface mines. The U.S. government defines invasive species as a “non-native organism whose introduction causes, or is likely to cause, economic or environmental harm, or harm to human, animal, or plant health” (Executive Office of the President, 2016). Their introduction on mine sites originates from either intentional plantings or as volunteer species from adjacent sites (Ross et al., 2021). Seed mixes used to establish ground cover often contain competitive grasses and legumes, such as tall fescue (*Festuca arundinacea*) and sericea lespedeza (*Lespedeza cuneata*) on a site in southeast Ohio (Cavender et al., 2014). Tree-of-heaven (*Ailanthus altissima*), autumn olive (*Elaeagnus umbellata*), and glossy buckthorn (*Frangula alnus*) which are invasive, are also planted on mine sites or are dispersed and colonize from nearby disturbed land (Sena et al., 2020). Some native species to the Appalachian region, like the black locust (*Robinia pseudoacacia*), are considered to be invasive due to their rapid growth and nitrogen-fixing capability which allow non-native grasses to persist and outcompete other native species (Groninger et al., 2007). The spreads of invasive species lead to the development of monocultures that not only reduce biodiversity but can also attract foreign pests, placing more stress on the survivability of native species (Evans et al., 2013). Non-native and invasive species, including black locust, are the dominant woody material on former surface mines. As a result, the establishment of pre-mine forests is delayed, prolonging recovery and requiring more human intervention in the environment (Ruggles et al., 2021).

## **Reclamation**

As the increase in surface mining continues, the amount of land that is left permanently altered will also continue to increase. In order to convert surface mines into productive land after mining has been completed, mining companies have the responsibility of reclaiming the land to a state that can support post-mine land uses similar to or better than the original use (Skousen and Zipper, 2014). Surface mine reclamation is the process of reconstructing the landscape to the approximate original contour of the original environment, revegetating the mine site, and mitigating any environmental impacts (Skousen and Zipper, 2020). It has been federally required for coal mining since the passage of the Surface Mining Control and Reclamation Act of 1977 (SMCRA). However, Appalachian states passed reclamation laws as early as 1939, generally requiring covering excavated areas with soil or overburden, grading, and revegetating the site (Plass, 2000). With the establishment of federal oversight, SMCRA mandates that coal mine operators obtain permits which detail performance standards are required to meet in order for the site to be considered reclaimed. These standards require that vegetation is established to effectively control erosion, stabilize the land, and establish an approved post-mining land use. Reclaimed surface mines must also ensure proper drainage and avoid exposing acid-forming or other toxic overburden that would impair revegetation or water quality (Skousen and Zipper, 2014). Additionally, all water leaving the mine site must comply with the water quality standards of the Clean Water Act. Similarly, if protected species are present in the permit area or affected waters, compliance with the Endangered Species Act is also required (Skousen and Zipper, 2020).

Much of the land surface mined in the Appalachian region previously supported forest and agriculture. However, reclamation can develop the land to a “higher and best use” including industrial, commercial, or residential developments (Skousen and Zipper, 2020). Post-mine land

uses that require management are generally considered to be “higher use”, such as pastureland. While wildlife habitat and forests are seen as less productive, approximately 150 million trees have been planted on about 810 km<sup>2</sup> of reclaimed mine land between 2004 and 2020 in Appalachia. In 2020, almost 92 km<sup>2</sup> were released from Phase III bonds, meaning that revegetation success standards were met (OSM, 2020 annual report). From 1978 to 2019, an average of 170 km<sup>2</sup> were released from Phase III bonds (Zipper, 2020). As of 2010, wildlife habitat and forests accounted for 60% of reclaimed mines in Appalachia. Altogether, wildlife habitat, forest, and pastureland make up 95% of the reclaimed land in the Appalachian region in 2010 (OSMRE, 2010). However, because SMCRA emphasizes erosion control and soil stabilization, requiring extensive grading to achieve the approximate original contour, the soil can become significantly compacted (Greer et al., 2017; Skousen et al., 2020). Since soil compaction is a contributing factor in the development of the arrested early successional ecosystems (Cavender et al., 2014), many mine operators turn to pasturelands as the targeted reclaimed state. However, of the 3,000 km<sup>2</sup> reclaimed between 1980 and 1995 in the Appalachian region, very few were used as their intended post-mine land use. Due to the remoteness of former surface mine sites and lack of water for livestock, these areas were rarely grazed and overwhelmed with invasive species within 10 years of reclamation (Whittier et al., 2010; Burger et al., 2011).

The value and quality of reclaimed mines became a concern in the mid-1990s and in response, reclamation in the Appalachian region was permitted to be designated as wildlife habitat and unmanaged forest (Burger, 2011). As SMCRA’s standards leaned towards mitigating short-term soil erosion rather than long-term ecological functions, these post-mine land uses were achieved by planting early successional and non-native species that can withstand the disturbed conditions (Zipper et al., 2011b). Non-native tree species preferred by mine operators were autumn

olive (*Elaeagnus umbellata*), glossy buckthorn (*Frangula alnus*), tree-of-heaven (*Ailanthus altissima*), and empress tree (*Paulownia tomentosa*). Other non-native and invasive plants common on these reclaimed sites are Japanese honeysuckle (*Lonicera japonica*), various *Lespedeza* species (Zipper et al., 2011a; Cavender et al., 2014; Oliphant et al., 2016; Sena et al., 2020; Ruggles, et al., 2021), and multiflora rose (*Rosa multiflora*) due to its “wide environmental tolerance” (Wade et al., 1985). Despite current guidelines discouraging the planting of these species, their establishment often occurs through volunteer spread from nearby reclaimed or abandoned mine land where invasive species are already present (Burger et al., 2011). Proliferation and seed dispersal stems from wind, wildlife, water, and root propagules (Adams et al., 2019). A study in southwestern Virginia found that volunteer species represented 65% of the total tree volume on a reclaimed surface mine. Non-native and invasive species made up more than 5 times the volume of native volunteer species (Evans et al, 2013).

#### *Forestry Reclamation Approach*

In response to degraded post-mine land use value on areas reclaimed as forests and wildlife habitat, the Appalachian Regional Reforestation Initiative (ARRI) was formed in 2004. The cooperative effort between states in the Appalachian region and the Dept. of Interior’s Office of Surface Mining Reclamation and Enforcement (OSMRE) was to promote high-value forest reclamation. From this, a series of advisories for reclaiming cost-effective, productive, and native forests were outlined in the Forestry Reclamation Approach (FRA) ( et al., 2005). The FRA uses five steps to achieve this goal: (1) create a suitable rooting medium with topsoil, weathered sandstone, or best available material; (2) loosely grade the topsoil or substitute to reduce compaction; (3) establish ground cover that minimizes competition; (4) plant both early

successional species and commercially valuable late successional tree species; and (5) use proper planting techniques (Burger et al., 2005; Zipper et al., 2011b).

An emphasis is placed on soil reclamation, preferably with native topsoil, weathered brown sandstone, or a mix of the two (Sena et al., 2014; Dallaire and Skousen, 2019). Grading of the surface should be minimal to avoid compacting the surface and the advisory guideline is for rooting mediums to have a minimum depth of 1.2 meters (Burger et al., 2005). To reduce competition with native pioneers, FRA establishes vegetation cover with grasses and legumes like perennial ryegrass (*Lolium perenne*) and birdsfoot trefoil (*Lotus corniculatus*). Though these species are non-native, they are slow-growing, tolerant of a range of soil conditions, and require less nutrients and water (Burger et al., 2009). While each site has its own considerations for selecting tree species; ground cover, early successional and late successional species can be planted simultaneously. Early successional trees chosen are fast-growing species like black locust, pines, bigtooth aspen, red maple, and hawthorn. Late successional trees, such as American beech, hickories, sugar maple, and oaks, are heavy seeders that promote natural succession and hold commercial value (Groninger et al., 2007; Davis et al., 2012).

Though the implementation of FRA is young, recovery rates are promising and appear to reach a higher level of recovery (Thomas et al., 2022). The guidelines have shown to decrease soil bulk density, increase survivability, and increase available nutrients on sites (Phillips et al., 2021). While FRA has been successful at reclaiming native forests with the use of non-native low vegetation, the presence of invasive species is a common concern on FRA sites and future monitoring is necessary to understand limitations (Fields-Johnson et al., 2012; Franklin et al., 2012).

### *Early Detection and Rapid Response*

The Federal Interagency Committee for the Management of Noxious and Exotic Weeds first published the concept for the Early Detection and Rapid Response (EDRR) program in 2003. The early idea of EDRR was focused on identifying preventative measures at a species-specific level.(Federal Interagency Committee for the Management of Noxious and Exotic Weeds, 2003). The concept was later refined and standardized by Reaser et al., 2019 as a “guiding principle for minimizing the impact of invasive species in an expedited yet effective cost-efficient manner”. The goal of the EDRR program is dynamic, where detection of invasive species is done through observations and documentation, and response to invasions can involve further analysis, eradication, or containment (Reaser et al., 2019). Implementing EDRR involves a non-linear and iterative process for identification, reporting, screening, and control, with each action requiring expert validation. This is meant to ensure that best practices are applied to individual species management and facilitates clear communication between multiple authorities (Wallace et al., 2019).

The most recent outline of EDRR introduces feasibility screening and target analysis. Unlike risk screening, which is used to determine the level of response needed for an individual invasion, feasibility screening is a measurement of the ability and likelihood of successfully responding to invasions. This includes financial, technological, legal, and human restraints (Marshall Meyers et al., 2019; Reaser et al., 2019). Target analysis is a key component of EDRR guidance and can significantly improve the measure of risk and feasibility of response success. It is a strategic approach for detecting invasive species at a specific site and time, using a particular method and technology. Detection with target analysis uses modeling, mapping, and computational resources to maximize efficiency and cost-effectiveness (Morisette et al., 2019). Advances in

technology will further improve detection with target analysis. The use of unmanned aerial systems (UAS), or drones, can expand surveillance capabilities and can be equipped with high resolution image sensors. Data collected with UASs can be analyzed with machine learning using advanced statistical techniques to identify targeted species. Along with geographic information systems (GIS), advanced technologies can be used as accurate decision support tools for controlling invasive species (Martinez et al., 2019).

### **Autumn Olive**

Autumn olive (*Elaeagnus umbellata*) is one of the most common species on former surface mines in the Appalachian region (Zipper et al., 2011b). Autumn olive was first introduced in the U.S. in 1830 as an ornamental species (Dirr, 1983) and was later used as erosion control on surface mines beginning in the 1960s (Thompson et al., 1984). It is large shrub native to Asia that can quickly grow up to 5 meters tall with a dense, 6-meter-wide crown. (Black et al., 2005). Beyond erosion control, the species can rapidly establish vegetation cover and soft mast for wildlife, producing up to 24,000 seeds per mature plant annually (Ahmad et al., 2006). The red fruit, in the form of drupes, can produce 14 kilograms per plant and are able to persist into the winter, providing nutrients to wildlife on disturbed sites that otherwise would be scarce (Lituma et al., 2020).

The prolific spread of autumn olive is aided by traits associated with reclaimed surface mines (Zipper et al., 2011a). Autumn olive thrives on weathered brown sandstone, a common challenge as it is the preferred FRA substitute for topsoil, and low-competition or barren environments (Franke et al., 2018). While low levels of nitrogen and other nutrients on reclaimed mine sites inhibit native plant growth, autumn olive is able to rapidly colonize due to its nitrogen fixing ability (Brym et al., 2011). In the eastern U.S., the leaf-on period can begin in March and last until late November. This is an extended growing period relative to native species and allows

understory growth to thrive in relative phenology of autumn olive is different relative to native species. (Riffe, 2018). These traits provide numerous advantages for autumn olive to outcompete and hinder the establishment of native species, especially in nutrient deficient and disturbed land. From 1984 to 2011, autumn olive was found to cover 12.6%, or 3,823 hectares of the 30,285-hectares surface mined in the southwestern Virginia study site (Oliphant et al., 2016). On a nearby 35-acre site, autumn olive made up 27% of the canopy cover and had a mean volume of 14.64 m<sup>3</sup> per hectare, five times all other tree species combined (Evans et al., 2013).

Controlling autumn olive on reclaimed landscapes is essential for native and productive forest recovery (Zipper et al., 2011b; Reaser et al., 2019). Eradication, which is generally necessary for control of autumn olive, can be difficult due to autumn olive's rapid proliferation and requires tremendous amount of time and expenses (Adams et al., 2019). On a reclaimed surface mine in southeast Ohio, moderate invasions (15-30% canopy cover) of autumn olive were successfully treated with a foliar herbicide application via a backpack sprayer at \$741 per hectare and averaged two hours per hectare. In cases of more severe invasions (95-100% canopy cover), mechanical methods may be necessary, such as cut-stump herbicide treatment and mulching. Autumn olive at this density limits eradication success and costs up to \$1,166 and 6.5 hours per hectare. These efforts must be continued iteratively due to incomplete foliar coverage and resprouts, requiring long-term management plans (Byrd et al., 2012). However, some reclamation sites with autumn olive present have shown improved growth in native hardwood species (Franke et al, 2018; Lemke et al., 2013). This is likely due to the species nitrogen fixing ability, which increases available nitrogen in surrounding soil and causes autumn olive to act as a nurse species for invasive and native trees (Lemke et al., 2013). Despite the need for further research to fully understand the effects of autumn olive on reclaimed surface mines, their presence is considered to be invasive and

undesirable, especially on post-mine lands that are used for forestry, wildlife habitat, and recreational purposes (Li et al., 2018).

## **Unmanned Aerial Systems**

The development of unmanned aerial vehicles (UAV), commercial drones, or unmanned aerial systems (UAS) has provided a cost and time efficient solution to collecting high-resolution remotely sensed imagery. UASs have aided researchers and reclamation managers with pipeline inspections (Mesa et al., 2023), sediment control (Strager et al., 2020), assessing forest recovery (Paudel et al., 2024), and monitoring invasive species (Baron et al., 2018). The use of fixed-wing, single and multi-rotor UASs can reduce costs, risks, and limitations of other remote sensing sources like satellite and aerial. When equipped with multispectral, hyperspectral, and LiDAR sensors, UASs are able to capture data with more efficiency and at a much higher resolution, at the expense of flight range (Wargo et al., 2014). Spatial resolutions of UAS acquired data can be very fine, with centimeter to sub-centimeter scale ground sampling distance (GSD) (Fraser et al., 2018). Research studies and environmental monitoring have increasingly used UASs for data collection and vegetation assessments. Data collected can be used for image transformations and photogrammetry, allowing users to generate indices across sites for analyzing vegetation features, watersheds, and tree growth. UASs are also commonly equipped with global positioning systems (GPS) that allow data to be geographically referenced and used in GIS and spatial statistical analysis (Cromwell et al., 2021).

While the wide adoption of UAS technology has generated a new depth to ecological studies, there are still limitations to their use (Tmusic et al., 2020). Implementing UAS can be cost-effective for projects and organizations planning to use it in the long-term, though the initial purchases can be expensive. Open-market UAS platforms can cost \$1,200 to more than \$15,000,

and high-resolution sensors can cost between \$400 and more than \$16,000 (Lachowiec et al., 2024). Those who are operating a UAS that weighs more than 250 grams must register the drone with the Federal Aviation Administration (FAA) and obtain a Part 107 Small Unmanned Aerial Systems (sUAS) Certificate. The FAA regulates the use of UAS and prohibits flights above 400 feet above ground level (AGL), unless they are inspecting a building or communications tower. Also, flights beyond the pilot's or visual observer's line of sight and operating in a controlled airspace without a Low Altitude Authorization and Notification Capability (LAANC) approval. For specific or non-standard operations, such as flying at higher altitude, beyond visual line of sight, or in restricted areas, a Certificate of Authorization (COA) may be necessary. Moreover, when conducting UAS operations that may interfere with other aircraft, or as required by an issued COA, a Notice to Airmen (NOTAM) may be required to notify other airspace users of the UAS activity. Depending on the flight operation, pilots may also be required to have insurance, submit petitions for exemption for operations not explicitly outlined under Part 107 and comply with personal privacy laws (FAA, 2016; FAA, 2025).

### *Image Sensors*

Many UASs come equipped with a first-person view (FPV) camera to provide the pilot with a real-time video of the flight, and a gimble mount for equipping more advanced sensors. In research applications, UASs utilize image sensors that are similar to those aboard satellites and manned aircraft, these include true color composite (RGB), multispectral, hyperspectral, and thermal sensors. These passive sensors capture the natural radiation that is emitted or reflected by objects in the electromagnetic spectrum (Padua et al., 2017). Visible light is reflected in the approximate wavelength range of 400 to 700 nm, near infrared light (NIR) is captured from 700 nm to 1,000+ nm, and thermal imagery uses shortwave infrared light (SWIR) from 1,000 nm to

2,500 nm (UNBC GIS Lab, 2024). RGB cameras, which capture visible light, are the most common choice for UAS surveys. These sensors are sufficient for many applications, though primarily land mapping and infrastructure inspections (Colomina and Molina, 2014). However, with the development of modular, affordable, and high-resolution RGB cameras, their use in vegetation studies is becoming more common and has greater success. For example, researchers have used an integrated consumer-grade drone and RGB camera to generate orthomosaic images with a resolution of 3.59 cm/pixel. They were then able to delineate individual red spruce canopies and measure variations in regeneration (Harris et al., 2022). Other research has made up for the limited spectral range of RGB imagery by using image processing techniques such as color thresholding, template matching, and de-speckling. This has enabled RGB cameras to accurately classify invasive yellow flag iris flowers approximately 8 cm in diameter (Baron et al., 2018).

Multispectral cameras capture the reflectance in discrete and fine spectral bands across the electromagnetic spectrum, including blue, green, red, NIR, as well as additional bands like red-edge. Captured digital number (DN) values can be calibrated with reflectance pads and irradiance sensors, then converted into reflectance values for accurate spectral analysis and interpretation (Suomalainen et al., 2021). In leafy vegetation, the visible spectrum has a minor peak of green reflectance but is otherwise heavily absorbed in the red and blue regions for photosynthesis by the plant pigments chlorophyll, carotenoids, and anthocyanins. However, NIR reflectance in leafy vegetation is particularly high in the range of 700 nm to 1,400 nm. This reflectance is due to a scattering effect caused by the internal leaf structure, presence or absence of pigment coloration, and the thickness of the leaf cuticle. A decrease in chlorophyll results in an increase of red and NIR reflectance, shifting chlorophyll absorption to shorter wavelengths in the visible range (Ustin et al., 2020). The water content of leaves is another component influencing the reflectance properties

of vegetation. Although NIR light is absorbed by water, water content in leaves can be measured through increases in absorption, especially at 1,450, 1,940, and 2,500 nm, with minor effects at 400 nm and 700 nm. These properties can be used to measure senescence, changes in health of vegetation, and environmental stressors (Seelig et al., 2008). Likewise, some soil properties have unique reflectance properties that can be detected with multispectral sensors. Soil moderately reflects visible light and increasingly reflects infrared light up to 2,500 nm due to iron oxides and organic matter. As organic matter in soil increases, reflectance decreases in the 400 to 1,000 nm range, whereas soils with low levels of organic matter exhibit higher reflectance in this range (Ustin et al., 2020).

Given the distinct spectral properties associated with chlorophyll, water content, and soil, researchers have developed numerous spectral indices by calculating raster pixels. to monitor and assess the environment. Several indices commonly used to monitor vegetation include the normalized difference vegetation index (NDVI), visible atmospherically resistant index (VARI), soil adjusted vegetation index (SAVI), normalized red and green difference index (NGRDI), normalized difference water index (NDWI), and many others (Ollinger, 2010). Examples of their use have become more common as UASs and multispectral sensors are more available to researchers. For instance, one study sought to classify the health of a mixed deciduous and coniferous forest using UAS multispectral imagery and National Agricultural Imagery Program (NAIP) aerial imagery. They determined that NDVI and NGRDI provided the most important feature in their classification model, which achieved 70% in aerial imagery and 72% in UAS imagery (Fraser and Congalton, 2021). Another study used 26 vegetation indices from UAS multispectral imagery to predict the yield of corn. The effectiveness of these indices varied across different phenological stages, but many proved to be strong predictors of yield, with an R-squared

value of 0.90 or higher. Among these, the SAVI, VARI, green leaf index (GLI), and the simplified canopy chlorophyll content index (SCCCI), which divides NDRE by NDVI, all demonstrated the highest predictive power (Barzin et al., 2020). Image sensors, including both RGB and multispectral, offer high-resolution imagery when utilized with UASs, providing significant flexibility for temporal, spatial, and spectral research in agriculture and forestry.

### *Light Detection and Ranging*

Light Detection and Ranging (LiDAR) is an active sensing technology that uses a scanning transmitter to emit pulses of light, which then reflect off surfaces and return to the receiver. By calculating the distance the laser pulse travels from the reflecting feature and back to the receiver, LiDAR is capable of generating a detailed point cloud of the terrain and features of a landscape. With the integration of GPS and an inertial measurement unit (IMU), each point in the cloud can be georeferenced with a high degree of accuracy (Mehendale and Neoge, 2020). These point clouds can be classified into digital elevation models (DEM), These include digital surface models (DSM), which include all features above the surface, such as trees and buildings, and digital terrain models (DTM), which is the bare surface topography (Rogers et al., 2020). UAS LiDAR-derived DEMs are high resolution and can be classified for use in a range of tasks, including utility vegetation management, forest structure analysis, measuring vegetation growth, as well as geomorphological and hydrological analysis (Wallace et al., 2012; Walker and Dahle, 2023; Paudel et al., 2024). Similarly, elevation models can be generated with overlapping imagery. Photogrammetry processes use structure-from-motion (SfM) and dense image algorithms to create three-dimensional point clouds from images (Schonberger et al., 2016). In less complex landscapes, SfM with high resolution imagery can generate point clouds that are of equal or greater quality to density of LiDAR point clouds. However, SfM cannot provide complete DTMs as it

does not capture a “bare earth model”. LiDAR has the ability to penetrate through the small gaps in forest canopies and capture multiple returns. Because of this, LiDAR provides significantly more accurate elevation models (Rogers et al., 2020).

LiDAR’s application in forestry and ability to capture multiple returns from different canopy layers allows for detailed assessments of forest structure, including canopy height, density, and biomass. A key product derived from LiDAR data is the canopy height model (CHM), which is generated by subtracting the DTM from the DSM. The CHM can be used to delineate individual tree crowns with semi-supervised and unsupervised algorithms. Existing methods and algorithms to delineate individual crowns within a point cloud or CHM can be described as edge-based, region-based, morphological watersheds, and template matching (Zhen et al., 2016). Using these methods for tree canopy detection is possible with aerial LiDAR, that is manned aircraft collecting at point densities generally less than 10 points/m<sup>2</sup>, though UAS LiDAR can produce capture point densities greater than 1000 points/m<sup>2</sup> (Resop et al., 2019). With a 10-centimeter resolution CHM, researchers were able to identify 98% of the Tasmanian blue gum throughout four plots. The CHM detection and point cloud delineation (CDPD) hybrid algorithm, which uses a downscaled point cloud and resampled CHM to classify point clusters from identified individual local maxima (Wallace et al., 2014).

For surface mining, LiDAR can be used to classify land cover, geomorphological features, and evaluate reclamation progress. Though due to significant costs and training requirements, UAS-LiDAR may be out of reach for many managers and researchers. However, satellite and aerial platforms are able to provide more readily accessible and available data. For long-term analysis over large extents, as is generally the case when studying surface mines, these alternatives to UAS-LiDAR are commonly employed (Beland et al., 2019). Incorporating LiDAR data into image

analysis can provide ancillary features for classification tasks, improving detail of features and classification accuracy. When using a support vector machine to classify 5-meter imagery into five reclaimed land cover types on the Hobet-21 mountaintop mine, the model achieved 80.6% accuracy. The LiDAR derivates were then incorporated into the classifier, improving the overall accuracy to 86.4%. The LiDAR derivates include the first return intensity, first return intensity range, and a normalized DSM. Additionally, of the five image and three LiDAR derivates, the normalized DSM was found to have the second highest relative importance of all predictor variables (Maxwell et al., 2014). Topographic characteristics of reclaimed surface mines can also be evaluated using LiDAR derived DEMs, which can identify points of potential erosion or instability. Aerial LiDAR was used to assess landform alterations caused by MTR mining, which used a DEM to classify landform types and identify areas of ecological significance (Maxwell and Strager, 2013). These applications demonstrate LiDAR's ability as a tool to assess the effects of surface mining and reclamation, as well as improving accuracy of classifiers by providing more granular data.

#### *Unmanned Aerial Agricultural Systems*

As UAS technology has continued to develop, utility agricultural applications became an industry focus. The development of remote application technology, or a UAS equipped with a tank, pump, and nozzles, for applying herbicide or spreading fertilizer. Due to the increased payload, unmanned aerial agriculture systems (UAAS) have reduced flight times (Pederi and Cheponiuik, 2015). The use of UAAS resembles and is regulated as an aircraft crop-dusting operation. However, UAAS can apply treatments much closer to canopies, reducing drift, and can treat vegetation as prescribed by multispectral indices, reducing over-spray and increasing precision (Campos et al., 2019). Regulations are provided under 14 CFR Part 137, which governs the use of

aircraft and drones to dispense, or spray specified substances. UAS Part 107 pilots are required to obtain an Agricultural Aircraft Operator Certificate (AAOC). Additionally, UAASs commonly weigh above the Part 107 limit of 55 lbs., which requires pilots to submit petitions of exemption before operating (FAA, 1965).

Agricultural treatments are the primary application for UAAS, and their use is commonly associated with the term “precision agriculture”, a theory framework which aims to increase yield, reduce resource use, and promote environmentally sustainable practices (Hunt and Daughtry, 2017). Precision agriculture with UAAS generally use a smaller swath width, though sizes vary for tasks, allowing for efficient treatment of smaller areas and minimizing overspray with proper configuration (Liu et al., 2024). Variable rate spraying, another common feature of UAAS, employs a “prescription map” to adjust the treatment rate during a flight mission. This method can apply varied treatments according to vegetative health or observed pests, thus reducing pesticide use and inadvertent environmental impacts (Hanif et al., 2022). Additionally, during UAAS applications, there is a significant amount of downwash airflow that penetrates through the canopy. This allows increased coverage of vegetation and treatment performance. However, applicators should consider the effects of downwash on drift during treatments. Spraying parameters should be configured according to vegetation height, flight height, flight speed, and obstacles (Yang et al., 2019).

The use of UAAS for precision agriculture translated into applications for invasive species in natural landscapes. Using the general principles of precision agriculture, UAAS can treat invasive species in heterogenous and delicate environments while avoiding non-targeted species. Selective treatments using a prescription map can target classified invasive species and spray rates can be adjusted according to the density of the invasion (Meesaragandla et al., 2024). Use of

UAASs for invasive species is becoming more common, especially in areas that would be difficult to access otherwise. In the Suisun Marsh, California, researchers treated perennial pepperweed, an invasive species, using a UAAS. Using a survey UAS to first collect imagery of the sites, the locations of the invasions were then classified. The UAAS mission was programmed to treat areas according to these classifications. This achieved an efficacy rate of 80% across five hectares and was able to contain drift by 90% within 5 meters of the UAAS when flying 2-3 meters above the ground. The use of the UAAS significantly reduced operating costs, costing approximately \$37 per hectare as opposed to \$140 per hectare for a manned helicopter treatment (Takekawa et al., 2023).

Despite the increasing popularity of UAAS for agricultural and orchard management, there is very little scientific research published on the use and efficacy of UAAS for managing invasive species in natural ecosystems. Yet, UAAS performance in various conditions indicates strong potential for successful adoption in controlling invasive species in pastures and grasslands, above forest canopies, and in sensitive aquatic ecosystems. For example, UAS has effectively treated fruit tree canopies on rugged terrains with slopes of 40 to 45 degrees (Liu et al., 2024). In dynamic landscapes, where terrain can vary, UAAS can adapt in real time using local DEMs or on-board radar and LiDAR sensors (Wang et al., 2022). These performance abilities suggest that UAAS could become a versatile tool for managing invasive species across challenging terrains, mitigating operator exposure to harmful chemicals and treating targeted invasive species while avoiding desired species.

## **Machine Learning**

Machine learning and artificial intelligence (ML/AI) have revolutionized numerous fields, including remote sensing and environmental monitoring. The application of these technologies has

evolved significantly in recent years, driven by advancements in computational power, algorithm development, and increased data availability. In the context of invasive species management on reclaimed mine lands, machine learning approaches offer powerful tools for detection, classification, and monitoring at scales with accuracy previously unattainable through traditional methods.

### *Machine Learning in Remote Sensing*

The integration of machine learning with remote sensing has transformed how environmental data is processed and analyzed. Early applications primarily relied on pixel-based classification methods using traditional statistical approaches, but advancements in computer vision and deep learning have enabled more sophisticated analysis of complex spatial patterns (Maxwell et al., 2018). The transition from purely statistical methods to AI-driven approaches has been particularly beneficial for vegetation mapping and invasive species detection, where subtle spectral and textural features must be identified across heterogeneous landscapes (Kattenborn et al., 2019).

Remote sensing applications have evolved from basic land cover classification to detailed species-level identification through increasingly powerful machine learning algorithms. This progression has been accelerated by both the increasing spatial and spectral resolution of available imagery and the development of more sophisticated classification techniques (Maxwell et al., 2018). High-resolution imagery from UASs has been particularly instrumental in advancing these capabilities, providing centimeter-level resolution that can capture fine-scale vegetation characteristics essential for species discrimination (Dash et al., 2017).

### *Random Forest Classification*

Among the various machine learning algorithms applied to remote sensing data, Random Forest (RF) has emerged as one of the most widely utilized due to its robustness, interpretability, and effectiveness with high-dimensional data (Belgiu and Dragut, 2016). Initially introduced by Breiman (2001), RF is an ensemble learning method that constructs multiple decision trees during training and outputs the class that is the mode of the individual trees' classifications. This approach inherently reduces overfitting, a common challenge in vegetation classification where training samples may not fully represent the population's variability.

The effectiveness of RF in vegetation classification stems from several key characteristics. First, it can handle high-dimensional data without requiring feature reduction, making it well-suited for multispectral and hyperspectral imagery where numerous bands and derived indices serve as input features (Rodriguez-Galiano et al., 2012). Second, RF provides measures of variable importance, allowing researchers to identify which spectral bands or indices contribute most significantly to classification accuracy. This feature is particularly valuable in invasive species detection, where understanding which spectral regions best distinguish target species can inform sensor selection and processing workflows (Oliphant et al., 2016).

The RF analyses have demonstrated considerable success in detecting invasive species across various ecosystems. Mullerova et al. (2017) utilized RF classification with UAS imagery to map giant hogweed (*Heracleum mantegazzianum*) with accuracies greater than 80%. Similarly, Kattenborn et al. (2019) applied RF to detect black cherry (*Prunus serotina*) in central Europe using UAS-derived structural and spectral features, achieving user's accuracies of 86%. On reclaimed mine lands specifically, Maxwell and Strager (2013) leveraged RF classification to aid with classifying land cover types with LiDAR-derived topographic metrics and aerial imagery,

demonstrating the algorithm's utility on post-mining landscapes. Additionally, *Elaeagnus umbellata* was classified using Random Forest from Landsat satellite imagery collected over surface mines in southwestern Virginia. This study achieved an overall accuracy of 96.8% between two classes and incorporated a multitemporal approach (Oliphant et al., 2016).

Despite its advantages, RF has certain limitations in the context of complex vegetation mapping. It typically requires representative training samples for each class, which can be challenging to obtain in heterogeneous environments like reclaimed mine lands (Millard and Richardson, 2015). Additionally, while RF can identify important variables, it does not inherently exploit spatial autocorrelation or contextual information that might improve classification in landscapes with complex spatial patterns (Belgiu and Dragut, 2016). These limitations have motivated exploration of more advanced approaches, particularly deep learning methods that can automatically extract hierarchical features from imagery.

### *Convolutional Neural Networks*

Convolutional Neural Networks (CNNs) have emerged as a transformative approach for image classification and segmentation in remote sensing applications. Unlike traditional machine learning methods that rely on pre-defined features, CNNs automatically learn hierarchical features directly from the input data, capturing both spectral and spatial patterns that may not be apparent to human analysts. This capability is particularly valuable for invasive species detection, where the distinguishing characteristics may involve complex combinations of spectral signatures, textural patterns, and contextual relationships (Kattenborn et al., 2021).

The architecture of CNNs typically consists of multiple layers of convolutional filters followed by pooling operations, which progressively extract higher-level features from the input imagery. These features are then processed through fully connected layers to produce classification

outputs (Kattenborn et al., 2021). This hierarchical feature extraction enables CNNs to identify patterns at multiple scales, from fine-textured characteristics of individual plants to broader landscape patterns that may indicate invasive species presence (Weinstein et al., 2020).

Recent advances in CNN architectures have further enhanced their suitability for vegetation mapping and invasive species detection. Fully convolutional networks (FCNs) and encoder-decoder architectures like U-Net have enabled pixel-level semantic segmentation, allowing precise delineation of species boundaries (Ronneberger et al., 2015). These segmentation approaches are particularly valuable for mapping species like autumn olive, which can form irregular patches across heterogeneous landscapes (Kattenborn et al., 2021).

Several studies have demonstrated the effectiveness of CNNs for invasive species detection using UAS imagery. Onishi and Ise (2021) utilized a U-Net architecture to map invasive bamboo species in Japan, achieving overall accuracies exceeding 90%. Similarly, Padua et al. (2022) applied CNNs to detect water hyacinth in multispectral imagery, which demonstrated superior performance compared to traditional methods. For woody vegetation, Wang et al. (2021) demonstrated that CNN-based approaches, utilizing high-resolution imagery, can effectively identify invasive shrubs such as eastern redcedar. The integration of multispectral data with CNNs has proven particularly effective for vegetation classification. Amarasingam et al., (2024) found that incorporating multispectral bands and vegetation indices as additional input channels to CNN models significantly improved classification accuracy for coastal, invasive vegetation. This approach is especially relevant for autumn olive detection, as similar species exhibit distinctive spectral characteristics, particularly in the near-infrared and red-edge regions (Ezzarrouqy et al., 2023).

Despite their powerful capabilities, CNNs present certain challenges for operational deployment in invasive species management. They typically require substantial training data, which can be labor-intensive to collect and annotate (Millard and Richardson, 2015; Maxwell et al., 2018). Additionally, CNN models are often computationally intensive, requiring specialized hardware for efficient training and deployment. Recent developments in transfer learning and model optimization have begun to address these limitations, making CNN approaches increasingly accessible for practical applications in land management (Kattenborn et al., 2021).

#### *Time Series Analysis and Phenological Approaches*

The temporal dimension of vegetation dynamics offers valuable information for discriminating invasive species from native vegetation. Time series analysis leverages multitemporal imagery to capture phenological patterns, such as seasonal changes in vegetation characteristics such as leaf emergence, flowering, and senescence, which can serve as distinctive ‘signatures’ for species identification (Fan et al., 2022). For autumn olive specifically, its extended leaf-on period relative to native species creates a temporal window of opportunity for detection using multitemporal imagery (Oliphant et al., 2016; Riffe, 2018).

Traditional time series analysis in remote sensing often relies on vegetation indices derived from multiple image acquisitions throughout the growing season. Metrics such as the start of season, peak greenness, and rate of senescence can be extracted from these time series and used as features in classification algorithms (Zeng et al., 2020). Recent advances have enhanced these approaches through more sophisticated time series models that can account for irregular sampling intervals and data gaps common in UAS acquisitions (Feng et al., 2020). Deep learning approaches have also been extended to incorporate temporal information through recurrent neural networks (RNNs) and their variants, such as long short-term memory (LSTM) networks. These architectures

are specifically designed to capture temporal dependencies in sequential data, making them well-suited for analyzing vegetation phenology (Russwurm and Körner, 2018). Yi et al. (2020) demonstrated the effectiveness of LSTM networks for crop classification using multitemporal Sentinel-2 imagery, achieving higher accuracy than methods considering only spatial information.

For invasive species like autumn olive on reclaimed mine lands, phenological approaches offer several advantages. The extended leaf-on period of autumn olive relative to native deciduous species creates a temporal signature that can be captured through multitemporal imagery (Riffe, 2018). Additionally, the timing of flowering and fruiting can provide further distinguishing characteristics that may be detected through spectral changes in UAS imagery (Franke et al., 2018). Modeling these phenological patterns can enhance detection accuracy, particularly in mixed vegetation communities where spectral confusion may occur at certain times of the year (Wood et al., 2022).

Recent research has explored the integration of phenological information with spatial features through combined CNN-LSTM architectures. Russwurm and Körner (2018) demonstrated the effectiveness of this approach for crop classification using satellite imagery, while Guo et al. (2022) applied similar methods to detect invasive species using multitemporal UAS data. These integrated approaches leverage both the spatial feature extraction capabilities of CNNs and the temporal modeling strengths of RNNs, providing a powerful framework for invasive species monitoring across seasonal transitions.

#### *Explainable AI and Feature Importance*

As machine learning approaches become increasingly sophisticated, the interpretability of models has emerged as a critical consideration for operational deployment in land management. Explainable AI methods seek to provide insights into model behavior, helping users understand

which features drive classification decisions and how models might generalize to new contexts (Roscher et al., 2020). This interpretability is particularly important in invasive species management, where understanding the biophysical basis for detection can inform broader ecological understanding and management strategies.

For Random Forest models, built-in measures of variable importance provide straightforward insights into which spectral bands or indices contribute most significantly to classification accuracy (Belgiu and Dragut, 2016). More robust approaches such as permutation importance and Shapley Additive Explanations (SHAP) have enhanced these capabilities, providing feature importance measures that account for feature interactions and are consistent across different models (Lundberg and Lee, 2017). These methods have been applied in vegetation mapping to identify the most discriminative features for target species, informing both model development and ecological understanding (Abdollahi and Pradhan, 2021).

For deep learning approaches like CNNs, visualization techniques such as gradient-weighted class activation mapping or 3D loss landscapes have emerged as valuable tools for model interpretation (Selvaraju et al., 2017). These methods generate feature maps which highlight image regions that strongly influence classification decisions, providing spatial context for model predictions. Ma et al. (2024) applied these techniques to CNN models for tree species classification, revealing that models often focus on distinct textural and structural patterns in tree crowns that align with known vegetative characteristics.

Understanding which features drive classification decisions can provide valuable ecological insights while informing data collection strategies. For autumn olive detection, identifying the most discriminative spectral regions and temporal windows can guide sensor selection and flight planning for optimal results (Kattenborn et al., 2021). Additionally, interpreting

why misclassifications occur can reveal ecological contexts where detection is challenging, such as mixed vegetation communities or specific phenological stages, informing the development of more robust approaches (Pichler and Hartig, 2023).

### *Emerging Trends*

Translating machine learning approaches from research to operational invasive species management requires consideration of computational requirements, data availability, and integration with existing workflows. While powerful deep learning approaches may achieve high accuracy in research settings, simpler methods may be more practical for routine monitoring given resource constraints (Padua et al., 2022). Finding the optimal balance between model complexity and operational feasibility remains an active area of research in applied remote sensing.

Recent developments in edge computing and model optimization have begun to address the computational challenges of deploying sophisticated machine learning models in field settings. Techniques such as model pruning, quantization, and knowledge distillation can significantly reduce model size and computational requirements while maintaining acceptable accuracy (Howard et al., 2019). These approaches are particularly relevant for UAS-based monitoring, where onboard processing capabilities may be limited.

Cloud computing platforms have also emerged as valuable resources for processing and analyzing remote sensing data with machine learning approaches. Services such as Google Earth Engine provide access to extensive archives of satellite imagery along with public computing resources for implementing classification algorithms (Gorelick et al., 2017). These platforms can complement UAS-based monitoring by providing broader spatial and temporal context for invasive species detection and spread assessment.

Looking forward, several emerging trends promise to further enhance machine learning capabilities for invasive species management. Active learning approaches, which iteratively select the most informative samples for manual annotation, can significantly reduce the training data requirements for supervised classification (Miao et al., 2024). Semi-supervised and self-supervised learning methods leverage unlabeled data to improve model generalization, addressing the challenge of limited labeled samples in complex environments (Russwurm et al., 2020). These approaches are particularly valuable for monitoring dynamic landscapes like reclaimed mine lands, where vegetation communities evolve rapidly.

Multimodal sensing approaches that integrate data from different sensors, such as multispectral imagery and LiDAR, are also gaining traction for improved vegetation mapping and classification. The fusion of spectral and structural information can enhance discrimination between species with similar spectral signatures but different growth forms or canopy structures (Weinstein et al., 2020). For autumn olive detection specifically, integrating multispectral imagery with structural information from photogrammetric point clouds or LiDAR could improve separation from other shrub species common on reclaimed mine lands (Maxwell et al., 2014).

As these technologies continue to evolve, their integration with invasive species management workflows represents a promising avenue for enhancing early detection and rapid response strategies on reclaimed mine lands and beyond. By leveraging the increasing spatial, spectral, and temporal resolution of UAS imagery alongside advanced machine learning techniques, land managers can develop more efficient and effective approaches to controlling invasive species like autumn olive on these challenging landscapes.

## **Methods**

### **Study Area**

Data collection for this research was conducted at two reclaimed surface mines in Monongalia County, West Virginia: the Goshen Road site and the Little Indian Creek Wildlife Management Area (Fig. 1). Both sites represent post-mining landscapes at different stages of reclamation and vegetation development, providing complementary conditions for evaluating *Elaeagnus umbellata* detection and treatment techniques.

#### *Goshen Road*

The Goshen Road (GR) site is located southeast of Morgantown, WV, on a privately owned 740-acre parcel belonging to Reliance Minerals Inc. This study area was historically the location of a refuse pile from the adjacent Mays Run Mine (WVDEP, 2024) and as an abandoned mine land that predates SMCRA, the site underwent reclamation efforts by WVDEP.

The specific study area encompasses 13 acres of flat, leveled topography. The general vegetation community is characteristic of early successional reclaimed surface mine lands, with grasses and shrubs found throughout the center of the site. Stands of mature hardwoods are also included in the study site along the edges of the site. Two active underground mining operations are present on the larger property, though they have no direct impact on the study area. Additionally, an ongoing research project on biomass volumes is being conducted within the portions of the site; however, our research activities were limited to imagery collection over these experiment plots, with no treatments applied within those plot boundaries.

### *Little Indian Creek*

The Little Indian Creek Wildlife Management Area (LIC) is located southwest of Morgantown, WV, within District 1 of the WVDNR. The property is 1,036 acres and was acquired by the state of West Virginia in 2006 from The Conservation Fund. Formerly a surface mine, the area was reclaimed specifically for wildlife habitat development and has since become a popular destination for recreational activities including hunting and hiking (WVDEP, 2024). Site access was coordinated with and facilitated by Logan Klingler, the WVDNR District 1 Wildlife Manager.

The LIC study site covers approximately 15 acres and exhibits a characteristic plateau-like landscape typical of mountain-top removal mining. While the broader LIC property supports diverse habitat types including hardwood forests, pollinator habitat areas, and pastures, the specific study site represents a grassland/shrubland ecosystem with interspersed stands of black locust (*Robinia pseudoacacia*), American sycamore (*Platanus occidentalis*), maple species (*Acer spp.*), tree-of-heaven (*Ailanthus altissima*), and others. *Elaeagnus umbellata* occurs throughout the site in isolated clusters, as understory growth beneath tree canopies, and intermixed with other species in densely vegetated areas. The LIC site displays significantly greater heterogeneity than GR, with more diverse species composition, varied vegetation heights, and complex canopy densities and patterns.



Figure 1: Goshen Road Reclaimed Surface Mine (left) and Little Indian Creek Wildlife Management Area (right)

#### *Site Selection*

These two sites were strategically selected to represent different stages and management approaches in mine reclamation while sharing the common challenge of an *Elaeagnus umbellata* invasion. The GR site provides an example of an earlier-stage reclamation landscape with simpler vegetation structure, while the LIC site represents a more complex and heterogeneous post-reclamation landscape. This contrast allows for evaluation of detection methodologies across varying levels of ecological complexity, enhancing the robustness and applicability of the research findings to diverse reclaimed mine lands throughout the Appalachian region (Skousen and Zipper,

2014; Maxwell et al., 2013) Furthermore, both sites are located within unrestricted airspaces for both UAS and UAAS operations.

## Data Collection

### *UAS Platform and Sensors*

Aerial imagery was collected using a DJI Matrice 200 (Fig. 5) and a DJI Matrice 300 RTK (Fig. 6) quadcopter equipped with a Sentera 6X multispectral sensor (Fig. 7) (*see Equipment section*). The Sentera 6X sensor features five monochromatic bands in the visible and near-infrared regions, and a RGB camera for true-color imagery (Table 1). The spectral bands include Blue (460-490 nm), Green (540-560 nm), Red (655-685 nm), Red-Edge (710-720 nm), and NIR (830-850 nm), allowing for comprehensive spectral analysis of vegetation properties. The camera uses an incident light sensor (ILS), equipped to the top of the UAS, for collecting downwelling radiance over the course of the image collection. Additionally, before each flight, the Sentera 6X captures photos of a calibrated reflectance panel.

Table 1: Sensor Specifications

---

#### *Sentera 6X Monochrome*

3.2 MP Monochrome Global Shutter	
	<u>Band Wavelength</u>
Focal Length:	8 mm
HFOV:	47°
GSD @ 200 ft:	1.0" (2.6cm)
	Blue: 460-490 nm
	Green: 540-560 nm
	Red: 655-685 nm
	Red-Edge: 710-720 nm
	NIR: 830-850 nm

---

#### *Sentera 6X RGB*

20 MP RGB Electronic Rolling Shutter	
Focal Length:	7.2 mm
HFOV:	47°
GSD @ 200 ft:	0.4" (1.0cm)

### *UAS Data Collection*

Flights were conducted at the GR and LIC sites beginning 1/18/2023 and 2/24/2023, respectively (Table 2). These flights were repeated during all seasons throughout the year; however, this was dependent on factors such as weather, resource availability, equipment issues, and access to LIC during hunting seasons. Imagery was captured over both sites during the leaf-on and leaf-off periods until October 11, 2024, providing a comprehensive temporal dataset spanning multiple phenological stages.

The DJI Matrice 200 was used for flights that took place from the beginning of data collection until March 2024. Because this UAS platform is not equipped with a real-time kinematics GPS (RTK), five ground control points (GCPs) were collected at both sites with a Spectra Precision SP80 RTK GNSS receiver (SP80) (Fig. 8). For flights conducted from April 2024 until October 2024, a DJI Matrice 300 RTK was used for flights at GR and LIC. The M300 RTK does not require GCPs for georeferencing and precise capture locations are recorded with the image metadata. The UAS was flown at 60 meters above ground level (AGL) with 70% front overlap and 80% side overlap for all flights at the at the GR and LIC sites.

Table 2: Flight Log

<u>Stage</u>	<u>Site</u>	<u>Date</u>	<u>Overlap</u>	<u>Altitude</u>
Early	Goshen Road	3/28/2024	70% front/80% side	60 meters
	Goshen Road	4/13/2023	70% front/80% side	60 meters
	Little Indian Creek WMA	4/13/2023	70% front/80% side	60 meters
	Goshen Road	4/25/2023	70% front/80% side	60 meters
	Goshen Road	5/1/2024	70% front/80% side	60 meters
Peak	Goshen Road	5/20/2024	70% front/80% side	60 meters
	Little Indian Creek WMA	5/31/2023	70% front/80% side	60 meters
	Goshen Road	6/3/2024	70% front/80% side	60 meters
	Little Indian Creek WMA	6/8/2023	70% front/80% side	60 meters
	Little Indian Creek WMA	6/21/2024	70% front/80% side	60 meters
	Little Indian Creek WMA	7/19/2023	70% front/80% side	60 meters
	Goshen Road	8/3/2023	70% front/80% side	60 meters
	Little Indian Creek WMA	8/16/2024	70% front/80% side	60 meters
	Little Indian Creek WMA	8/31/2023	70% front/80% side	60 meters
	Goshen Road	8/31/2023	70% front/80% side	60 meters
Late	Goshen Road	9/6/2024	70% front/80% side	60 meters
	Little Indian Creek WMA	9/13/2023	70% front/80% side	60 meters
	Little Indian Creek WMA	9/26/2024	70% front/80% side	60 meters
	Goshen Road	9/29/2023	70% front/80% side	60 meters
Senescence	Little Indian Creek WMA	10/13/2023	70% front/80% side	60 meters
	Little Indian Creek WMA	10/25/2023	70% front/80% side	60 meters
	Goshen Road	10/27/2023	70% front/80% side	60 meters
	Little Indian Creek WMA	11/8/2023	70% front/80% side	60 meters
	Goshen Road	11/13/2023	70% front/80% side	60 meters

## **Image Processing**

### *Radiometric Corrections and Photogrammetry*

After data collection, multispectral images were radiometrically corrected for atmospheric and lighting distortions using the captured calibration panel and ILS sensor with the provided post-processing script (Sentera, LLC). Once images were radiometrically corrected, Agisoft Metashape was used to generate orthomosaics for each flight and were georeferenced using either RTK positioning or ground-control points to NAD83 / UTM Zone 17 North. Orthomosaics were generated with a ground sampling distance of 3 cm/pixel for multispectral imagery and 1.5 cm/pixel for RGB imagery. All orthomosaics were georeferenced with a horizontal positioning error of less than 1 meter.

### *Vegetation Indices*

Multispectral imagery offers the opportunity to extract valuable information beyond what is visible in standard RGB imagery. Vegetation indices are mathematical combinations of spectral bands designed to enhance the signal of vegetation properties while minimizing the influence of confounding factors such as soil background and atmospheric effects. For this study, 15 vegetation indices were calculated from the 5-band multispectral imagery to provide a comprehensive set of features for *Elaeagnus umbellata* detection and classification. The selection of vegetation indices was guided by their demonstrated utility in previous research on invasive species and other vegetation detection and mapping. Each index captures different aspects of vegetation physiology and structure that may help distinguish *Elaeagnus umbellata* from other vegetation types on reclaimed surface mines. Table 3 lists the vegetation indices used in this study, along with their band formulas.

Table 3: Vegetation Indices

<u>Vegetation Indices</u>	<u>Formula</u>
Normalized Difference Vegetation Index	$NDVI = (NIR - Red) / (NIR + Red)$
Normalized Difference Red-Edge Index	$NDRE = (NIR - RedEdge) / (NIR + RedEdge)$
Green Normalized Difference Vegetation Index	$GNDVI = (NIR - Green) / (NIR + Green)$
Blue Normalized Difference Vegetation Index	$BNDVI = (NIR - Blue) / (NIR + Blue)$
Leaf Chlorophyll Index	$LCI = (NIR - RedEdge) / (NIR + Red)$
Green Chlorophyll Index	$GCI = (NIR / Green) - 1$
Red Edge Chlorophyll Index	$RECI = (NIR / RedEdge) - 1$
Simple Ratio Index	$SRI = (NIR / Red)$
Green-Red Normalized Difference Vegetation Index	$GRNDVI = (NIR - (Green + Red)) / (NIR + (Green + Red))$
Optimized Soil Adjustment Vegetation Index	$OSAVI = (NIR - Red) / (NIR + Red + 0.16)$
Enhanced Vegetation Index 2	$EVI2 = (2.5(NIR - Red) / (NIR + 2.4(Red) + 1)$
Red Edge Green Index	$ReGI = (RedEdge / Green)$
Green-Red Vegetation Index	$GRVI = (Green - Red) / (Green + Red)$
Chlorophyll Vegetation Index	$CVI = NIR(Red / Green^2)$
Green-Blue Vegetation Index	$GBVI = (Green - Blue) / (Blue + Green)$

## **Data Collection and Annotation**

### *GPS Data Collection*

Reference data for identifying *Elaeagnus umbellata* in UAS imagery was collected with systematic field surveys conducted during the spring and summer of 2023. GPS points were collected using a Spectra Precision SP80 RTK GNSS receiver. Because *Elaeagnus umbellata* can grow in dense thickets, collecting reference GPS points for each individual and at the center of each crown can be difficult to distinguish. This also causes difficulty to discern the exact number of individuals at each point, however the reference data allows delineation between

During the leaf-on period of 2023, GPS points were collected using a Spectra Precision SP80 RTK GNSS receiver at the GR and LIC sites. Points were collected with fixed-RTK GPS coordinates at the location of *Elaeagnus umbellata*. Because *Elaeagnus umbellata* grows in dense thickets, and it is difficult to discern the exact number of individual trees at each point, points were collected on the circumference of the canopies. These points were then manually adjusted using ArcGIS Pro 3.4 (Esri) to be placed over the center of each discernable individual canopy. Additional points were also added by referencing orthomosaics and known locations of autumn olive that were not able to be reached.

### *Image Annotation and Datasets*

Image annotations are digitized segmentations used to label features or areas of interest within an image. Annotations for image classification can be in the form of either bounding boxes, polygons, or points. In this study, four annotated datasets were created for each flight. All the datasets contained four classes:

1. Barren: Instances of gravel and soil.
2. LowVeg: Instances of grass and other low vegetation.

3. AutumnOlive: Instances of *Elaeagnus umbellata* canopies.
4. OtherTree: Instances of all other tree canopies other than *Elaeagnus umbellata*.

The first dataset was generated specifically for the Random Forest classification approach, using a point-based sampling strategy. GPS points collected during field surveys provided the foundation for autumn olive locations, with additional points manually placed for other land cover classes. These points were buffered to create circular areas with a 0.1-meter radius. Within each digitized polygon for the respective land cover classes, 10 random points were generated and buffered to ensure adequate sampling of spectral variability within each class. Additionally, for large and contiguous classes like ‘Barren’ and ‘LowVeg’, these annotations were divided into grids of 10 sq/meters with the buffered points placed within each one. The buffered points were used to extract mean spectral values and vegetation indices from the orthomosaics using ArcGIS Pro 3.4. This process created tabular data with each row representing a single buffered point and columns containing the mean values for each spectral band and vegetation index. This structured format was particularly suitable for the Random Forest algorithm, which performs well with tabular feature data. Visual verification was performed on all extracted points to ensure that each buffered area contained only features belonging to the assigned class, minimizing the introduction of mixed pixels in the training data.

For the deep learning classification, three datasets were created from the annotated features (Fig. 2). A multispectral dataset was created containing 5-band multispectral imagery (Blue, Green, Red, Red-Edge, and NIR) with corresponding class masks. Second, a dataset containing the 5-band multispectral data with 3 selected vegetation indices identified as most important through the Random Forest feature importance analysis. This 8-band dataset was designed to evaluate whether the inclusion of pre-calculated vegetation indices improved detection performance compared to

using raw spectral bands alone. Third, an RGB dataset was created using the RGB images captured using the Sentera 6X 20 MP camera.

For all three deep learning datasets, orthomosaics and their corresponding annotation masks were divided into 256 x 256-pixel chips using a sliding window with 50% overlap between adjacent chips and a minimum coverage of 10% with any class (Fig. 3). By using the overlap and minimum coverage parameters, this method ensures that features near edges of chips are adequately represented in the training data and improves the model's ability to detect features that cross chip boundaries. Each chip maintained the original spatial resolution of the orthomosaic, which preserves the detailed texture and spectral information necessary for accurate classification of the classes of interest.

The annotation masks were created by converting the polygon annotation features to raster format with unique integer values assigned to each class (1=Barren, 2=LowVeg, 3=AutumnOlive, 4=OtherTree, and 0=non-annotated areas). These masks were chipped in the same manner as the imagery to maintain an exact pixel-to-pixel correspondence between input data and target classifications.

Finally, to enhance computational efficiency and model performance, the image chips and corresponding masks were organized into a structured dataset format compatible with PyTorch. Each deep learning dataset was divided into training (80%) and validation (20%) subsets, with stratification to ensure representative class distributions in each subset. This partitioning strategy follows best practices for deep learning model development in remote sensing applications.



Figure 2: Deep learning annotated training data

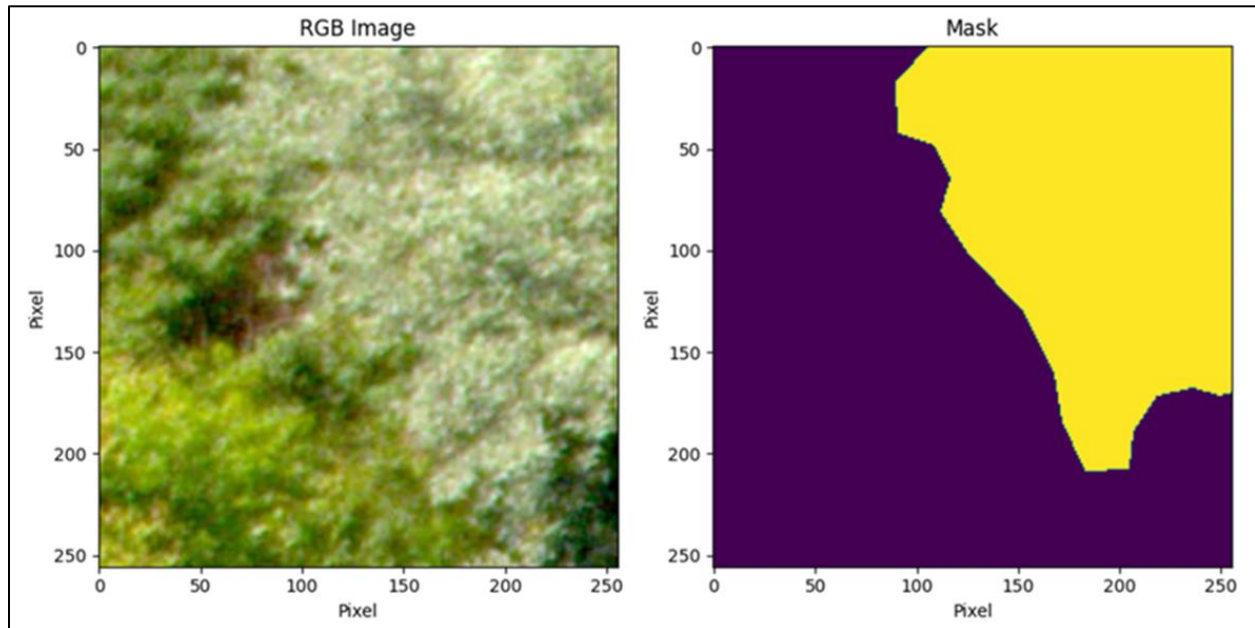


Figure 3: Deep learning 256 x 256 image and mask

## **Random Forest Classification**

Random Forest (RF) is a non-parametric ensemble learning method that constructs multiple decision trees during training and outputs the class that is the mode of the classes of the individual trees (Breiman, 2001). This algorithm has been widely used for remote sensing applications due to its robustness, resistance to overfitting, and ability to handle high-dimensional data (Belgiu and Dragut, 2016).

### *Data Preparation and Preprocessing*

Using the multispectral orthomosaic dataset and point annotations, RF classification was performed with R 4.4.1 and the ‘randomForest’ package (version 4.7-1.2) (Breiman et al., 2024). Multispectral orthomosaics were used to derive the mean reflectance values of each individual band and vegetation indices from the multispectral data captured within the buffered annotation points. For each annotated point, values were extracted from all 5 spectral bands (Blue, Green, Red, Red-Edge, NIR) and the 15 derived vegetation indices. Using the RF implementation in R was chosen over ArcGIS Pro’s “random trees” tool because it proves a full, statistically rigorous Random Forest algorithm. In contrast, ArcGIS Pro uses a proprietary random tree model that lacks features such as full bootstrapping, out-of-bag evaluation, and interpretability, making it less suited for model interpretation and reproducibility.

Prior to model development, exploratory data analysis was conducted to assess the distribution of spectral signatures across different classes. Mean reflectance values were calculated for each class across all spectral bands to visualize the separability of autumn olive from other vegetation classes. Missing values were identified and treated, though they were minimal due to the preprocessing steps applied to the orthomosaics.

To address class imbalance issues commonly encountered in land cover classification tasks (Millard and Richardson, 2015), a balanced sampling approach was implemented. For each flight and class combination, a target sample of 1,000 points was selected, with replacement sampling used when fewer than 1,000 points were available for a given class. This approach helps improve classification accuracy for classes with limited training samples without introducing significant bias.

#### *Multicollinearity Assessment*

Prior to model training, multicollinearity among predictor variables was assessed using Pearson correlation matrices computed for all 15 vegetation indices. This step was critical given that many vegetation indices are derived from the same spectral bands, potentially creating statistical redundancies that can impact model stability and interpretability. Correlation matrices were generated separately for each phenological stage to evaluate how relationships between indices varied seasonally. The analysis focused on identifying groups of highly correlated indices and determining which variables might provide complementary information. Indices with a high level of correlation were noted but not automatically removed, as Random Forest can handle correlated predictors better than parametric methods (Millard and Richardson, 2015). Instead, the information was used to interpret feature importance in subsequent analyses and to guide the selection of indices of the VI-Composite U-Net model.

#### *Phenological Stage-Specific Models*

The dataset was divided into four stages based on phenology. Phenological stages were chosen by visual observations during field visits and align with leaf area index values measured by Oliphant et al. (2016), which were taken in the same region. These stages are:

1. Early-Stage (early spring, limited leaf development)

2. Peak-Stage (late spring/summer, full leaf development)
3. Late-Stage (early fall, beginning of senescence)
4. Senescence-Stage (late fall, advanced leaf color change and leaf drop)

A separate RF model was trained for each phenological stage to capture the temporal dynamics of autumn olive's spectral signature. Each dataset was split into training (80%) and testing (20%) sets using stratified random sampling to maintain class proportions. This stage-specific modeling approach is particularly valuable for detecting species with distinctive phenological patterns, such as autumn olive, which has an extended leaf-on period compared to native species (Riffe, 2018).

For each stage-specific model, hyperparameter tuning was performed to optimize performance. The primary parameter tuned was ‘mtry’ (number of variables randomly sampled as candidates at each split), which was explored through a grid search approach using values ranging from 2 to the total number of predictor variables (mtry = 20). Ten-fold cross-validation was used to evaluate each parameter combination, with overall accuracy serving as the optimization metric. The number of trees (ntree) was set to 500, as this value has been shown to provide stable results in similar remote sensing applications (Rodriguez-Galiano et al., 2012).

#### *Feature Importance Analysis*

To understand which vegetation indices contributed most significantly to autumn olive detection, two complementary feature importance analyses were conducted: First, permutation importance analysis was conducted by randomly shuffling one predictor variable at a time in the validation dataset and measuring the resulting decrease in prediction accuracy for each class (Altmann et al., 2010). This approach provides class-specific importance scores, allowing for

identification of features that are particularly valuable for autumn olive detection. Second, SHAP (SHapley Additive exPlanations) values were calculated using the ‘fastshap’ R package (Greenwell, 2024). This method, based on cooperative game theory and Monte Carlo simulations, provides a more interpretable feature importance measure by assigning each feature an importance value for a particular prediction. Due to computational constraints, a subset of the dataset (balanced by class and flight) was used for SHAP analysis.

The results from these three approaches were compared to identify consistently important features across methods. The most important features identified through this process were subsequently used to inform the input selection for the deep learning models, particularly the VI-Composite U-Net.

#### *Model Evaluation*

Each Random Forest model was evaluated using the independent test set. Several metrics were calculated to assess performance:

1. Overall accuracy: the proportion of correctly classified instances across all classes
2. Class-specific precision: the proportion of true positives among instances predicted as positive
3. Class-specific recall: the proportion of true positives identified among all actual positives
4. Class-specific F1-score: the harmonic mean of precision and recall
5. Balanced accuracy: the average of recall values for each class, which accounts for class imbalance

Confusion matrices were generated to visualize the patterns of misclassification between classes. Additionally, precision-recall curves were created specifically for the autumn olive class to assess the trade-off between precision and recall at different classification thresholds.

The performance metrics across all four phenological stages were compared to identify the optimal time periods for autumn olive detection. This temporal analysis provides insights into when the spectral signatures of autumn olive are most distinct from other vegetation types on reclaimed mine lands, informing EDRR strategies.

## **Convolutional Neural Network Classification**

Building on the insights from the Random Forest feature selection analysis, three different U-Net models were developed to evaluate the potential of deep learning approaches for autumn olive detection on reclaimed mine lands.

### *U-Net Model Architecture and Modifications*

The U-Net architecture, originally developed by Ronneberger et al. (2015) for biomedical image segmentation, has been adapted for remote sensing applications with demonstrated success in vegetation mapping (Kattenborn et al., 2021). The standard U-Net includes a contracting path (encoder) that captures context and an expanding path (decoder) that enables precise localization, connected by skip connections that preserve spatial information.

For this study, several modifications were implemented to enhance performance for autumn olive detection in the heterogeneous environment of reclaimed surface mines. Progressive dropout was incorporated throughout the network, with rates increasing with network depth (0.1 in early layers to 0.3 in deeper layers). This approach helps prevent overfitting while maintaining feature learning capacity in early layers where spatial information is critical (Tompson et al., 2015).

Batch normalization layers were included after each convolution operation to stabilize training and accelerate convergence by normalizing the inputs to each layer (Ioffe and Szegedy, 2015).

The loss function was modified to use a weighted combination of cross-entropy and focal loss, addressing the class imbalance that is inherent in the autumn olive detection task. The focal loss component (with  $\gamma=2$ ) helps the model focus on hard-to-classify examples by reducing the contribution of easy examples to the loss, which improves performance for imbalanced classes in semantic segmentation tasks (Lin et al., 2017). Class weights were dynamically calculated based on the pixel frequency of each class and were adjusted to give higher importance to the ‘AutumnOlive’ class (weight=1.8) and the ‘OtherTrees’ class (weight=1.5), compared to other more distinguishable and common classes like ‘Barren’ and ‘LowVeg’, respectively (weight = 1.0).

To increase the diversity of training samples and improve model generalization, data augmentation techniques were applied during training. These included horizontal and vertical flips (25% probability each) and 90-degree rotations (25% probability), which create synthetic training examples that represent the same features in different orientations.

#### *Model Variants and Input Data*

Three distinct U-Net variants were implemented (Fig. 4), each with different input data configurations to evaluate the importance of spectral information for autumn olive detection:

The RGB U-Net used only 3-band RGB imagery as input, representing the simplest data configuration that might be available from standard drone platforms. Flight-specific normalization was applied to account for variations in lighting and atmospheric conditions across different acquisition dates. This normalization involved calculating flight-specific statistics (mean, standard deviation, and 1st/99th percentiles) for each RGB band and using these to standardize pixel values,

an approach that has been shown to improve CNN performance in remote sensing applications (Audebert et al., 2019).

The Multispectral U-Net utilized the full 5-band multispectral data (Blue, Green, Red, Red-Edge, NIR) as input. Radiometric correction was applied to ensure consistent reflectance values across flights, allowing the model to learn meaningful spectral patterns regardless of acquisition conditions. The VI-Composite U-Net combined 5-band multispectral data with 3 key vegetation indices identified from the Random Forest feature importance analysis, creating an 8-band input dataset. This approach integrates both raw spectral information and domain-specific vegetation metrics that highlight autumn olive characteristics.

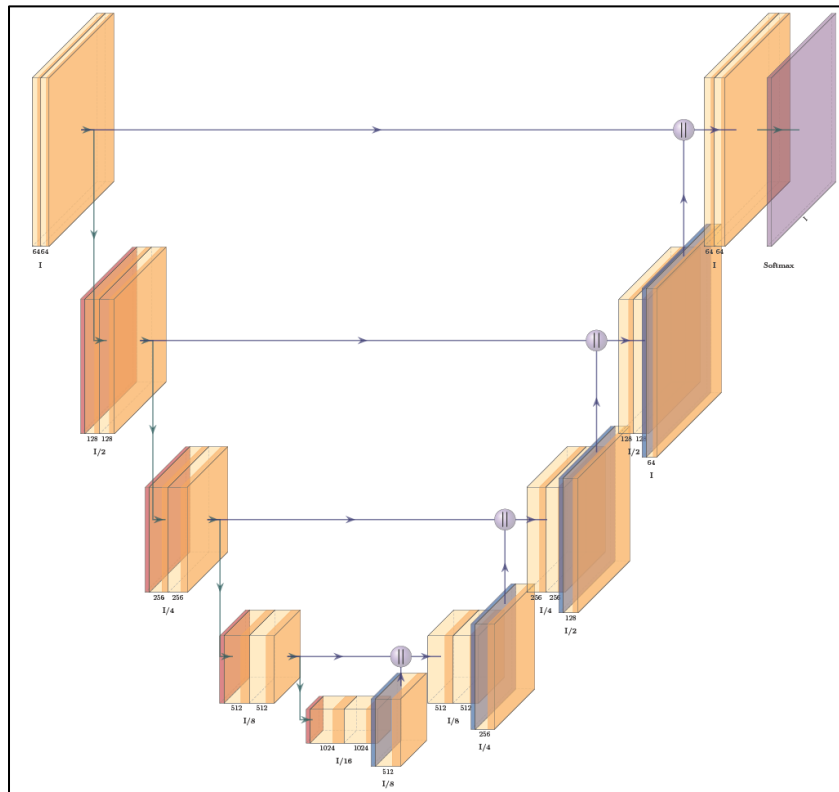


Figure 4: U-Net Model Architecture

### *Training Process and Hyperparameter Tuning*

All U-Net models were implemented using PyTorch and trained on 256 x 256-pixel image chips extracted from the original imagery. To ensure representative training and validation sets, chips were split using a stratified approach based on the presence/absence of each class. A composite label was created for each chip reflecting the class composition, and an 80/20 train/validation split was performed to maintain similar class distributions in both sets, following best practices for semantic segmentation tasks (Audebert et al., 2019).

For model optimization, the AdamW optimizer was used with weight decay (1e-4) to prevent overfitting while maintaining good convergence properties (Loshchilov and Hutter, 2019). An OneCycleLR learning rate scheduler was employed with an initial learning rate of 0.001 and a maximum learning rate of 0.005. This approach, which includes a gradual warm-up phase followed by a controlled decay, has been shown to improve convergence and generalization in deep learning models (Smith, 2018).

To address class imbalance in the training data, a weighted random sampling strategy was implemented with priority weights of 1.8 for autumn olive, 1.5 for other trees, and 1.0 for barren and low vegetation classes. This ensured that the model was exposed to a balanced distribution of classes during training, preventing bias toward more common land cover types.

Model training was conducted on the Dolly Sods high-performance computing (HPC) cluster maintained by West Virginia University. Models were trained with a batch size of 48 on three NVIDIA A40 GPUs using PyTorch's DataParallel for distributed training, for up to 200 epochs. Early stopping with a patience of 15 epochs was implemented to prevent overfitting, with validation loss used as the monitoring metric. To stabilize training, gradient clipping with a

maximum norm of 1.0 was applied at each update step, preventing exploding gradients that can occur in deep networks (Pascanu et al., 2013).

Each model was trained separately on each phenological stage, allowing for stage-specific optimization and performance evaluation. This approach accounts for the seasonal variations in autumn olive's spectral signature and enables comparison of detection performance across different times of the year.

#### *Model Evaluation and Comparison*

To ensure a comprehensive evaluation of model performance, multiple metrics were calculated for each model on the validation datasets. These included overall accuracy, class-specific precision, recall, and F1-scores, as well as confusion matrices to visualize classification patterns.

Special attention was given to the autumn olive class, with additional metrics including the precision, recall, and F1-score, which provide a more nuanced view of performance for this key class of interest. The trade-off between precision (minimizing false positives) and recall (minimizing false negatives) is particularly important for invasive species management applications, where the cost of missing true instances must be balanced against the resources required to address false detections.

Visual assessment of the segmentation results was also conducted, comparing the predicted autumn olive distribution maps with the reference data and RGB imagery. This qualitative evaluation helps identify specific conditions or landscape contexts where the models perform well or struggle, providing insights that purely quantitative metrics might miss (Maxwell et al., 2018).

The performance of the CNN models was compared with the Random Forest classification results to assess the relative strengths and limitations of each approach. This comparison considered not only overall accuracy metrics but also computational requirements, training time, and ease of deployment, factors that impact the operational utility of these methods for land managers.

## **UAAS Treatment**

### *Equipment and Site Selection*

Unmanned agricultural aerial system (UAAS) treatments were conducted using a DJI Agras T-40 (Fig. 9) at the Goshen Road site. The Little Indian Creek WMA site was excluded from treatment testing due to its status as wildlife management area under a separate management plan, where UAAS operations could potentially interfere with existing management protocols, disrupt recreational activities, and negatively impact wildlife habitat quality. The Goshen Road site was selected for treatment because it was not under an active management plan and was not used for recreational purposes, making it suitable for experimental treatments.

All UAAS operations adhered to Federal Aviation Administration (FAA) Part 137 regulations, which govern agricultural aircraft operations. These regulations include requirements to operation outside of restricted airspace, maintain a minimum distance of 500 feet from man-made structures, and complete mandatory pre-flight inspections. Additionally, since the pilot in command was in the probationary period of Part 137 (having less than twenty-five hours of recorded aerial pesticide application), all flight operations strictly followed FAA regulatory guidelines for this PIC status. The West Virginia Department of Agriculture requirements were also followed, ensuring that all pesticide applications were supervised by or performed by individuals with valid pesticide applicator licenses.

### *Flight Planning*

Flight planning was conducted using the DJI SmartFarm software platform (DJI, 2025).

Three-dimensional flight maps were generated using a locally derived digital surface model (DSM) captured by the UAAS at an altitude of 20 meters. This 3-D flight mapping enabled the aircraft to navigate over varying canopy heights using a terrain-following feature. The UAAS was equipped with two front-facing NIR obstacle avoidance sensors and an active phased array radar, providing 365-degree horizontal obstacle avoidance capabilities. While the DJI Agras T-40 offered sophisticated horizontal obstacle avoidance, it lacks downward-facing obstacle sensors. This configuration prioritized horizontal obstacle avoidance, which presented limitations in environments with significant vertical canopy height variations. During treatment operations, the UAAS was programmed to maintain a height of 8.5 feet above each targeted canopy.

### *Application Rate Testing*

Prior to actual herbicide application, preliminary testing was conducted using a mixture of water and blue dye to assess coverage patterns at different application rates. This testing helped establish optimal Gallon Per Acre (GPA) rates for effective coverage. GPA is a standard measurement for aerial broadcast pesticide applications, where application rate and pesticide concentration have an inverse relationship—higher GPA rates typically require lower pesticide concentrations and vice versa. Additionally, a droplet size of 400 microns was used for all application rates.

The preliminary test revealed important considerations regarding application rates. Due to the relatively novel nature of UAAS treatments in the United States, many pesticide labels lack specific application rate guidance for this method of deployment. When GPA rates are specified on pesticide labels, they typically refer to traditional full-sized, fixed-wing agricultural aircraft

operations. The UAAS treatment approach used in this study differed from conventional broadcast spraying by selectively targeting identified autumn olive canopies rather than treating the entire area uniformly.

To address this methodological difference, a hybrid approach was developed. The treatment used pesticide concentrations appropriate for spot treatments (typically higher concentration) while applying them at various GPA rates to ensure adequate coverage. Based on the water and dye testing results, three application rates were selected for evaluation: 10 GPA, 12.5 GPA, and 15 GPA.

#### *Herbicide Formulation*

The treatment formulation consisted of three components: Triclopyr 4, Whetstone, and Liberate. Triclopyr 4 served as the primary active herbicide, selected for its effectiveness in controlling woody plants and perennial broadleaf weeds while having minimal impact on grasses. This selectivity is particularly important in reclaimed mine settings where maintaining grass cover is beneficial for soil stabilization. Whetstone, applied at a lower concentration, functioned as an adjuvant with both pre-emergent and post-emergent properties suitable for a broad spectrum of vegetation types. Liberate was included as a surfactant to enhance herbicide uptake by the target vegetation, reduce spray drift during application, and increase retention through improved adhesion and spreading of the spray solution. The concentration of these chemicals used for a 40-liter gallon tank are listed in Table 4.

Table 4: DJI Agras T-40 *Elaeagnus umbellata* treatment

	<u>Liters</u>	<u>Concentrate</u>
<i>Triclopyr 4</i>	1.6	4%
<i>Whetstone</i>	0.4	0.5%
<i>Liberate</i>	0.4	1%

### *Treatment Implementation*

The study site was divided into three treatment zones corresponding to the different application rates (10 GPA, 12.5 GPA, and 15 GPA) to evaluate efficacy across different coverage levels. The UAAS was programmed to follow a systematic flight path covering each treatment zone while selectively applying herbicide only when positioned above identified autumn olive canopies. This targeted approach minimized herbicide use and reduced potential impacts on non-target vegetation.

## **Equipment**



Figure 5: DJI Matrice 200 UAS



Figure 6: DJI Matrice 300 UAS



Figure 7: Sentera 6X Multispectral Sensor



Figure 8: Spectra Precision SP80 RTK GNSS Receiver



Figure 9: DJI Agras T-40 UAAS

## **Results**

### **Multispectral Reflectance**

Analysis of multispectral reflectance patterns revealed distinctive signatures for Autumn Olive, low vegetation, and other tree species across all spectral bands (Figs. X-X). In the NIR and the red-edge regions, Autumn Olive consistently exhibited higher reflectance compared to other tree species. The NIR band showed mean differences of 0.03-0.05 reflectance units between Autumn Olive and other trees, while the red-edge band displayed a more noticeable transition between red absorption and NIR reflection for Autumn Olive. In the visible spectrum, Autumn Olive maintained slightly higher reflectance values than other tree species but lower than low vegetation. The green peak was most pronounced in the low vegetation class, characteristic of grasses and herbaceous plants.

Spectral characteristics varied across the four phenological stages. During early-stage growth (Fig. 10), minimal separation occurred in visible bands, though Autumn Olive already showed higher NIR reflectance (0.24) than other tree species (0.20). While peak-stage (Fig. 11) showed the highest absolute reflectance values across all classes, the proportional differences between classes were not as pronounced as in other stages. Late-stage (Fig. 12) exhibited notable spectral separation, with Autumn Olive maintaining higher NIR reflectance (0.30) compared to other tree species (0.26). During senescence (Fig. 13), the greatest proportional difference in NIR reflectance was observed between Autumn Olive (0.21) and other tree species (0.16), suggesting an extended leaf-on period relative to native deciduous species.

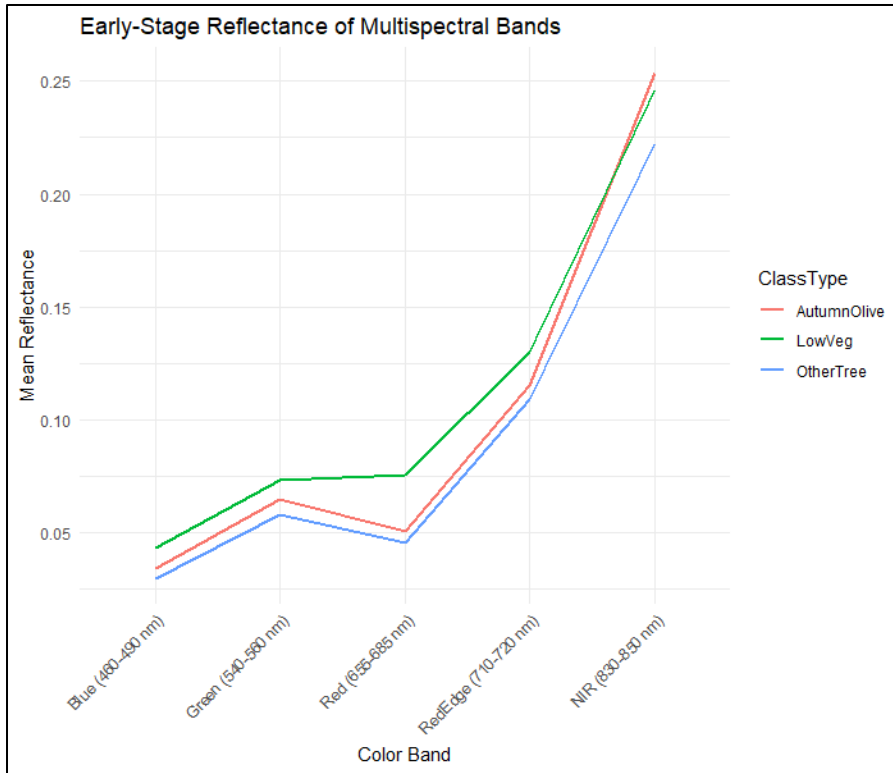


Figure 10: Early-stage mean multispectral reflectance

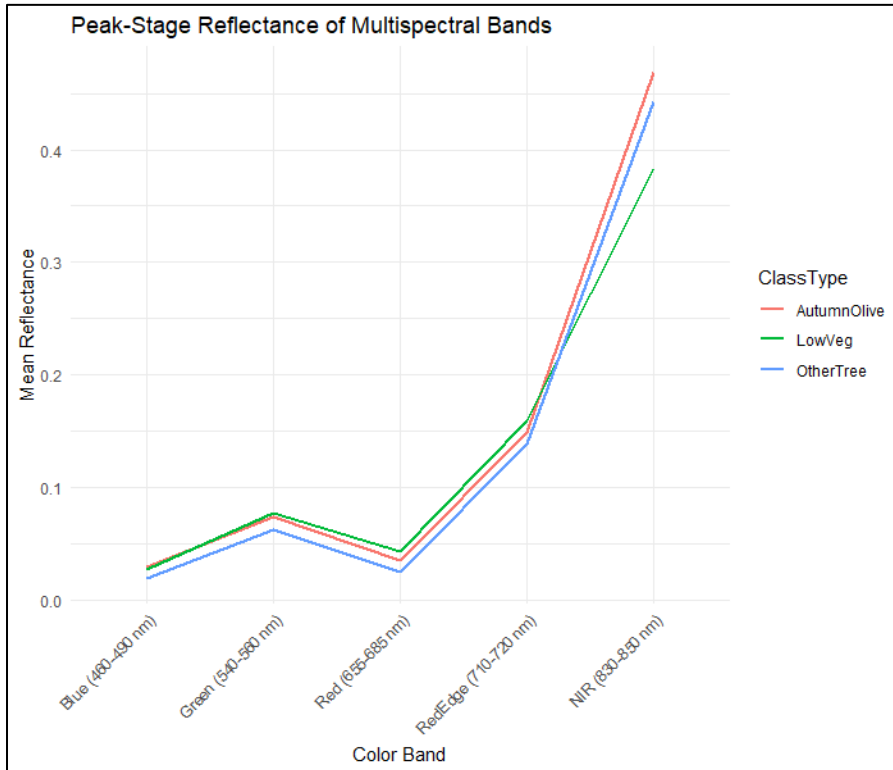


Figure 11: Peak-stage mean multispectral reflectance

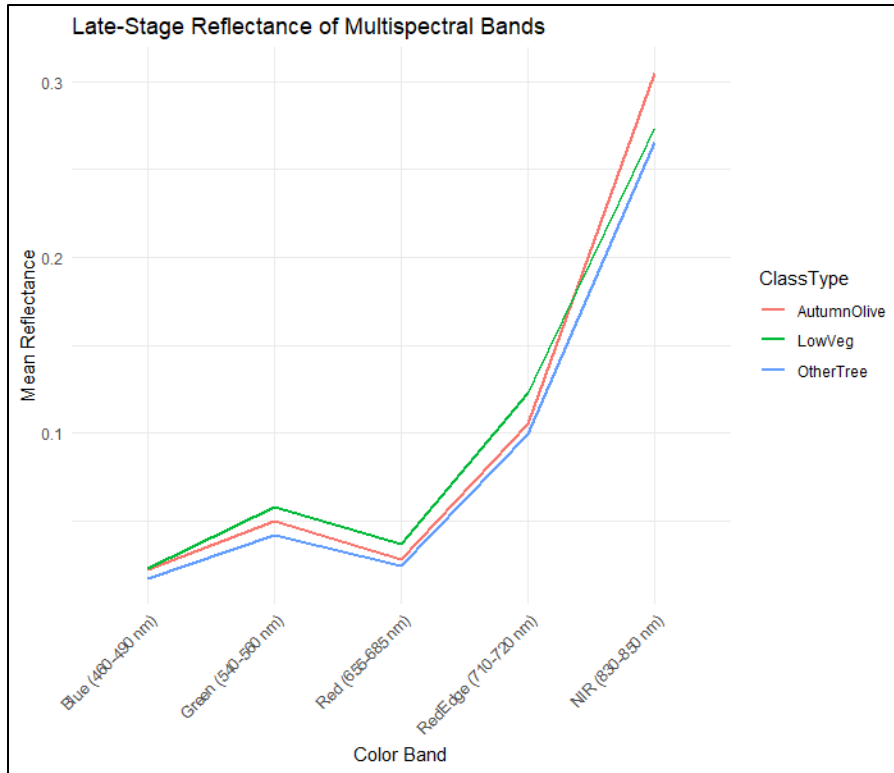


Figure 12: Late-stage mean multispectral reflectance

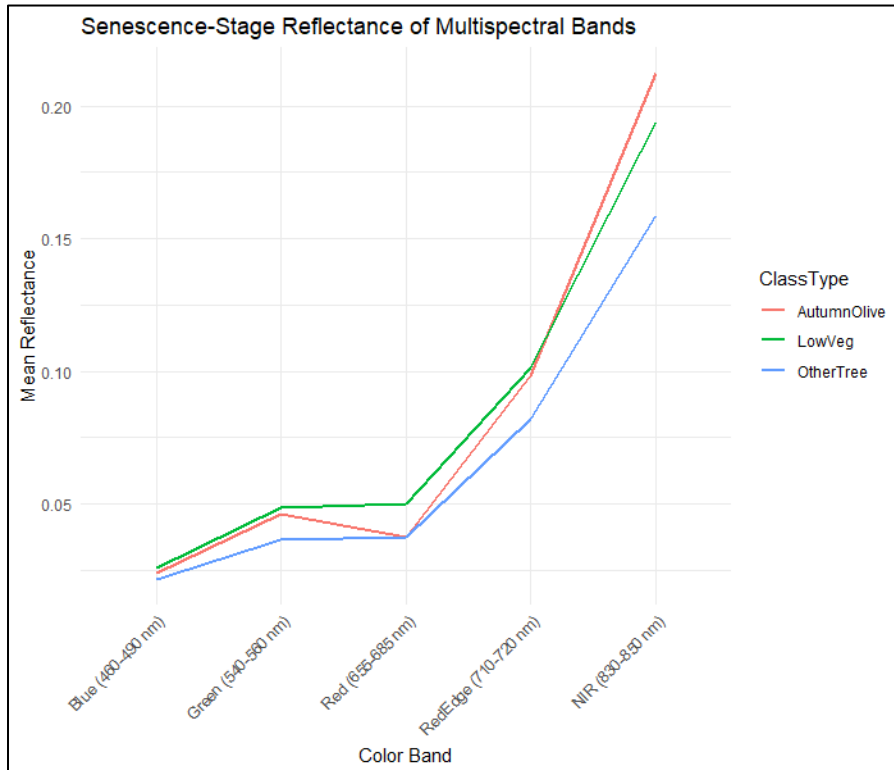


Figure 13: Senescence-stage mean multispectral reflectance

## **Vegetation Index Comparison**

### *Normalized Vegetation Indices*

The comparison of vegetation indices shows differentiating patterns that aid in discriminating autumn olive from other tree species across different phenological stages. The normalized values of 15 vegetation indices were compared between autumn olive and other tree classes to identify indices that provide optimal separation between these classes.

In the early phenological stage (Fig. 14), the evaluated indices showed that autumn olive exhibited the highest mean values for BNDVI (0.56), which was followed by NDVI (0.53). This indicates that reflectance in both the blue and red spectral regions is more robust relative to NIR. Conversely, the lowest vegetation index values for autumn olive were observed for SRI, with a value of 0.26. The other tree class exhibited similarly high values for BNDVI and GNDVI, suggesting that there is also significant reflectance differences between NIR and the visible bands for both of these classes. Differences between classes were especially evident in several indices. Autumn olive displayed consistently higher values in NDVI, NDRE, LCI, OSAVI, and RECI, implying stronger differentiation in these indices during early stages of growth. Other trees present on the sites demonstrated higher values in the GNDVI (0.50), ReGI (0.46), GCI (0.37), and CVI (0.46) indices.

In the peak phenological stage (Fig. 15), other tree species exhibited the highest values for BNDVI (0.66), OSAVI (0.64), and NDVI (0.65), indicating very strong NIR reflectance relative to the blue and red regions. This points towards a shift in the reflectance differences from the early stage. Autumn olive's highest values occurred with OSAVI (0.57) and NDVI (0.52), while the lowest values were observed for SRI (0.28). The comparative differences between the two classes became more prominent during the peak stage. Other tree species maintained higher values in

BDNVI, NDVI, OSAVI, GNDVI, EVI2, and GRVI, which may indicate greater canopy greenness during this period. Conversely, autumn olive showed higher peak-stage normalized values in NDRE (0.50), RECI (0.41), and CVI (0.45), suggesting that the red-edge indices may better distinguish autumn olive during full foliage.

During the late phenological stage (Fig. 16), autumn olive's highest values were observed for OSAVI (0.64), EVI2 (0.57), and NDVI (0.59), while the lowest occurred for ReGI (0.33). In contrast, other tree species exhibited their highest values in BNDVI (0.61), NDVI (0.59), and GNDVI (0.54), with SRI as the class's lowest at 035. Class-specific differences during the late stage reveal that autumn olive maintains stronger signals in the red-edge and chlorophyll-sensitive indices, such as NDRE, LCI, RECI, OSAVI, EVI2, and GRVI. This highlights these metrics' continued utility for distinguishing autumn olive as overall canopy reflectance begins to decline for other tree species. Conversely, other tree species exhibit the most differentiating values from autumn olive with BNDVI, GBVI, NDRE, and ReGI.

In the senescence phenological stage (Fig. 17), autumn olive exhibited its highest normalized mean value in BNDVI (0.63), GRVI (0.56), and NDVI (0.60), reflecting persistent NIR reflectance values despite some instances of observable leaf senescence. The lowest values for autumn olive were observed in ReGI and CVI, approximately 0.31, which signifies some reduction in chlorophyll indices during this period. Other tree species peaked with BNDVI (0.58), GNDVI (0.52), and NDVI (0.53), and the lowest values in SRI (0.30) and RECI (0.32). Comparing the two classes reveals that the senescence stage has distinct differences between autumn olive and other trees species present. During this stage, non-autumn olive tree species were observed to undergo phases of senescence. Where other tree species' foliage was reduced drastically or

completely and leaves would change colors, this would inevitably have a drastic impact on reflectance values in both the visible and NIR regions.

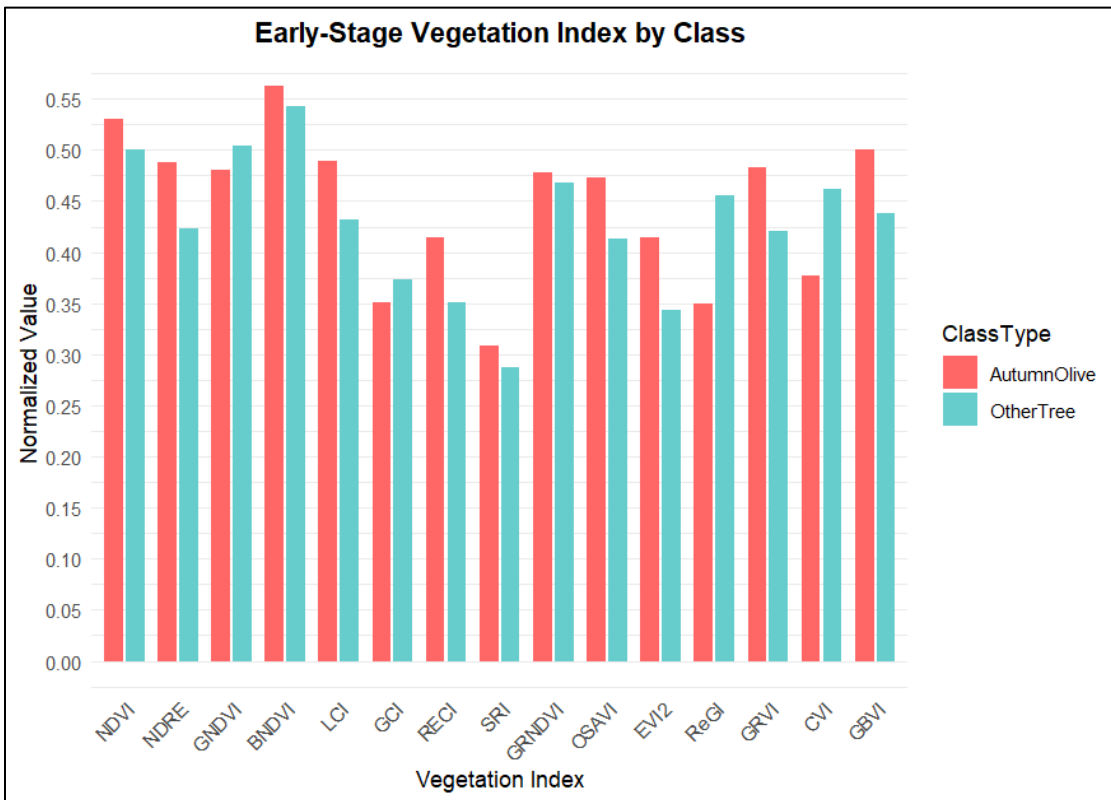


Figure 14: Early-stage mean vegetation index values

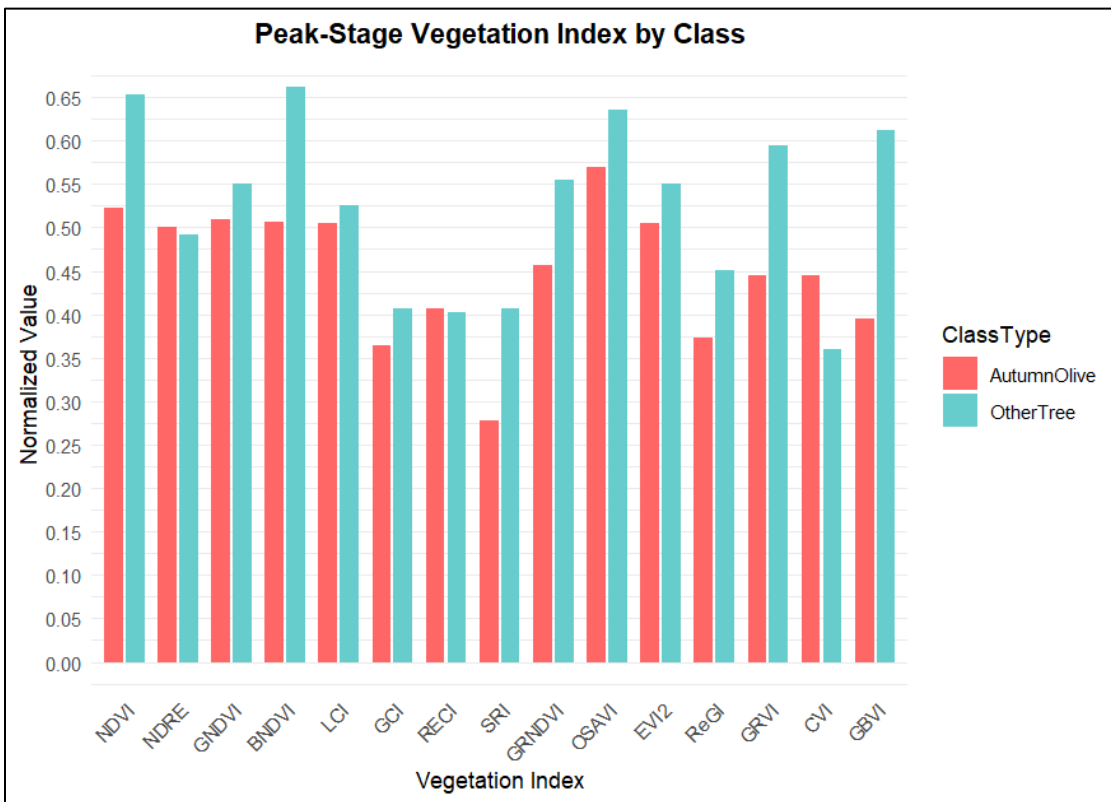


Figure 15: Peak-stage mean vegetation index values

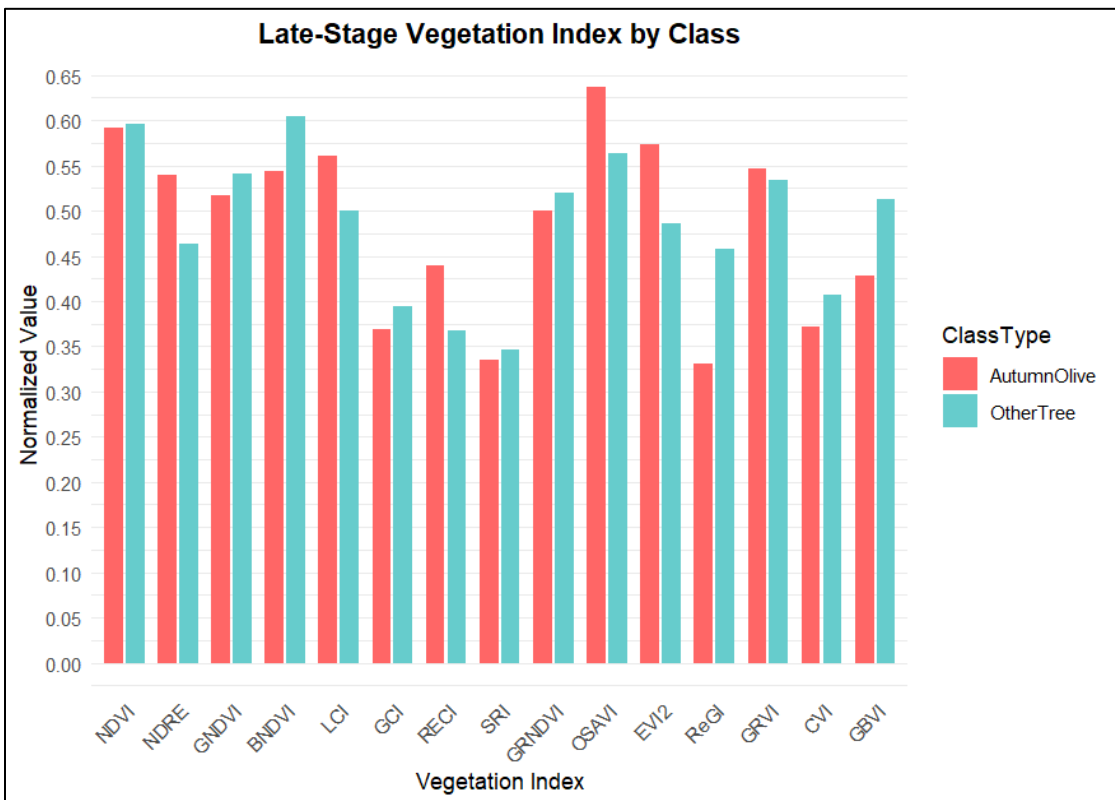


Figure 16: Late-stage mean vegetation index values

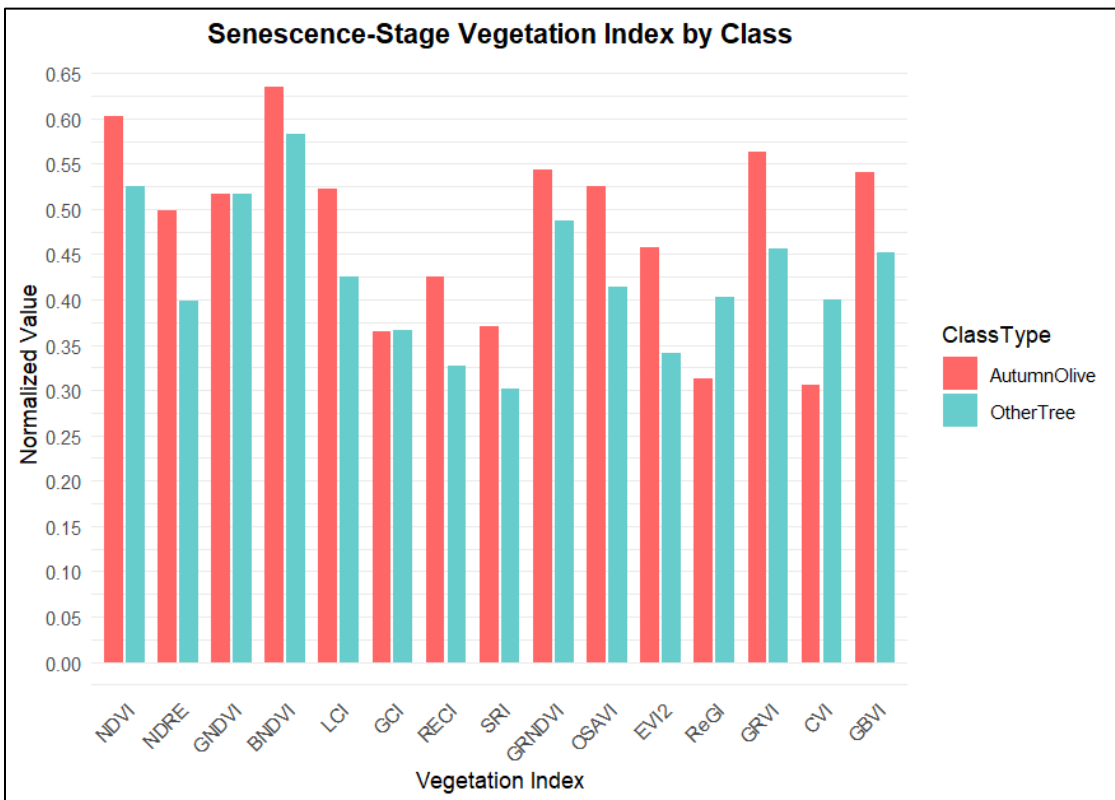


Figure 17: Senescence-stage mean vegetation index values

### *Pearson Correlation of Vegetation Indices*

To assess the stability and divergence of spectral relationships between and within the phenological stages, Pearson correlation matrices were computed for all 15 vegetation indices used. These matrices quantify how pairs of indices co-vary from early leaf emergence through senescence for autumn olive, which reveals both persistent multicollinearity and stage-specific decoupling.

During early growth (Fig. 18), NIR-derived indices (NDVI, GNDVI, BNDVI) formed a highly intercorrelated group ( $r \approx 0.90\text{-}0.98$ ), while red-edge indices (NDRE, LCI, RECI) constituted another tightly correlated cluster. Visible-band indices (GRVI, GBVI) showed lower correlations with NIR indices, indicating their complementary information value when vegetation is sparse. As vegetation reached peak development (Fig. 19), while NDVI maintained strong correlation with OSAVI, its relationship with red-edge indices weakened. Chlorophyll-sensitive indices (GCI, RECI) formed a distinct correlation group from structural indices, reflecting spectral differentiation in fully developed canopies. During late season (Fig. 20), correlation between NDVI and NDRE decreased further, while EVI2 and OSAVI maintained very high correlation ( $r > 0.95$ ), highlighting the increasing importance of red-edge information as native vegetation begins senescence. Senescence stage showed the most significant correlation restructuring (Fig. 21), with previously tight relationships between NIR and visible indices fragmenting. Red-edge indices maintained stronger internal correlations than with other groups, emphasizing their value for discriminating against autumn olive's extended leaf retention. Across all stages, certain relationships remained consistently strong (OSAVI-EVI2, NDRE-RECI), while others exhibited substantial temporal variation.

These patterns suggest that while considerable redundancy exists between certain indices, strategic combinations from different correlation clusters can maximize discriminative information for autumn olive detection, particularly during late and senescence stages when its spectral signature diverges most from native vegetation.

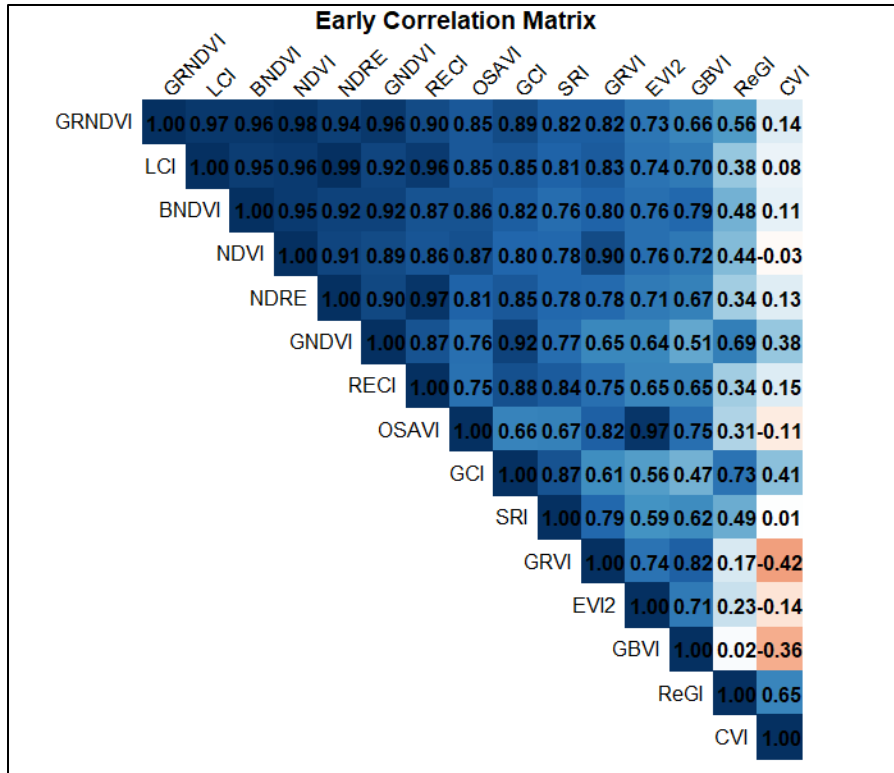


Figure 18: Early-stage vegetation index correlation

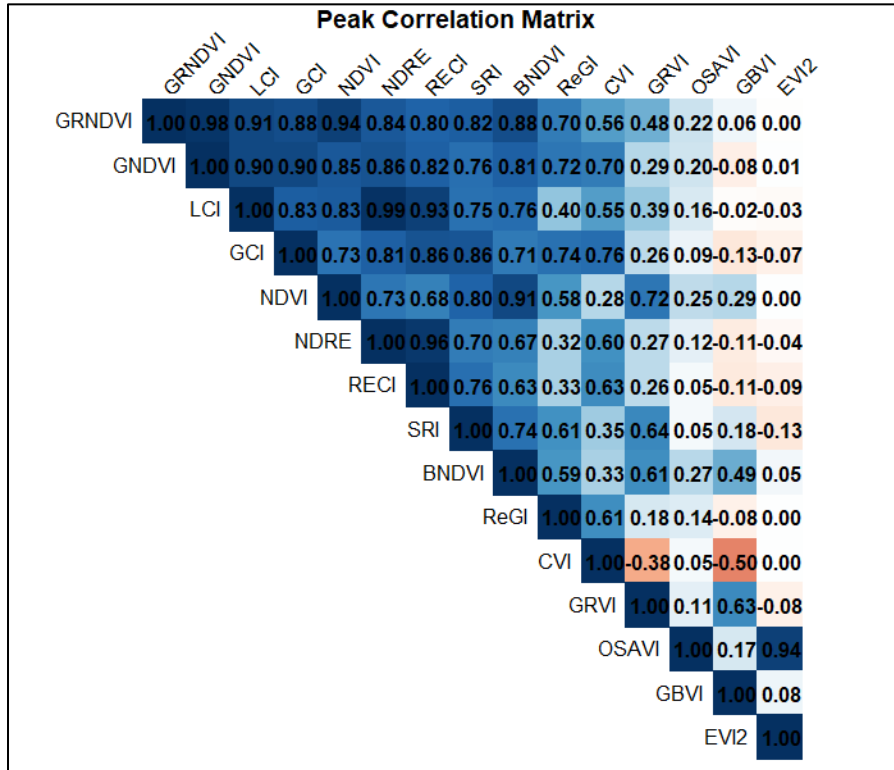


Figure 19: Peak-stage vegetation index correlation

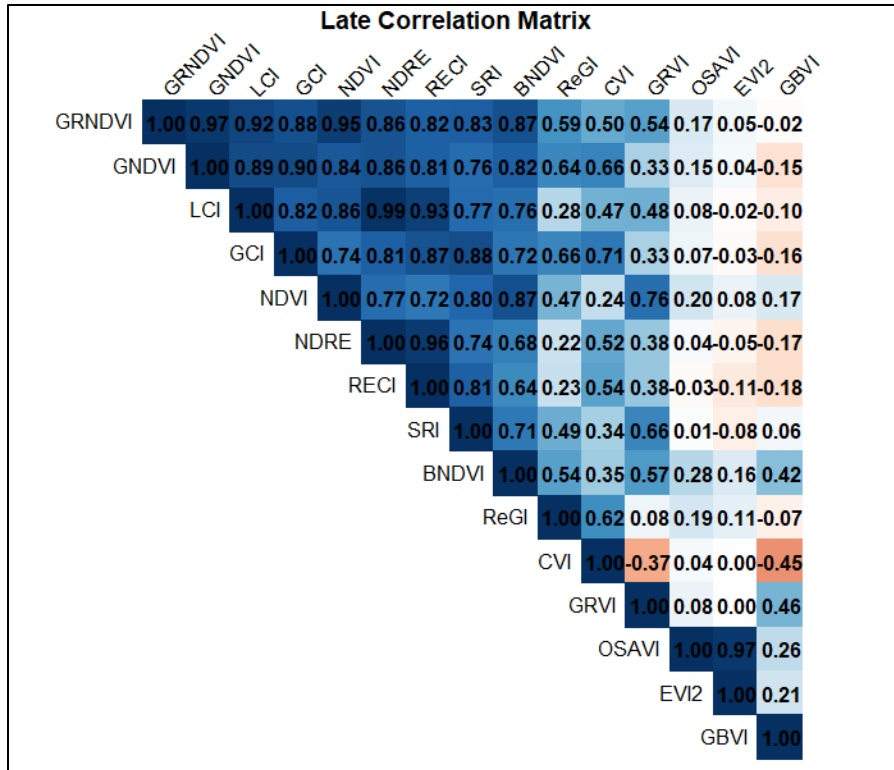


Figure 20: Late-stage vegetation index correlation

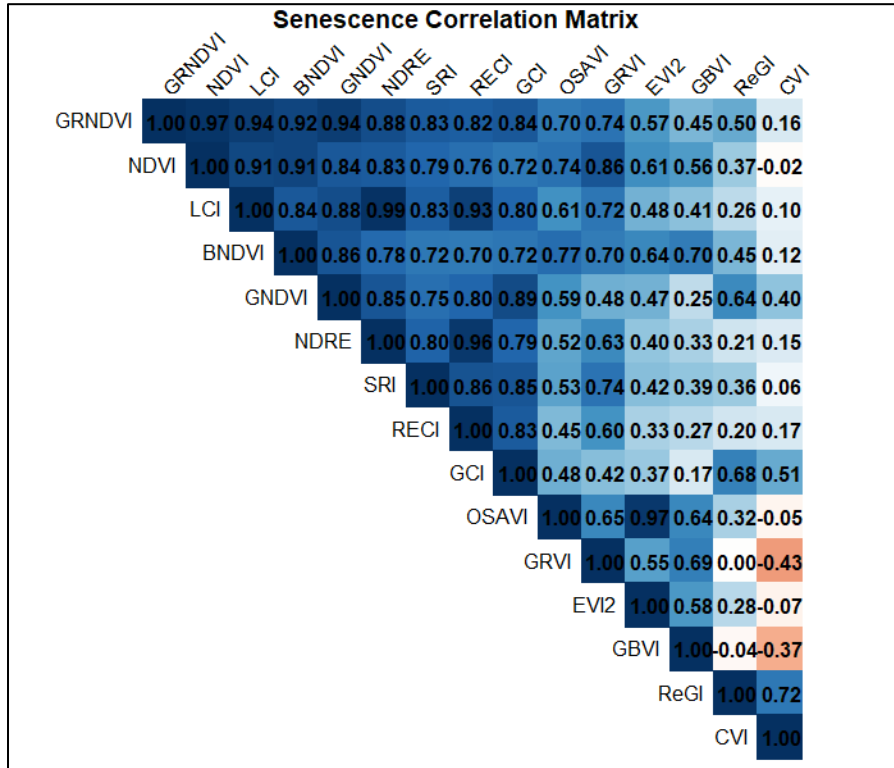


Figure 21: Senescence-stage vegetation index correlation

## **Random Forest Classification**

The Random Forest algorithm was applied to classify autumn olive and other land cover types across four phenological stages, revealing varying detection performance throughout the growing season. Classification accuracy was examined using confusion matrices and performance metrics for each stage.

During the early stage (Table 5), autumn olive was detected with moderate effectiveness, achieving a producer's accuracy of 53.5% and user's accuracy of 60.2%. The model demonstrated balanced precision and recall (0.602 and 0.535 respectively), yielding an F1-score of 0.567. Confusion was most evident between autumn olive and other vegetation classes, with 365 autumn olive points misclassified as low vegetation and 332 points misclassified as other trees.

The peak stage (Table 6) exhibited the highest detection performance for autumn olive, with a producer's accuracy of 70.3% and a user's accuracy decreased to 68.9%. The F1-score reached its maximum value of 0.696 during this stage, indicating optimal overall performance for autumn olive detection. Notably, 559 autumn olive points were misclassified the other tree class and 636 other tree points were classified as autumn olive, suggesting similar spectral characteristics between mature autumn olive and other tree species during peak foliage.

In the late stage (Table 7), autumn olive detection maintained relatively strong performance with a producer's accuracy of 64.3% and user's accuracy of 64.9%, resulting in an F1-score of 0.646. While confusion with other vegetation classes persisted, the balanced accuracy of 76.3% demonstrates the model's improved reliability during this transitional period when autumn olive maintains its foliage while other vegetation begins to senesce.

The senescence stage (Table 8) showed the weakest autumn olive detection performance, with producer's accuracy declining to 49.6% and user's accuracy to 53.3%, yielding an F1-score of 0.514. Confusion was distributed across all vegetation classes, with substantial misclassification between autumn olive and both low vegetation (382 points) and other trees (367 points). This decline in accuracy likely reflects the reduced spectral separability during late autumn when some autumn olive individuals exhibit partial senescence while retaining more foliage than most native deciduous species.

Across all phenological stages, the barren class maintained consistently high classification accuracy (>98% for both producer's and user's accuracy), demonstrating the distinct spectral signature of non-vegetated surfaces. Low vegetation and other tree classes showed moderate classification performance, with accuracy metrics generally ranging from 69% to 82%. These results indicate that autumn olive detection using Random Forest classification is most effective during peak and late phenological stages, coinciding with periods when its spectral signature diverges most significantly from other vegetation types. The temporal variation in classification performance highlights the importance of considering phenological context when developing detection strategies for this invasive species on reclaimed mine sites.

Early-Stage Random Forest Confusion Matrix		Reference Data					
		AutumnOlive	Barren	LowVeg	OtherTree	Totals	User's Accuracy
Classified Data	AutumnOlive	803	0	220	311	1334	60.2%
	Barren	0	1496	3	13	1512	98.9%
	LowVeg	365	0	1065	307	1737	61.3%
	OtherTree	332	4	212	869	1417	61.3%
	Totals	1500	1500	1500	1500		
	Producer's Accuracy	53.5%	99.7%	71.0%	57.9%		

#### Early-Stage Random Forest Performance

Class	Precision	Recall	F1-Score	Balanced Accuracy
AutumnOlive	0.602	0.535	0.567	70.9%
Barren	0.989	0.997	0.993	99.7%
LowVeg	0.613	0.710	0.658	78.0%
OtherTree	0.613	0.579	0.596	72.9%

Table 5: Early-stage random forest confusion matrix (top); Early-stage random forest performance metrics (bottom)

Peak-Stage Random Forest Confusion Matrix		Reference Data					
		AutumnOlive	Barren	LowVeg	OtherTree	Totals	User's Accuracy
Classified Data	AutumnOlive	2108	1	313	636	3058	68.9%
	Barren	1	2997	10	4	3012	99.5%
	LowVeg	332	2	2245	605	3184	70.5%
	OtherTree	559	0	432	1755	2746	63.9%
	Totals	3000	3000	3000	3000		
	Producer's Accuracy	70.3%	99.9%	74.8%	58.5%		

#### Peak-Stage Random Forest Performance

Class	Precision	Recall	F1-Score	Balanced Accuracy
AutumnOlive	0.689	0.703	0.696	79.9%
Barren	0.995	0.999	0.997	99.9%
LowVeg	0.705	0.748	0.726	82.2%
OtherTree	0.639	0.585	0.611	73.7%

Table 6: Peak-stage random forest confusion matrix (top); Peak-stage random forest performance metrics (bottom)

Late-Stage Random Forest Confusion Matrix		Reference Data					
		AutumnOlive	Barren	LowVeg	OtherTree	Totals	User's Accuracy
Classified Data	AutumnOlive	771	0	147	270	1188	64.9%
	Barren	1	1190	6	7	1204	98.8%
	LowVeg	203	6	841	313	1363	61.7%
	OtherTree	225	4	206	610	1045	58.4%
	Totals	1200	1200	1200	1200		
	Producer's Accuracy	64.3%	99.2%	70.1%	50.8%		

#### Late-Stage Random Forest Performance

Class	Precision	Recall	F1-Score	Balanced Accuracy
AutumnOlive	0.649	0.643	0.646	76.3%
Barren	0.988	0.992	0.990	99.4%
LowVeg	0.617	0.701	0.656	77.8%
OtherTree	0.584	0.508	0.543	69.4%

Table 7: Late-stage random forest confusion matrix (top); Late-stage random forest performance metrics (bottom)

Senescence-Stage Random Forest Confusion Matrix		Reference Data					
		AutumnOlive	Barren	LowVeg	OtherTree	Totals	User's Accuracy
Classified Data	AutumnOlive	744	5	321	325	1395	53.3%
	Barren	7	1480	6	17	1510	98.0%
	LowVeg	382	7	864	308	1561	55.3%
	OtherTree	367	8	309	850	1534	55.4%
	Totals	1500	1500	1500	1500		
	Producer's Accuracy	49.6%	98.7%	57.6%	56.7%		

#### Senescence-Stage Random Forest Performance

Class	Precision	Recall	F1-Score	Balanced Accuracy
AutumnOlive	0.533	0.496	0.514	67.6%
Barren	0.980	0.987	0.983	99.0%
LowVeg	0.553	0.576	0.565	71.1%
OtherTree	0.554	0.567	0.560	70.7%

Table 8: Senescence-stage random forest confusion matrix (top); Senescence-stage random forest performance metrics (bottom)

### *Permutation Importance*

Permutation importance analysis was conducted to identify the most influential vegetation indices for discriminating between classes across different phenological stages. This method measures the decrease in model performance when values of a specific feature are randomly shuffled, providing insights into which indices contribute most significantly to classification accuracy.

During the early stage (Fig. 22), the most influential indices for autumn olive detection were NDRE (0.016), RECI (0.015), and LCI (0.008). These three indices all incorporate red-edge information, suggesting that autumn olive's distinctive red-edge reflectance characteristics are particularly valuable for early-season identification. Many commonly used indices such as NDVI (-0.002), GRVI (-0.002), and BNDVI (-0.009) showed a decrease in predictive power, indicating they may actually reduce or introduce confusion to the classification accuracy for autumn olive during this stage.

As vegetation reached full development, the relative importance of indices maintained a similar pattern for autumn olive classification during peak stage (Fig. 23). LCI (0.010), NDRE (0.009), and RECI (0.008) remained the top three indices, reinforcing the value of red-edge and chlorophyll-sensitive metrics for autumn olive identification during peak foliage. Interestingly, CVI (0.002) showed positive importance at this stage despite being negative in the early stage, suggesting its increased utility during full canopy development. Meanwhile, NDVI (-0.008) and BNDVI (-0.016) showed a decrease in predictive power, indicating again that these common vegetation indices may be particularly unsuitable for autumn olive detection during peak growth.

During the late phenological stage (Fig. 24), autumn olive detection relied most heavily on NDRE (0.010) and RECI (0.009), maintaining the importance of red-edge information. Unlike

earlier stages, NDVI (0.004) showed positive importance, joining the valuable indices along with GRNDVI (0.003) and GNDVI (0.003). This shift suggests that as other vegetation begins to senesce, traditional normalized difference indices become more useful for distinguishing autumn olive, which maintains its distinctive foliage longer than native species. Blue-sensitive indices showed the strongest negative importance, with BNDVI (-0.016) and GBVI (-0.016) potentially confounding classification.

During senescence (Fig. 25), a notable shift occurred in index importance. OSAVI (0.010) and GRVI (0.008) emerged as the most important indices for autumn olive detection, with EVI2 (0.005) ranking third. This represents a substantial departure from the red-edge dominance observed in earlier stages. NDRE (0.002) and RECI (0.001) maintained positive but reduced importance. This pattern suggests that soil-adjusted and visible-band indices become more valuable during senescence, potentially because they better capture autumn olive's distinctive retention of foliage against increasingly bare landscapes as native vegetation loses leaves.

Analysis across phenological stages revealed significant temporal patterns in vegetation index importance for autumn olive detection. Red-edge indices (NDRE, RECI) consistently showed high importance during early, peak, and late stages but decreased in importance during senescence. LCI followed a similar pattern, with substantial importance in early and peak stages (0.008 and 0.010) but declining to near zero (0.0002) during senescence. In contrast, soil-adjusted indices (OSAVI, EVI2) showed negative or minimal importance during early and peak stages but emerged as top performers during senescence. OSAVI shifted from negative values in the peak stage (-0.004) to become the most important index during senescence (0.010). Chlorophyll-sensitive indices like CVI showed inconsistent patterns, with strong negative importance during early stage (-0.025), positive importance during peak and late stages (0.003 and 0.002), then

returning to negative importance during senescence (-0.009). These temporal shifts align with autumn olive's known phenological characteristics, particularly its extended leaf-retention compared to native deciduous species. As the surrounding vegetation senesces, different spectral properties become more valuable for distinguishing autumn olive from the surrounding environment.

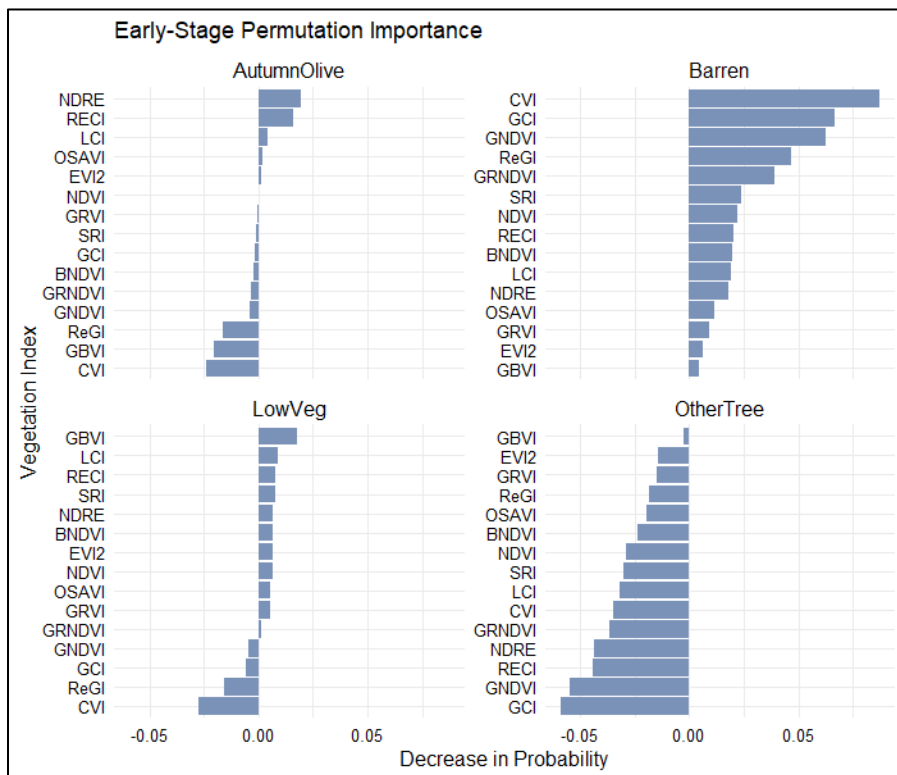


Figure 22: Early-stage permutation importance

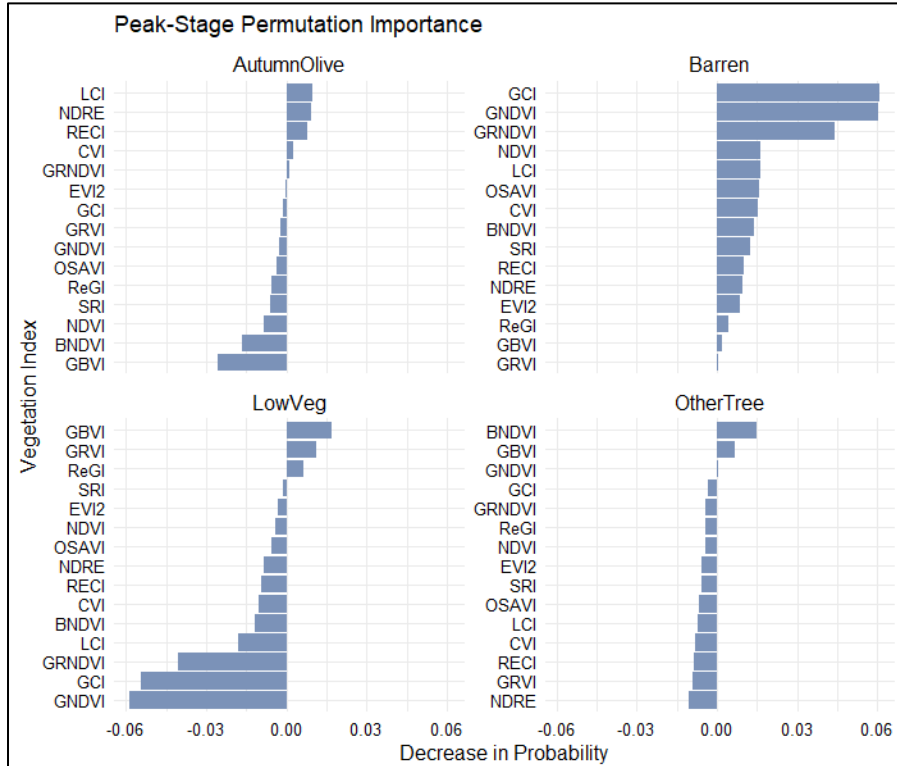


Figure 23: Peak-stage permutation importance

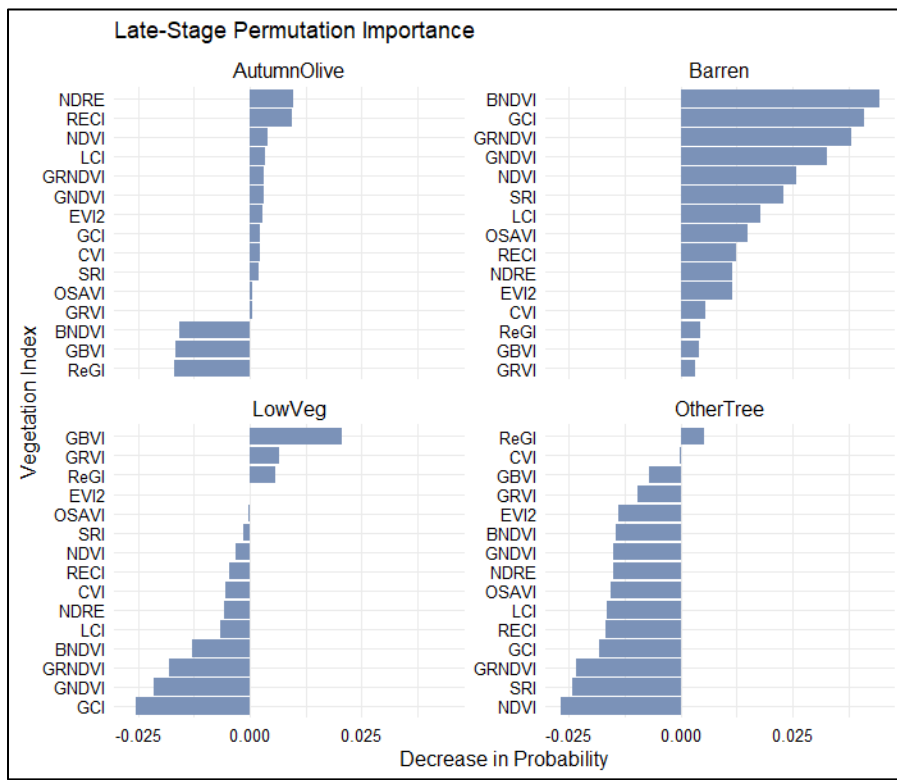


Figure 24: Late-stage permutation importance

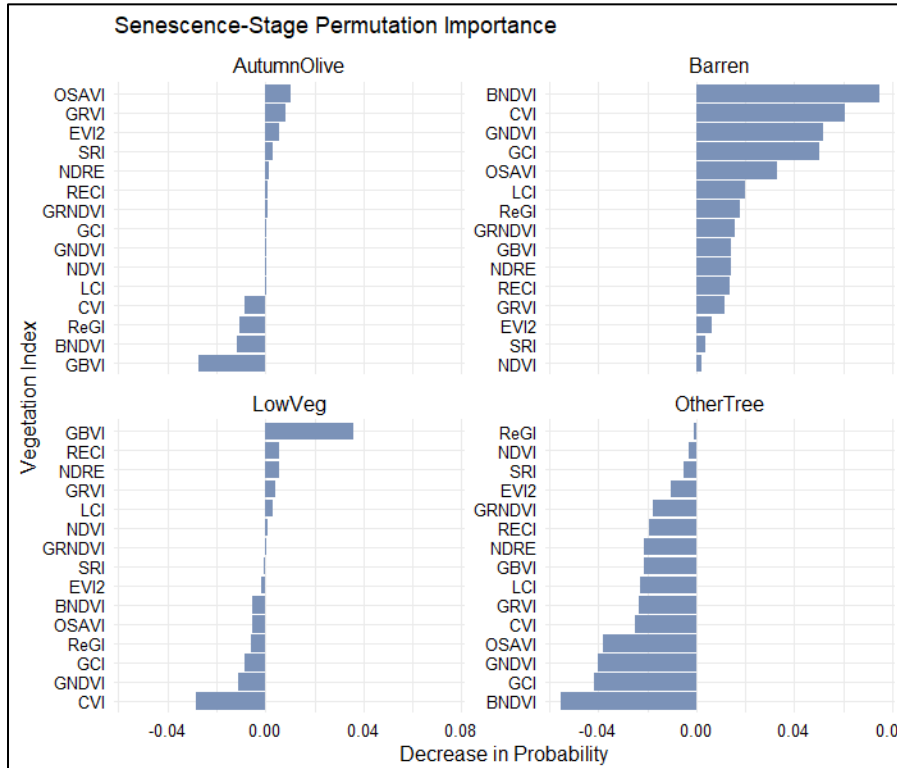


Figure 25: Senescence-stage permutation importance

### *Shapley Additive Explanations*

Shapley Additive Explanations analysis was performed to provide a comprehensive understanding of feature importance across the four phenological stages. SHAP values quantify the contribution of each predictor variable to model predictions, offering insights into which vegetation indices most strongly influence classification for each class type. This analysis revealed distinct patterns in the relative importance of vegetation indices for autumn olive detection across seasons.

During the early stage (Fig. 26), visible band-based indices dominated autumn olive detection. GBVI demonstrated the highest SHAP value (0.052) for autumn olive, followed by CVI (0.048) and ReGI (0.040). These indices emphasize the relationship between visible spectral bands, suggesting that early-stage autumn olive may exhibit distinctive pigmentation patterns compared to surrounding vegetation. Red-edge based indices NDRE (0.037), RECI (0.036), and LCI (0.033) showed moderate importance, while soil-adjusted indices OSAVI (0.017) and EVI2 (0.020) contributed least to autumn olive identification at this stage. For other tree species, GBVI (0.064), Blue (0.062), and Red (0.061) provided the strongest contributions, indicating different pigmentation patterns than autumn olive despite both being woody vegetation. The barren class was best characterized by CVI (0.057), GCI (0.054), and GNDVI (0.053), while low vegetation exhibited high dependence on CVI (0.079), GRVI (0.056), and Red (0.055).

As vegetation reached peak development (Fig. 27), BNDVI emerged as the most influential predictor for autumn olive (0.069), followed by GBVI (0.055) and red-edge indices NDRE (0.052), RECI (0.052), and LCI (0.051). This transition suggests that during peak foliage, the relationship between near-infrared and blue reflectance becomes particularly distinctive for autumn olive, potentially due to its unique leaf structure and canopy architecture. For other tree species, BNDVI

(0.068) maintained similar importance as for autumn olive, followed by GNDVI (0.042) and GBVI (0.041), showing considerable overlap in important indices despite spectral differences between tree types. The barren class showed highest dependence on BNDVI (0.073) and GNDVI (0.059), while low vegetation classification relied primarily on BNDVI (0.061), LCI (0.056), and NDRE (0.053).

The late phenological stage (Fig. 28) revealed another significant shift in feature importance. For autumn olive detection, red-edge indices emerged as dominant predictors, with LCI (0.057), NDRE (0.055), and RECI (0.055) showing the highest SHAP values. This strong importance of red-edge indices coincides with the beginning of senescence in native vegetation, highlighting autumn olive's extended photosynthetic activity compared to native species. Other tree species showed highest dependence on GCI (0.050), BNDVI (0.049), and GNDVI (0.047), with notably lower importance for red-edge indices compared to autumn olive. The barren class continued to be best characterized by BNDVI (0.059), GCI (0.043), and GRNDVI (0.042), while low vegetation classification relied heavily on BNDVI (0.061), GCI (0.048), and LCI (0.046).

The most dramatic redistribution of feature importance occurred during the senescence stage (Fig. 29). For autumn olive detection, visible-band indices regained dominance, with GBVI (0.081), GRVI (0.071), and BNDVI (0.068) providing the strongest contributions, substantially higher than during any previous stage. This marked increase in visible-band importance likely captures the stark contrast between autumn olive's retained green foliage and the senescent or leafless state of surrounding vegetation. Other tree species showed a similar pattern with GBVI (0.095), GRVI (0.065), and BNDVI (0.061) providing the strongest contributions, though with higher overall SHAP values for GBVI compared to autumn olive. The barren class showed

exceptionally high dependence on BNDVI (0.109), CVI (0.047), and GCI (0.039), while low vegetation was most strongly influenced by GBVI (0.110), GRVI (0.084), and BNDVI (0.062).

This temporal evolution in feature importance aligns with autumn olive's distinctive phenological characteristics. Visible-band indices (GBVI, GRVI) are most effective during early growth and senescence when autumn olive's foliage contrasts against other vegetation, while red-edge indices (NDRE, RECI, LCI) peak in importance during late stage when autumn olive maintains photosynthetic activity as native vegetation declines. While BNDVI showed strong importance across multiple seasons, the dramatic shifts in relative index importance suggest that detection models would benefit from season-specific approaches that emphasize different spectral features as autumn olive and surrounding vegetation progress through their growing cycles.

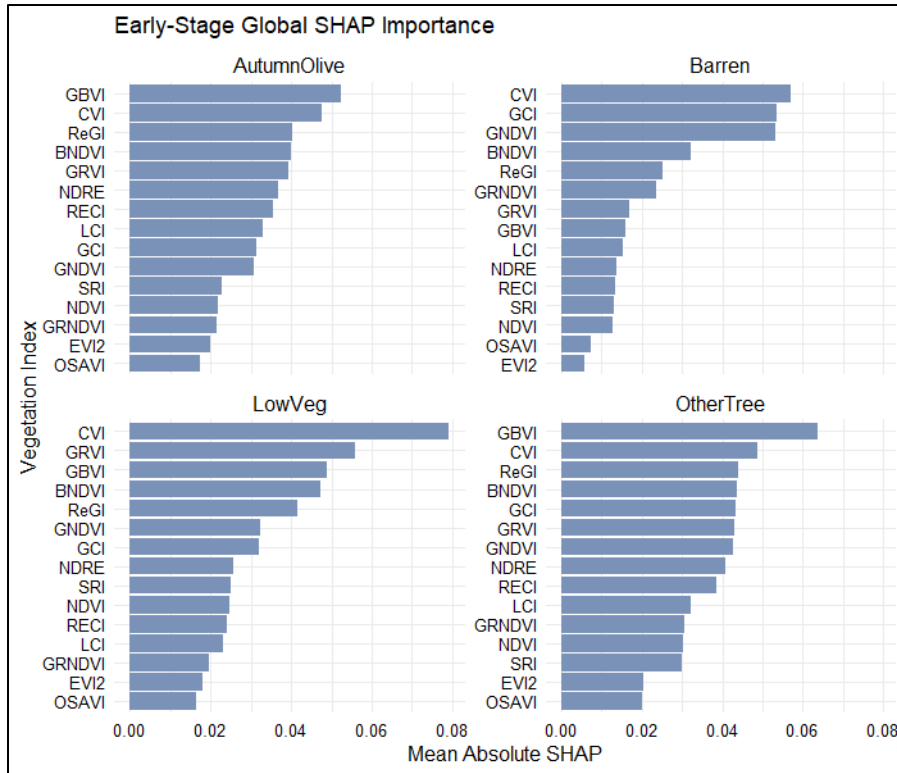


Figure 26: Early-stage SHAP importance

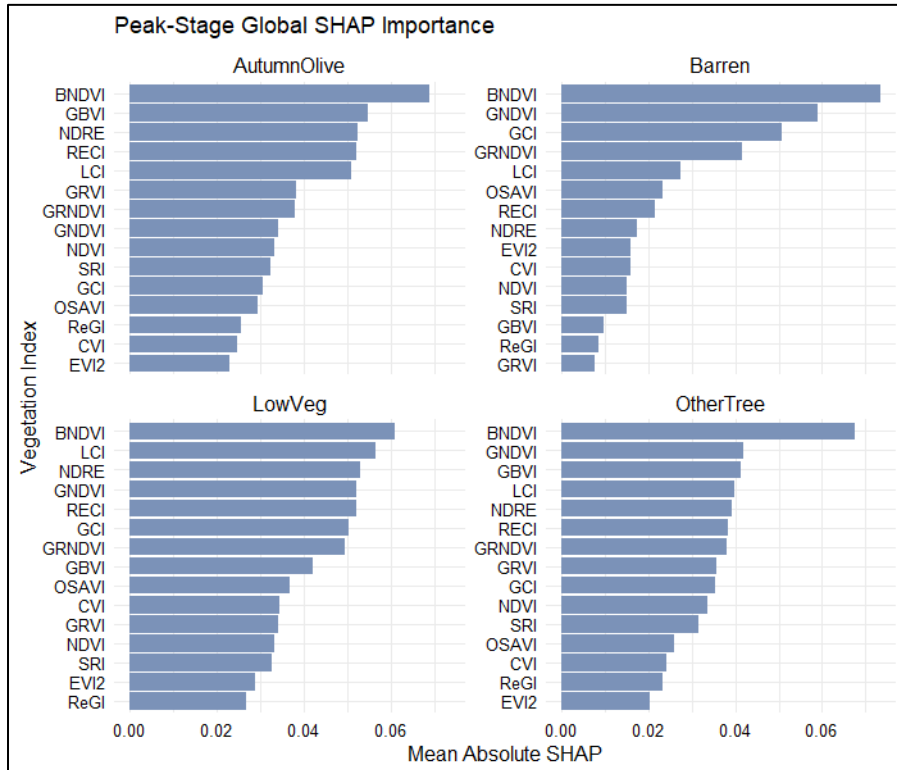


Figure 27: Peak-stage SHAP importance

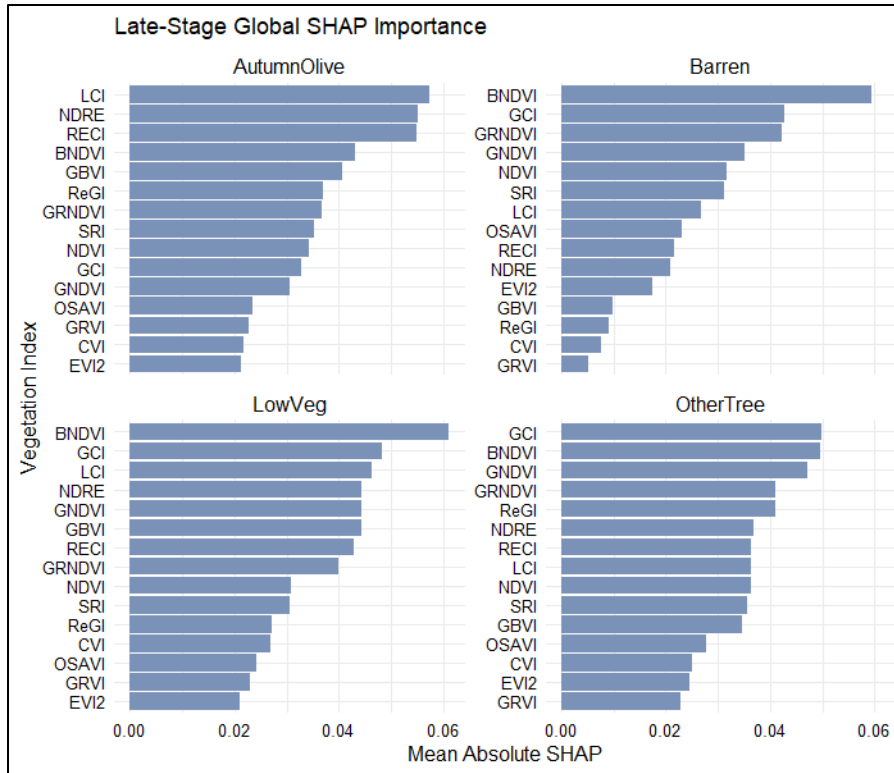


Figure 28: Late-stage SHAP importance

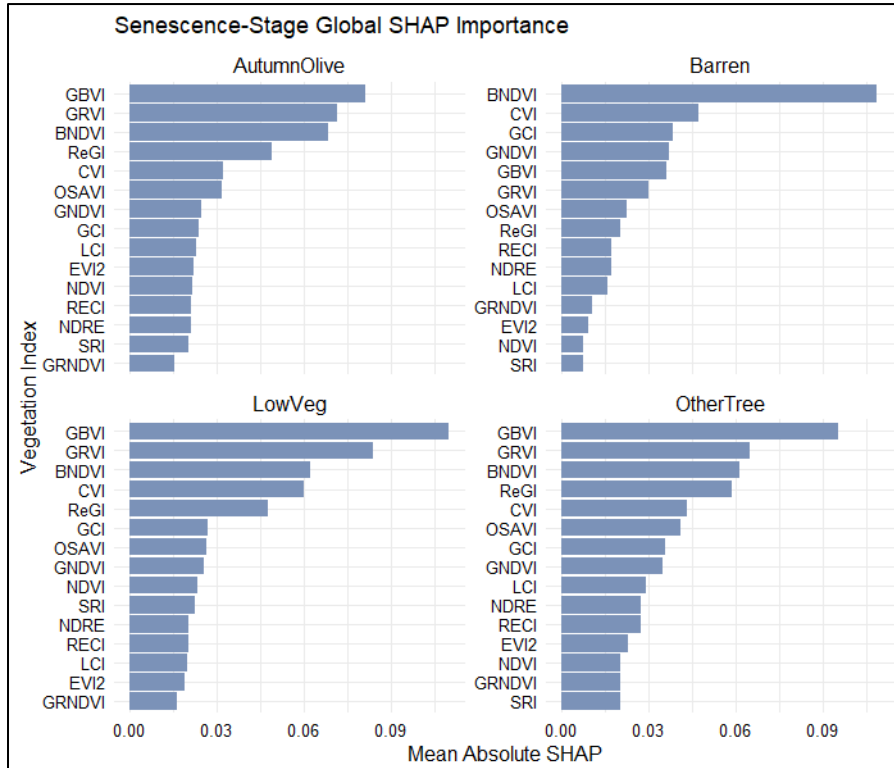


Figure 29: Senescence-stage SHAP importance

## Feature Selection

Based on permutation and SHAP importance analyses, we selected three vegetation indices for each phenological stage to pair with multispectral bands in our VI-Composite U-Net model (Table 9). For the early stage, GBVI, NDRE, and LCI were chosen, capturing both visible band relationships and red-edge characteristics during initial leaf development. Peak stage selections included BNDVI, GBVI, and GRVI, which effectively distinguish autumn olive at maximum foliage development. The late stage utilized red-edge indices exclusively (LCI, NDRE, and RECI), aligning with autumn olive's extended photosynthetic activity compared to the senescing native vegetation. During senescence, GBVI, GRVI, and NDRE were selected to capture the contrast between autumn olive's retained foliage and surrounding leafless vegetation. These stage-specific indices were integrated with the five multispectral bands to create an 8-band input for our models.

Table 9: Selected vegetation indices for VI-Composite U-Net

Early	Peak	Late	Senescence
GBVI	BNDVI	LCI	GBVI
NDRE	GBVI	NDRE	GRVI
LCI	GRVI	RECI	NDRE

## **U-Net Classification**

The U-Net architecture was employed to perform semantic segmentation for autumn olive detection across different phenological stages. Three model variants were developed and evaluated: a multispectral U-Net utilizing 5-band imagery, a vegetation index composite U-Net (VI-Composite) combining spectral bands with selected vegetation indices, and an RGB U-Net using the standard 3-band imagery. Each model was trained independently for early, peak, late, and senescence phenological stages to evaluate detection performance across the growing seasons.

### *Multispectral U-Net Classification*

The Multispectral U-Net model, which utilized all five spectral bands (Blue, Green, Red, Red-Edge, and NIR) as input, demonstrated strong performance across all phenological stages. Tables X-X illustrates the training and validation metrics for this model variant across the four seasonal stages. Training convergence was varied for each phenological stage, with the early stage improved until the 196<sup>th</sup> epoch, peak stage improved until the 103<sup>rd</sup> epoch, late stage improved until the 19<sup>th</sup> epoch, and senescence improved until the 13<sup>th</sup> epoch.

In the early stage, the Multispectral U-Net achieved an overall accuracy of 96.9% and a weighted F1-score of 0.970 (Table 10). Class-specific performance metrics revealed that autumn olive was detected with 87.0% precision and 95.5% recall, resulting in an F1-score of 0.911. This performance indicates effective discrimination between autumn olive and other vegetation types during early leaf development. Missclassification primarily occurred between autumn olive and other tree species, with approximately 384,711 autumn olive pixels incorrectly classified as other trees, and 718,913 other tree pixels misclassified as autumn olive.

The peak phenological stage marked the highest performance for autumn olive detection, with the model achieving an overall accuracy of 96.0% and a weighted F1-score of 0.960 (Table

11). For the autumn olive class specifically, the model demonstrated 88.7% precision and 94.1% recall, yielding an F1-score of 0.913. Of the 18,727,724 autumn olive pixels, 17,613,663 were correctly classified (94.1%), while 449,430 were incorrectly classified as low vegetation and 664,415 as other trees. Conversely, the model incorrectly identified 993,822 other tree pixels and 1,247,110 low vegetation pixels as autumn olive. This superior performance during peak season likely reflects autumn olive's distinctive spectral signature during this stage, particularly the higher reflectance in the NIR region compared to other vegetation types.

In the late phenological stage, classification performance declined slightly with an overall accuracy of 93.2% and a weighted F1-score of 0.933 (Table 12). The model maintained strong discrimination capability for autumn olive with 80.7% precision and 88.4% recall (F1-score of 0.844). The confusion matrix shows that of the 10,697,371 autumn olive pixels, 9,454,715 were correctly classified (88.4%), while 501,890 were misclassified as low vegetation and 740,556 as other trees. Additionally, the model incorrectly classified 892,868 low vegetation pixels and 1,369,909 other tree pixels as autumn olive. This increased confusion may be attributed to the beginning of early senescence in some tree species while autumn olive maintains its foliage, creating more complex spectral patterns across the landscape.

During senescence, when most deciduous vegetation has lost leaves, classification became more challenging. The model achieved 92.0% overall accuracy with a weighted F1-score of 0.921. Autumn olive detection performance dropped to 75.9% precision and 84.5% recall (F1-score of 0.799) (Table 13), representing the lowest seasonal performance among all stages. Substantial misclassification occurred between autumn olive and other tree species, with 1,173,710 autumn olive pixels incorrectly classified as other trees and 1,577,481 other tree pixels misclassified as autumn olive. This confusion likely stems from the differing leaf retention patterns across different

species during senescence, creating highly heterogeneous spectral responses that complicate class discrimination.

Barren and low vegetation classes consistently achieved very high classification accuracy (>94% F1-scores) across all phenological stages, indicating clear spectral separation from woody vegetation types. This finding suggests that distinguishing non-woody from woody vegetation is relatively straightforward using multispectral imagery, while separating different woody vegetation types presents a greater challenge.

The learning curves (Figs. 30-33) show mildly stable convergence for all seasonal models with minimal divergence between training and validation metrics, indicating good generalization capabilities. Interestingly, the models for later phenological stages (late and senescence) converged much faster than those for earlier stages, possibly due to stronger spectral contrasts between vegetation types during these periods as leaf loss creates more distinctive patterns. The early-stage model required 196 epochs to reach highest performance, while the senescence stage model achieved its best results after just 13 epochs.

When examining the classification maps (Figs. 34-37), notable differences in autumn olive detection are evident across phenological stages. The early-stage classification (Fig. 34) shows relatively clean delineation with over-prediction beyond annotated boundaries. During peak growing season (Fig. 35), autumn olive detection appears most consistent, with well-defined patch boundaries and strong agreement between predicted and annotated regions. The late stage (Fig. 36) shows increased commission errors. The senescence stage classification (Fig. 37) displays the most inconsistencies, with increased commission errors and less distinct boundaries.

Early-Stage Multispec U-Net Confusion Matrix		Reference Data					
		AutumnOlive	Barren	LowVeg	OtherTree	Totals	User's Accuracy
Classified Data	AutumnOlive	10291672	0	821645	718913	11832230	87.0%
	Barren	1019	3032333	945	26902	3061199	99.1%
	LowVeg	95352	0	60053010	302514	60450876	99.3%
	OtherTree	384711	250	531176	17301604	18217741	95.0%
	Totals	10772754	3032583	61406776	18349933		
	Producer's Accuracy	95.5%	99.9%	97.8%	94.3%		

#### Early-Stage Multispec U-Net Performance

Class	Precision	Recall	F1-Score	Model Accuracy
AutumnOlive	0.870	0.955	0.911	96.9%
Barren	0.991	1.000	0.995	
LowVeg	0.993	0.978	0.986	
OtherTree	0.950	0.943	0.946	
Weighted Average	0.971	0.969	0.970	

Table 10: Early-stage Multispec U-Net confusion matrix (top); Early-stage Multispec U-Net performance metrics (bottom)

Peak-Stage Multispec U-Net Confusion Matrix		Reference Data					
		AutumnOlive	Barren	LowVeg	OtherTree	Totals	User's Accuracy
Classified Data	AutumnOlive	17613663	330	1247110	993822	19854925	88.7%
	Barren	216	2302579	101724	23831	2428350	94.8%
	LowVeg	449430	56622	128035074	1553574	130094700	98.4%
	OtherTree	664415	8529	2747131	40395360	43815435	92.2%
	Totals	18727724	2368060	132131039	42966587		
	Producer's Accuracy	94.1%	97.2%	96.9%	94.0%		

#### Peak-Stage Multispec U-Net Performance

Class	Precision	Recall	F1-Score	Model Accuracy
AutumnOlive	0.887	0.941	0.913	96.0%
Barren	0.948	0.986	0.960	
LowVeg	0.984	0.969	0.977	
OtherTree	0.922	0.940	0.931	
Weighted Average	0.961	0.960	0.960	

Table 11: Peak-stage Multispec U-Net confusion matrix (top); Peak-stage Multispec U-Net performance metrics (bottom)

Late-Stage Multispec U-Net Confusion Matrix		Reference Data					
		AutumnOlive	Barren	LowVeg	OtherTree	Totals	User's Accuracy
Classified Data	AutumnOlive	9454715	210	892868	1369909	11717702	80.7%
	Barren	210	1704714	14801	15109	1734834	98.3%
	LowVeg	501890	27315	63308908	948675	64786788	97.7%
	OtherTree	740556	7231	2331200	18893274	21972261	86.0%
	Totals	10697371	1739470	66547777	21226967		
Producer's Accuracy		88.4%	98.0%	95.1%	89.0%		

#### Late-Stage Multispec U-Net Performance

Class	Precision	Recall	F1-Score	Model Accuracy
AutumnOlive	0.807	0.884	0.844	93.2%
Barren	0.983	0.980	0.981	
LowVeg	0.977	0.951	0.964	
OtherTree	0.860	0.890	0.875	
Weighted Average	0.934	0.932	0.933	

Table 12: Late-stage Multispec U-Net confusion matrix (top); Late-stage Multispec U-Net performance metrics (bottom)

Senescence-Stage Multispec U-Net Confusion Matrix		Reference Data					
		AutumnOlive	Barren	LowVeg	OtherTree	Totals	User's Accuracy
Classified Data	AutumnOlive	8112927	462	1003813	1577481	10694683	75.9%
	Barren	1514	1079356	20078	111627	1212575	89.0%
	LowVeg	314173	6012	61405950	1167862	62893997	97.6%
	OtherTree	1173710	2	2416757	18656836	22247305	83.9%
	Totals	9602324	1085832	64846598	21513806		
Producer's Accuracy		84.5%	99.4%	94.7%	86.7%		

#### Senescence-Stage Multispec U-Net Performance

Class	Precision	Recall	F1-Score	Model Accuracy
AutumnOlive	0.759	0.845	0.799	92.0%
Barren	0.890	0.994	0.939	
LowVeg	0.976	0.947	0.961	
OtherTree	0.839	0.867	0.853	
Weighted Average	0.923	0.920	0.921	

Table 13: Senescence-stage Multispec U-Net confusion matrix (top); Senescence-stage Multispec U-Net performance metrics (bottom)

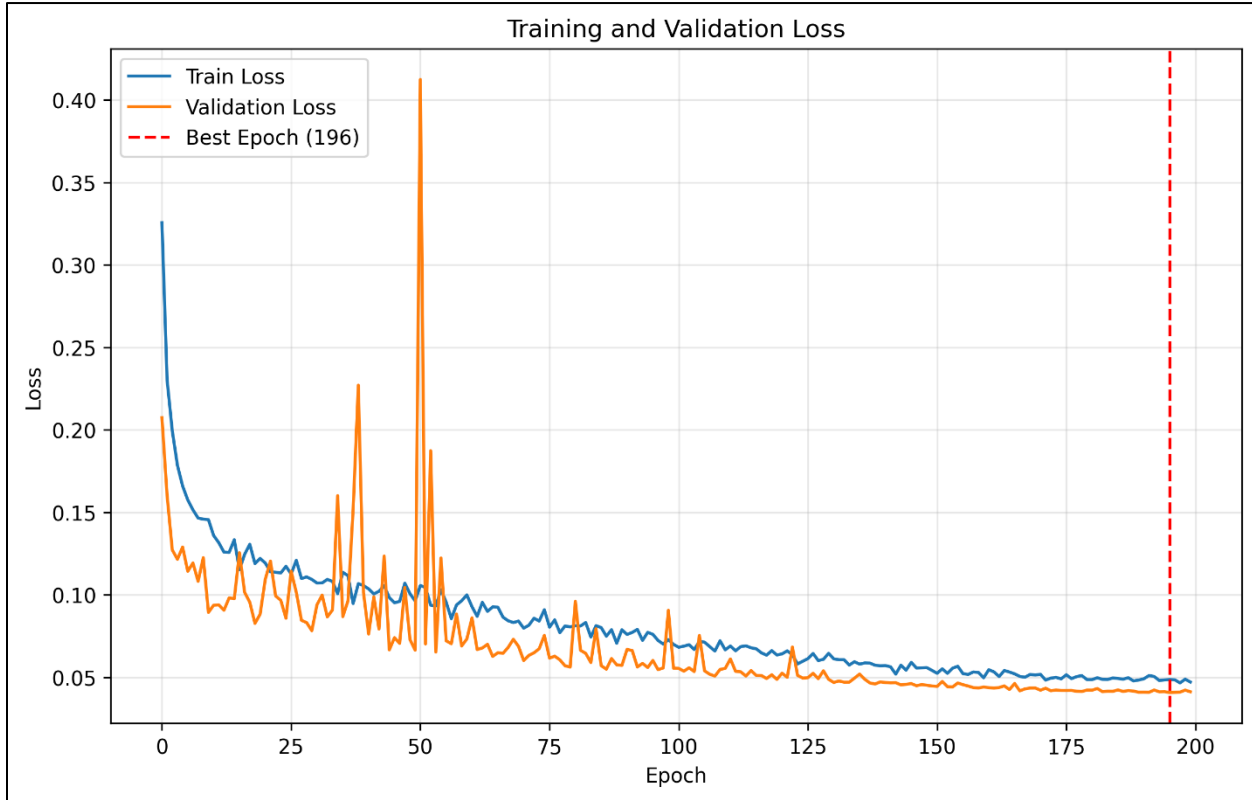


Figure 30: Early-stage Multispec U-Net loss

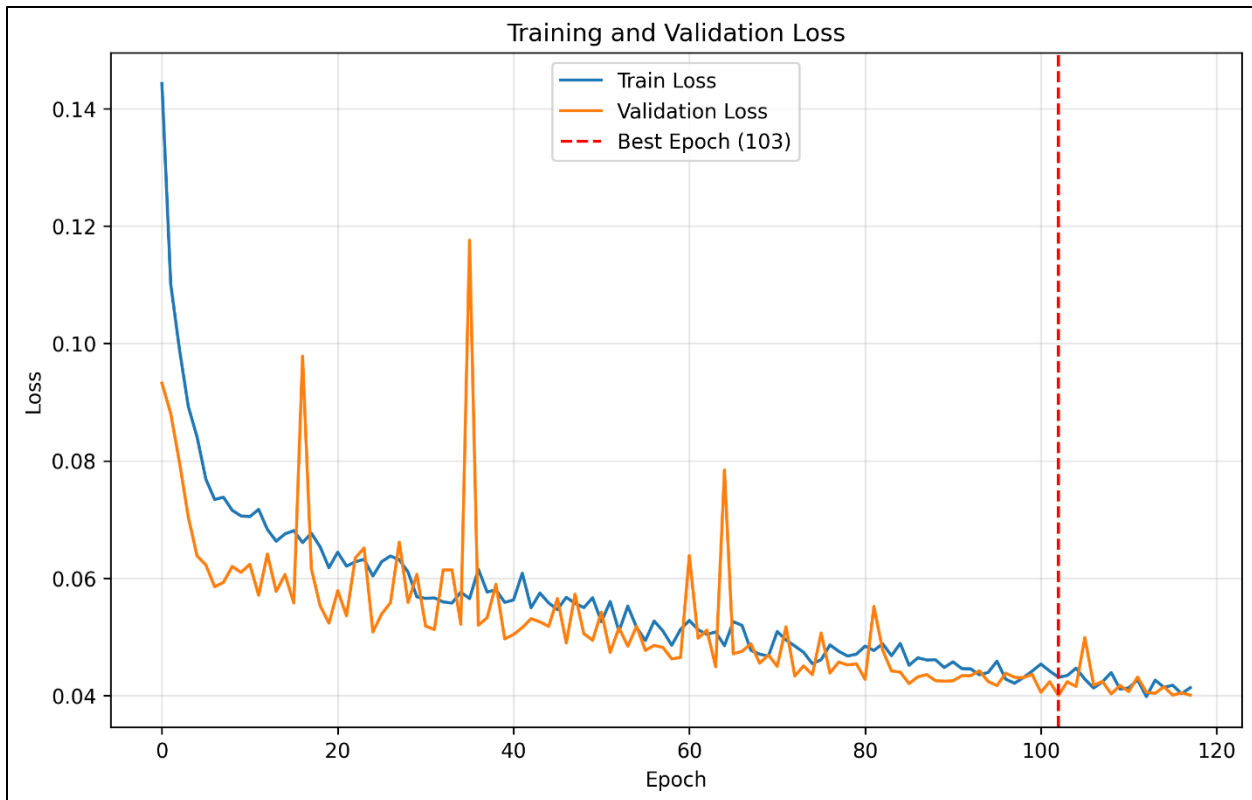


Figure 31: Peak-stage Multispec U-Net loss



Figure 32: Late-stage Multispec U-Net loss

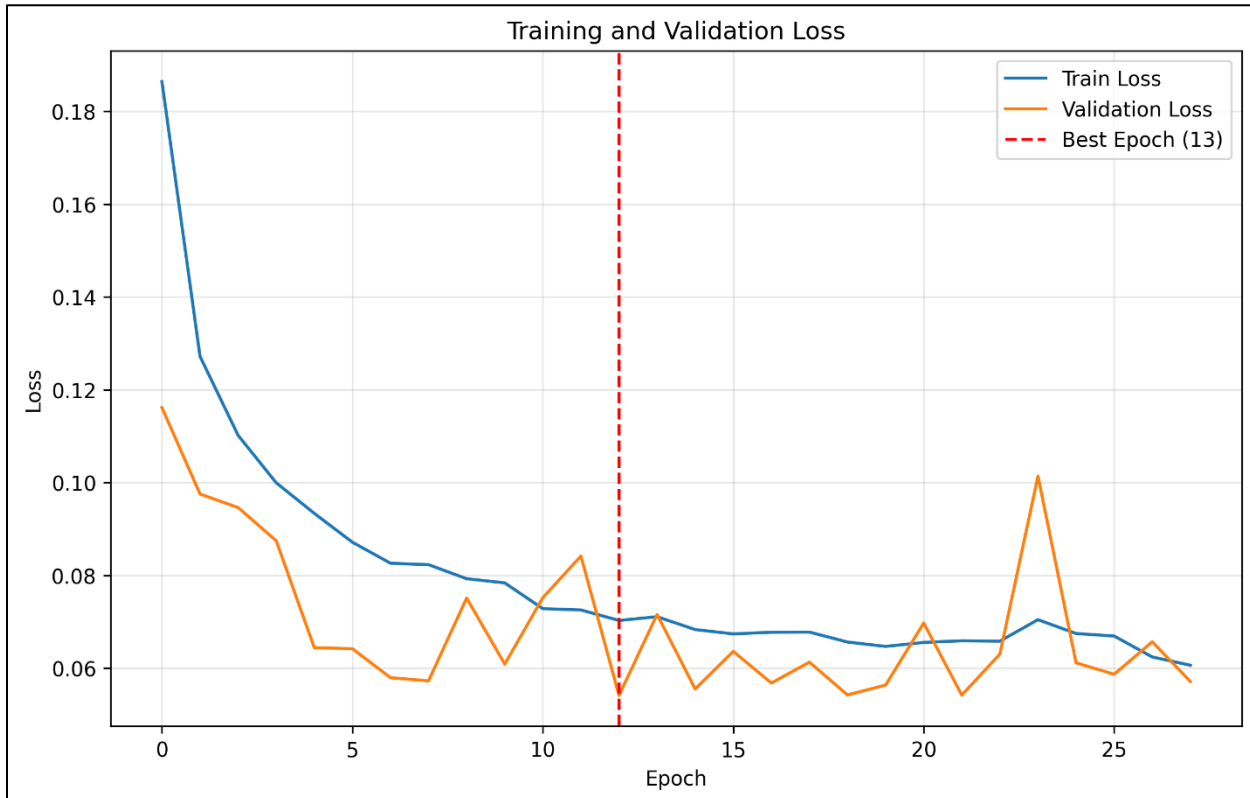


Figure 33: Senescence-stage Multispec U-Net loss

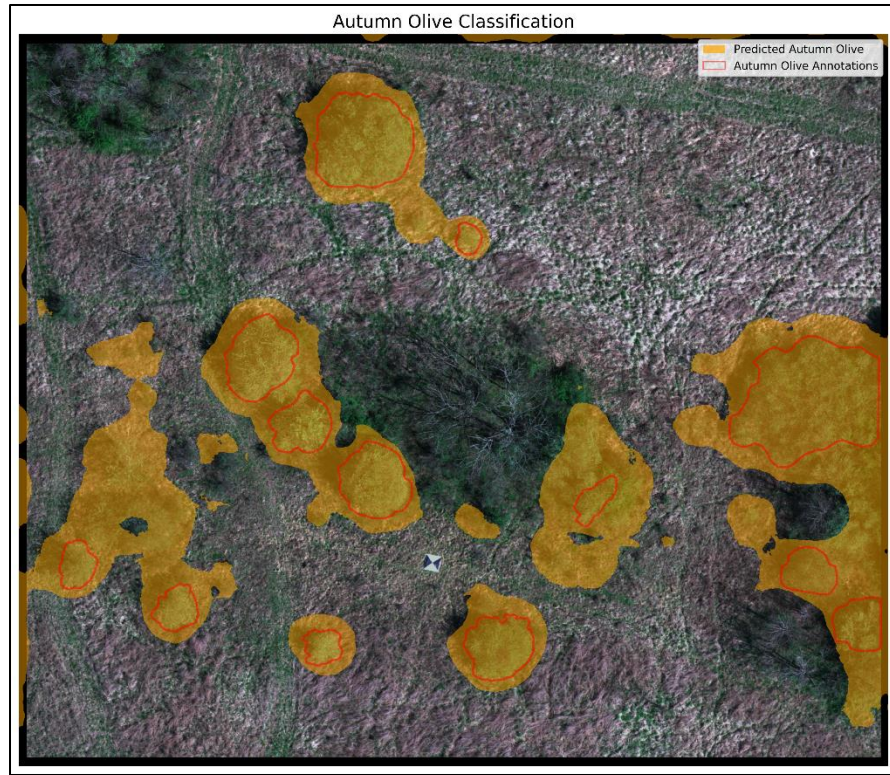


Figure 34: Early-stage Multispec U-Net classification (4/13/2023)

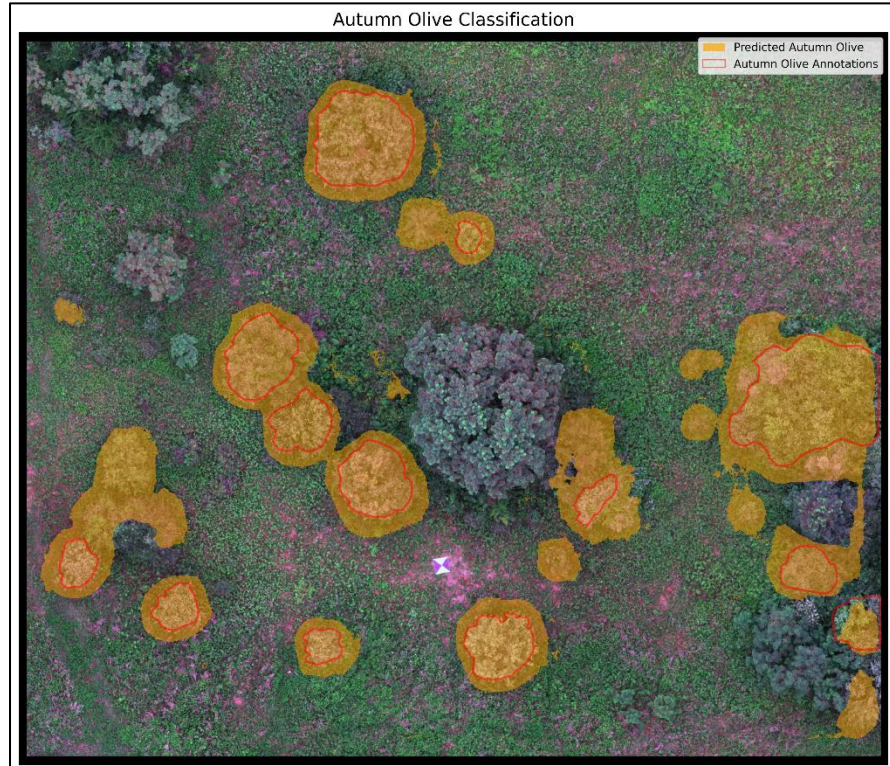


Figure 35: Peak-stage Multispec U-Net classification (7/19/2023)

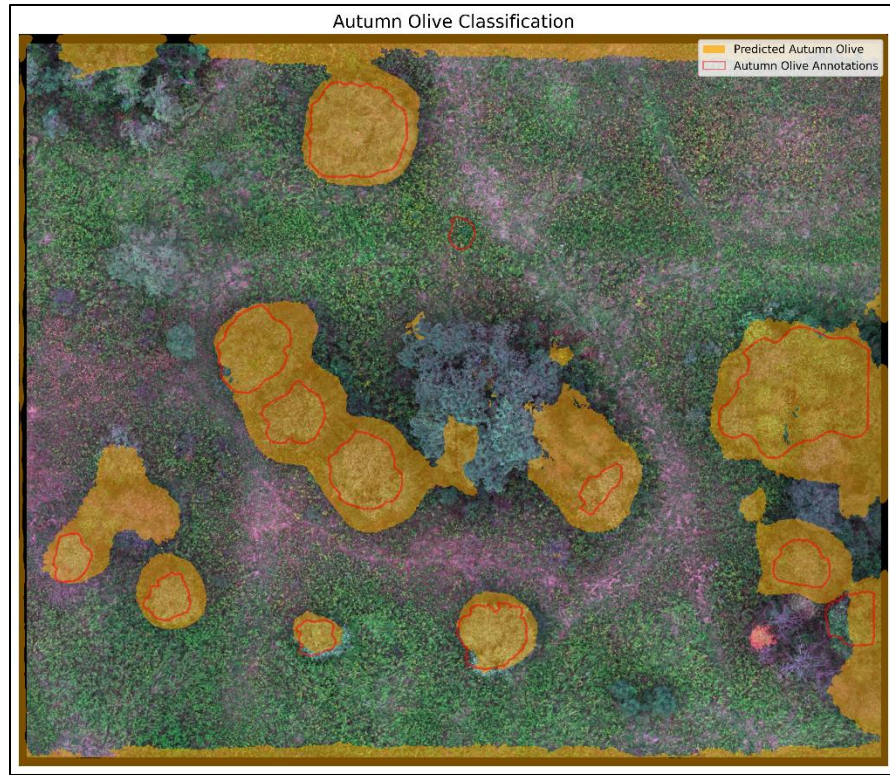


Figure 36: Late-stage Multispec U-Net classification (9/26/2024)

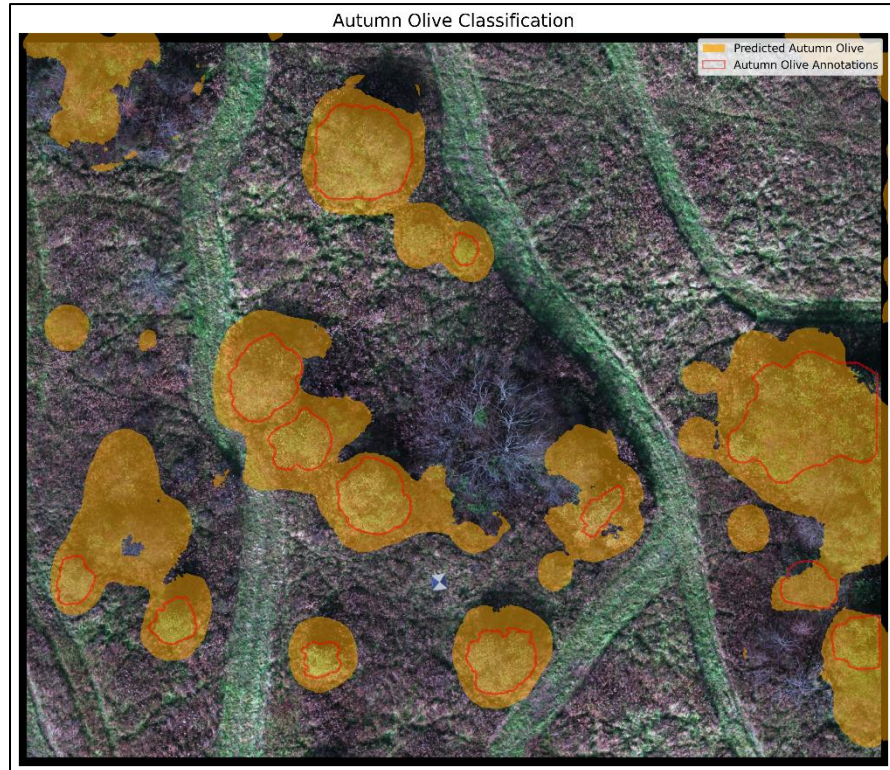


Figure 37: Senescence-stage Multispec U-Net classification (11/8/2023)

### *VI-Comp U-Net Classification*

The Vegetation Index Composite U-Net (VI-Comp U-Net) model combined the 5-band multispectral data with three selected stage-specific vegetation indices, chosen based on the feature importance analysis from the Random Forest classification. This integration of spectral bands with vegetation indices was designed to enhance the model's sensitivity to the autumn olive spectral characteristics across different phenological stages.

For the early phenological stage, the model achieved 95.6% overall accuracy with autumn olive detection metrics showing 80.4% precision and 95.1% recall, resulting in an F1-score of 0.871 (Table 14). There are significant commission errors, particularly with 1,665,399 pixels from the other tree class being incorrectly classified as autumn olive. Despite these commission errors, the high recall value of 95.1% indicates strong detection capability for true autumn olive instances. The early-stage model showed somewhat inconsistent learning progression, though convergence did occur rapidly and eventually stabilized at epoch 74.

Peak-stage classification reached the highest performance levels with a 96.3% overall accuracy and autumn olive F1-score of 0.922 (Table 15). The confusion matrix indicates that 17,878,855 of 18,727,724 autumn olive pixels (95.5%) were correctly classified, demonstrating excellent detection. However, 1,112,773 low vegetation pixels and 1,064,075 other tree pixels were misidentified as autumn olive, suggesting continued challenges in discriminating between autumn olive and other vegetation types during peak foliage development.

The late phenological stage saw the VI-Comp model achieve 95.7% overall accuracy with autumn olive detection showing 86.8% precision and 92.3% recall (F1-score: 0.894) (Table 16). There are 9,869,197 correctly classified autumn olive pixels against 493,784 autumn olive pixels misidentified as other trees. Notably, commission errors decreased compared to earlier stages, with

920,258 other tree pixels incorrectly classified as autumn olive. The late-stage model converged relatively quickly compared to the peak stage, with optimal performance reached at epoch 72 and rapid initial improvements followed by consistent refinement.

During senescence, autumn olive detection became considerably more challenging as reflected in the decreased precision (69.7%) despite maintaining high recall (91.7%), yielding the lowest F1-score across all stages (0.792) (Table 17). While overall accuracy remained respectable at 92.6%, there is substantial confusion with other classes, particularly 2,404,880 other tree pixels misclassified as autumn olive. This increase in commission errors likely stems from autumn olive's extended leaf retention creating similar spectral patterns to partially senescent vegetation of other species. Interestingly, the senescence model reached its peak performance after just 20 epochs, showing an extremely rapid convergence compared to other stages. This quick training saturation suggests that the distinctive features of autumn olive during senescence, while creating more classification errors, are more immediately apparent to the model.

The learning trajectories varied across phenological stages. The early-stage model showed rapid, though unstable, convergence with the validation loss fluctuating drastically before stabilizing (Fig. 38). The peak stage demonstrated the most gradual and consistent improvement pattern, with steady progress across nearly 200 epochs (Fig. 39). The late stage converged more rapidly yet still showed meaningful improvements until epoch 72 (Fig. 40). The senescence stage model exhibited the most dramatic learning pattern, with extremely rapid convergence within the first 20 epochs followed by performance degradation with additional training (Fig. 41).

Examination of the classification maps reveals distinct patterns across the four phenological stages. The early-stage (Fig. 42) shows autumn olive patches with solid definition against the dormant background vegetation, with the model showing strong detection of known

patches. The peak-stage classification (Fig. 43) shows similar detection patterns with identification of autumn olive against developed vegetation. During late-stage (Fig. 44), the model maintains reliable detection of autumn olive patches as surrounding vegetation begins transitioning to early senescence. The senescence-stage classification (Fig. 45) demonstrates how autumn olive remains detectable even against a complex background of senescent vegetation, though with increased classification noise particularly evident in areas where vegetation patterns create similar spectral signatures to autumn olive's retained foliage.

Early-Stage VI-Comp U-Net Confusion Matrix		Reference Data					
		AutumnOlive	Barren	LowVeg	OtherTree	Totals	User's Accuracy
Classified Data	AutumnOlive	10245596	0	836368	1665399	12747363	80.4%
	Barren	588	3028710	8961	121216	3159475	95.9%
	LowVeg	222502	36	60086122	437460	60746120	98.9%
	OtherTree	304068	3837	475325	16125858	16909088	95.4%
	Totals	10772754	3032583	61406776	18349933		
	Producer's Accuracy	95.1%	99.9%	97.8%	87.9%		

#### Early-Stage VI-Comp U-Net Performance

Class	Precision	Recall	F1-Score	Model Accuracy
AutumnOlive	0.804	0.951	0.871	95.6%
Barren	0.959	0.999	0.978	
LowVeg	0.989	0.978	0.984	
OtherTree	0.954	0.879	0.915	
Weighted Average	0.960	0.956	0.957	

Table 14: Early-stage VI-Comp U-Net confusion matrix (top); Early-stage VI-Comp U-Net performance metrics (bottom)

Peak-Stage VI-Comp U-Net Confusion Matrix		Reference Data					
		AutumnOlive	Barren	LowVeg	OtherTree	Totals	User's Accuracy
Classified Data	AutumnOlive	17878855	0	1112773	1064075	20055703	89.1%
	Barren	499	2302643	75099	19336	2397577	96.0%
	LowVeg	454609	55104	128472190	1591719	130573622	98.4%
	OtherTree	393761	10313	2470977	40291457	43166508	93.3%
	Totals	18727724	2368060	132131039	42966587		
	Producer's Accuracy	95.5%	97.2%	97.2%	93.8%		

#### Peak-Stage VI-Comp U-Net Performance

Class	Precision	Recall	F1-Score	Model Accuracy
AutumnOlive	0.891	0.955	0.922	96.3%
Barren	0.960	0.972	0.966	
LowVeg	0.984	0.972	0.978	
OtherTree	0.933	0.938	0.936	
Weighted Average	0.964	0.963	0.963	

Table 15: Peak-stage VI-Comp U-Net confusion matrix (top); Peak-stage VI-Comp U-Net performance metrics (bottom)

Late-Stage VI-Comp U-Net Confusion Matrix		Reference Data					
		AutumnOlive	Barren	LowVeg	OtherTree	Totals	User's Accuracy
Classified Data	AutumnOlive	9869197	2802	583075	920258	11375332	86.8%
	Barren	422	1706085	25348	11124	1742979	97.9%
	LowVeg	333968	23668	64936467	895120	66189223	98.1%
	OtherTree	493784	6915	1002887	19400465	20904051	92.8%
	Totals	10697371	1739470	66547777	21226967		
	Producer's Accuracy	92.3%	98.1%	97.6%	91.4%		

#### Late-Stage VI-Comp U-Net Performance

Class	Precision	Recall	F1-Score	Model Accuracy
AutumnOlive	0.868	0.923	0.894	95.7%
Barren	0.979	0.981	0.980	
LowVeg	0.981	0.976	0.978	
OtherTree	0.928	0.914	0.921	
Weighted Average	0.958	0.957	0.957	

Table 16: Late-stage VI-Comp U-Net confusion matrix (top); Late-stage VI-Comp U-Net performance metrics (bottom)

Senescence-Stage VI-Comp U-Net Confusion Matrix		Reference Data					
		AutumnOlive	Barren	LowVeg	OtherTree	Totals	User's Accuracy
Classified Data	AutumnOlive	8806205	288	1421634	2404880	12633007	69.7%
	Barren	416	1074531	2681	17287	1094915	98.1%
	LowVeg	253429	6434	61953042	1019332	63232237	98.0%
	OtherTree	542274	4579	1469241	18072307	20088401	90.0%
	Totals	9602324	1085832	64846598	21513806		
	Producer's Accuracy	91.7%	99.0%	95.5%	84.0%		

#### Senescence-Stage VI-Comp U-Net Performance

Class	Precision	Recall	F1-Score	Model Accuracy
AutumnOlive	0.697	0.917	0.792	92.6%
Barren	0.981	0.990	0.985	
LowVeg	0.980	0.955	0.967	
OtherTree	0.900	0.840	0.869	
Weighted Average	0.934	0.926	0.928	

Table 17: Senescence-stage VI-Comp U-Net confusion matrix (top); Senescence-stage VI-Comp U-Net performance metrics (bottom)

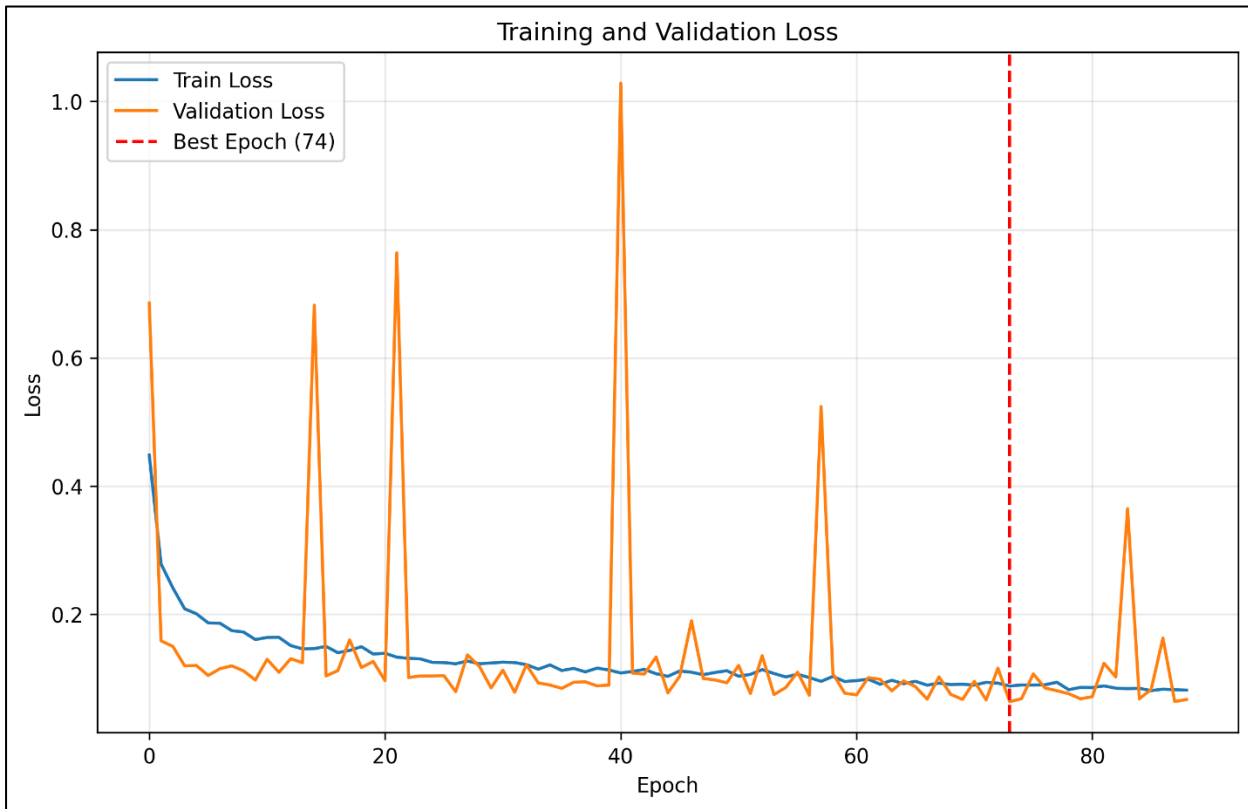


Figure 38: Early-stage VI-Comp U-Net loss

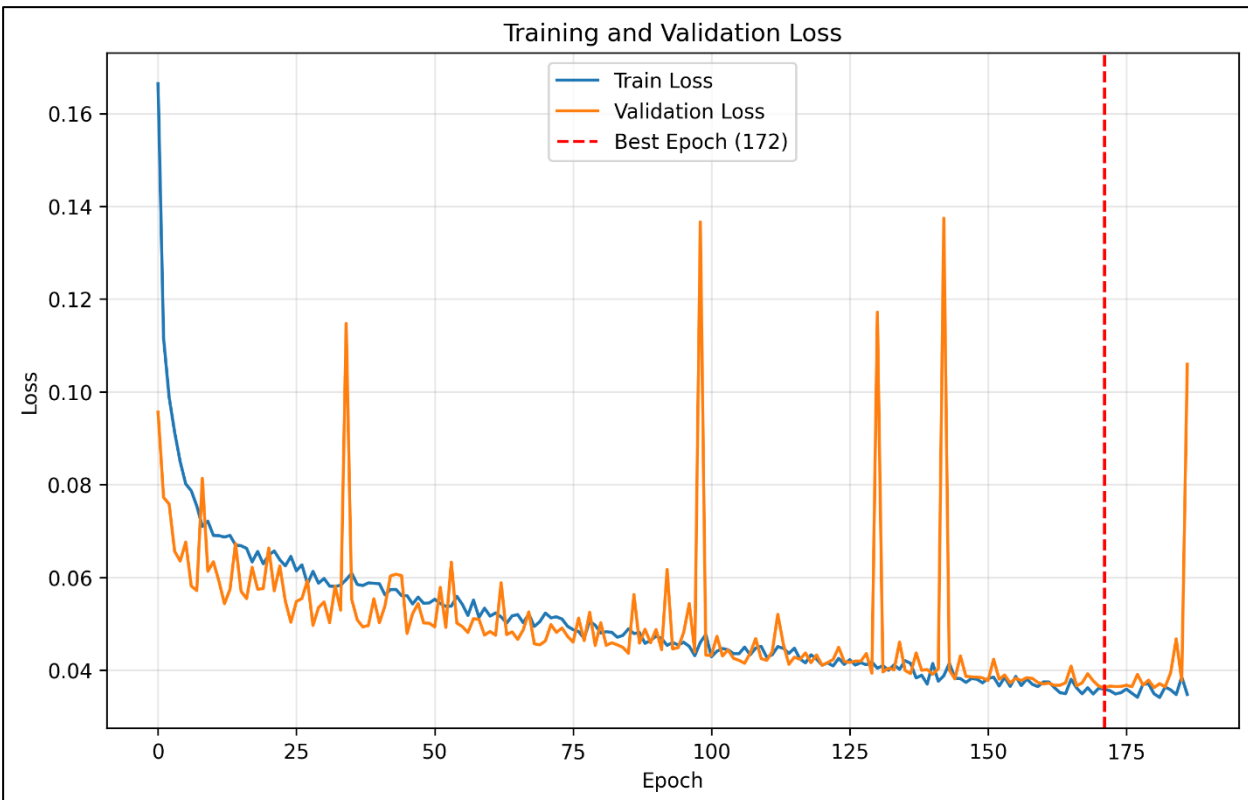


Figure 39: Peak-stage VI-Comp U-Net loss

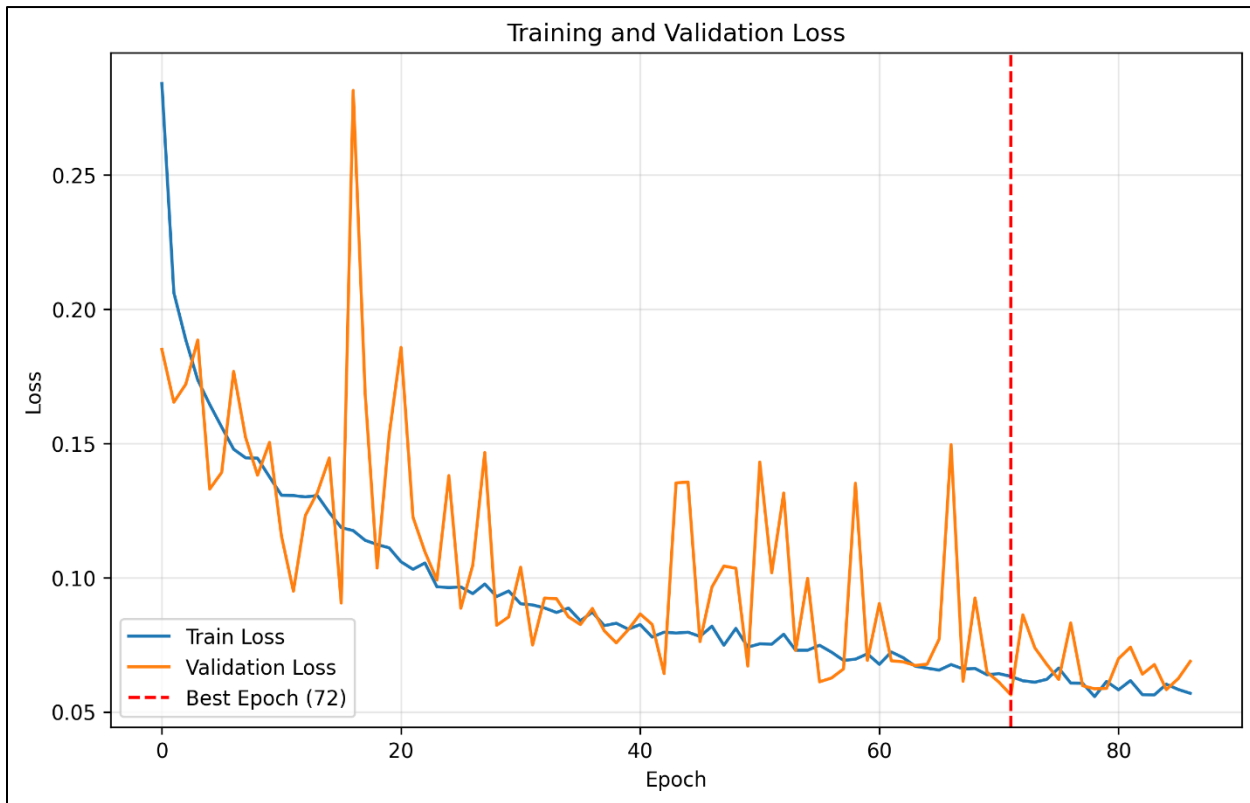


Figure 40: Late-stage VI-Comp U-Net loss

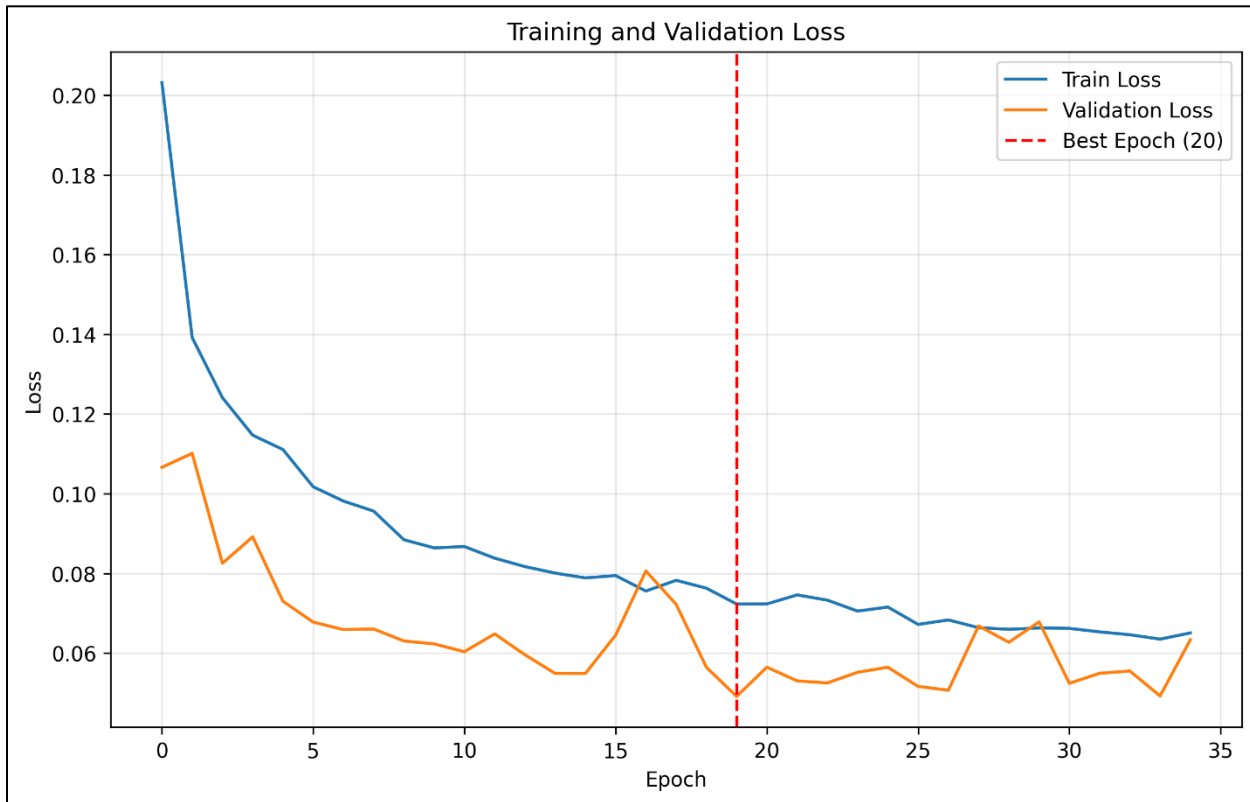


Figure 41: Senescence-stage VI-Comp U-Net loss

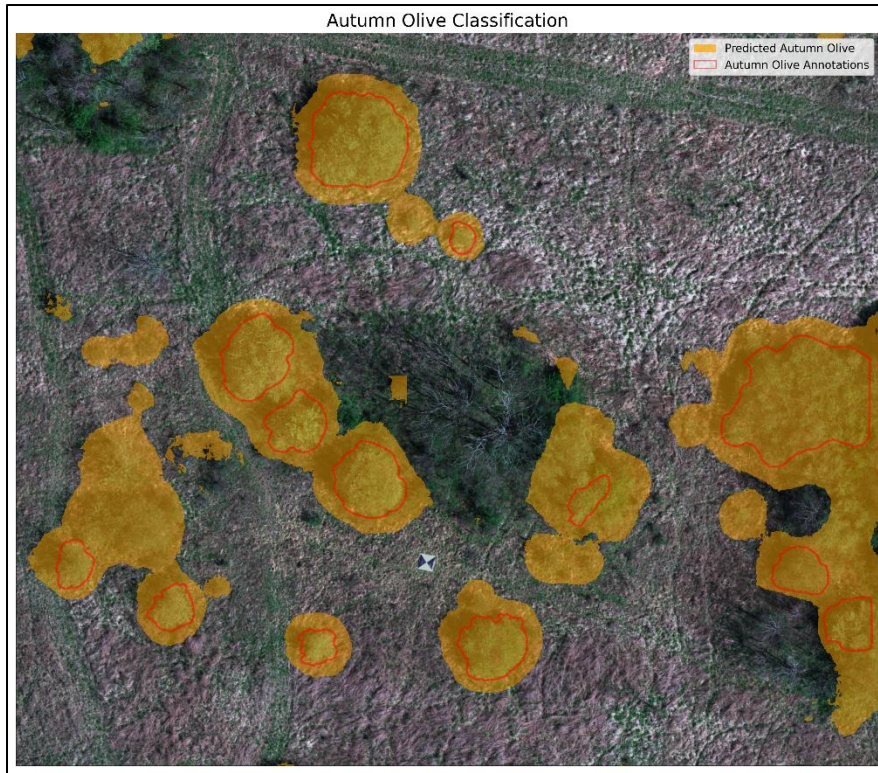


Figure 42: Early-stage VI-Comp U-Net classification (4/13/2023)



Figure 43: Peak-stage VI-Comp U-Net classification (7/19/2023)

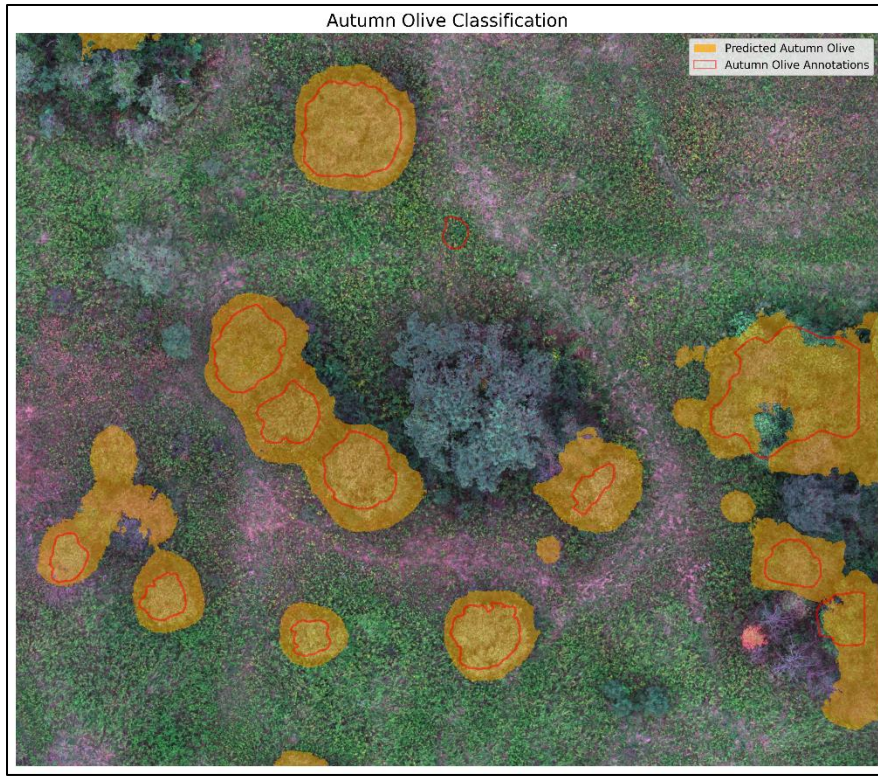


Figure 44: Late-stage VI-Comp U-Net classification (9/26/2024)



Figure 45: Senescence-stage VI-Comp U-Net classification (11/8/2023)

### *RGB U-Net Classification*

The RGB U-Net model uses standard 3-band imagery as input, representing a configuration that would be available from most commercial UAS platforms without specialized multispectral sensors. This approach was implemented to evaluate whether autumn olive could be effectively detected using non-calibrated digital numbers, which would significantly reduce equipment costs and complexity for land managers. Similar to the Multispec U-Net model, training convergence varied across the phenological stages. The early stage improved to the 50<sup>th</sup> epoch, peak stage improved until the 189<sup>th</sup> epoch and recorded the most stable training cycle of any model, late stage improved until the 167<sup>th</sup> epoch, and the senescence stage improved until the 78<sup>th</sup> epoch.

Performance across phenological stages demonstrated notable variations in autumn olive detection capabilities. During the early stage, the RGB U-Net achieved an overall accuracy of 95.5% with a weighted F1-score of 0.956 (Table 18). For the autumn olive class specifically, the model demonstrated 86.8% precision and 91.8% recall, resulting in an F1-score of 0.893. A total of 2,566,102 autumn olive pixels were incorrectly classified as other trees, while 4,140,874 other tree pixels were misclassified as autumn olive. This pattern of confusion between woody vegetation types was consistent with findings from the multispectral model, suggesting that differentiating between similar canopy structures remains challenging when using RGB images as well.

The peak phenological stage marked the highest performance for the RGB model, with an overall accuracy of 96.7% and an autumn olive F1-score of 0.927 (Table 19). During this stage, producer's accuracy for autumn olive reached 97.7%, indicating that the model successfully identified the vast majority of autumn olive pixels in the validation dataset. However, the user's accuracy decreased to 88.2% due to increased commission errors, particularly with 4,290,604 other

tree pixels misclassified as autumn olive. This suggests that at peak foliage development, the RGB model becomes more biased towards classifying woody vegetation as autumn olive, potentially due to subtle color differences that become more pronounced during full leaf expansion.

Performance remained strong during the late phenological stage, with an overall accuracy of 96.4% and an autumn olive F1-score of 0.912 (Table 20). The confusion matrix showed that misclassification between autumn olive and other trees decreased compared to the peak stage, with 478,666 autumn olive pixels incorrectly classified as other trees and 2,281,080 other tree pixels misclassified as autumn olive. While the Multispec model saw dissimilar results, the simpler form of information provided through the RGB images may have improved discrimination. Additionally, an increase in recall when compared to the late stage of the multispec model may point towards some level of overfitting, which is supported by the increased training duration.

The senescence stage showed the weakest performance for autumn olive detection using RGB imagery, with precision dropping to 79.9% while recall remained high at 95.8%. The resulting F1-score of 0.871, which is a decrease from other phenological stages (Table 21). Examination of the confusion matrix revealed substantial commission errors, with 5,324,684 other tree pixels incorrectly classified as autumn olive. This increased confusion during senescence likely stems from the complex spectral patterns that emerge when different species begin senescence at varying rates, creating a more heterogeneous landscape that is difficult to classify using only RGB imagery.

Learning curves for the RGB U-Net models showed efficient convergence (Figs. 46-49), with the early-stage model requiring 50 epochs to reach optimal performance, while peak, late, and senescence models stabilized after 189, 167, and 78 epochs, respectively. The peak stage model demonstrated the most stable and prolonged improvement during training, suggesting that

the RGB features at this phenological stage provided the most consistent information for the model to learn from.

The non-woody vegetation classes (Barren and LowVeg) maintained high classification accuracy (>92% F1-scores) across all phenological stages, indicating that RGB information is sufficient for distinguishing between woody vegetation, non-woody vegetation, and other land cover classes.

RGB U-Net classification maps reveal clear seasonal variations in autumn olive detection performance. The early-stage map (Fig. 50) shows good detection of autumn olive patches against the dormant brown low vegetation and minimal foliage of other tree species. Peak stage classification (Fig. 51) demonstrates the strongest performance, with excellent delineation of autumn olive against the similarly green landscape and more precise boundary alignment. The late-stage map (Fig. 52) maintains generally accurate detection with some inconsistencies as the background vegetation begins to have spectral divergence. The senescence stage map (Fig. 53) exhibits the most challenging detection conditions, with accurate identification of core autumn olive areas but less precise boundary definition and more scattered commission errors throughout the landscape, reflecting the complex seasonal changes of vegetation in various senescence stages.

Early-Stage RGB U-Net Confusion Matrix		Reference Data					
		AutumnOlive	Barren	LowVeg	OtherTree	Totals	User's Accuracy
Classified Data	AutumnOlive	40545805	46260	1962119	4140874	46695058	86.8%
	Barren	58338	12689582	380834	630455	13759209	92.2%
	LowVeg	993572	89356	240069115	2297622	243449665	98.6%
	OtherTree	2566102	40431	3743210	69702003	76051746	91.7%
	Totals	44163817	12865629	246155278	76770954		
	Producer's Accuracy	91.8%	98.6%	97.5%	90.8%		

#### Early-Stage RGB U-Net Performance

Class	Precision	Recall	F1-Score	Model Accuracy
AutumnOlive	0.868	0.918	0.893	95.5%
Barren	0.922	0.986	0.953	
LowVeg	0.986	0.975	0.981	
OtherTree	0.917	0.908	0.912	
Weighted Average	0.956	0.955	0.956	

Table 18: Early-stage RGB U-Net confusion matrix (top); Early-stage RGB U-Net performance metrics (bottom)

Peak-Stage RGB U-Net Confusion Matrix		Reference Data					
		AutumnOlive	Barren	LowVeg	OtherTree	Totals	User's Accuracy
Classified Data	AutumnOlive	75990383	43284	5875201	4290604	86199472	88.2%
	Barren	114469	12560116	882996	104100	13661681	91.9%
	LowVeg	789948	259970	510367283	4353221	515770422	99.0%
	OtherTree	917438	19818	8872415	167288704	177098375	94.5%
	Totals	77812238	12883188	525997895	176036629		
	Producer's Accuracy	97.7%	97.5%	97.0%	95.0%		

#### Peak-Stage RGB U-Net Performance

Class	Precision	Recall	F1-Score	Model Accuracy
AutumnOlive	0.882	0.977	0.927	96.7%
Barren	0.919	0.975	0.946	
LowVeg	0.990	0.970	0.980	
OtherTree	0.945	0.950	0.947	
Weighted Average	0.968	0.967	0.967	

Table 19: Peak-stage RGB U-Net confusion matrix (top); Peak-stage RGB U-Net performance metrics (bottom)

Late-Stage RGB U-Net Confusion Matrix		Reference Data					
		AutumnOlive	Barren	LowVeg	OtherTree	Totals	User's Accuracy
Classified Data	AutumnOlive	30992836	34866	2726469	2281080	36035251	86.0%
	Barren	30562	5306420	551719	66320	5955021	89.1%
	LowVeg	438337	74931	199684090	1659876	201857234	98.9%
	OtherTree	478666	8561	2769645	63561277	66818149	95.1%
	Totals	31940401	5424778	205731923	67568553		
	Producer's Accuracy	97.0%	97.8%	97.1%	94.1%		

#### Late-Stage RGB U-Net Performance

Class	Precision	Recall	F1-Score	Model Accuracy
AutumnOlive	0.860	0.970	0.912	96.4%
Barren	0.891	0.978	0.933	
LowVeg	0.989	0.971	0.980	
OtherTree	0.951	0.941	0.946	
Weighted Average	0.966	0.964	0.965	

Table 20: Late-stage RGB U-Net confusion matrix (top); Late-stage RGB U-Net performance metrics (bottom)

Senescence-Stage RGB U-Net Confusion Matrix		Reference Data					
		AutumnOlive	Barren	LowVeg	OtherTree	Totals	User's Accuracy
Classified Data	AutumnOlive	36779899	25665	3882495	5324684	46012743	79.9%
	Barren	8059	5320724	564920	191902	6085605	87.4%
	LowVeg	592311	70226	256484974	3154275	260301786	98.5%
	OtherTree	1028576	28037	3814898	79796860	84668371	94.2%
	Totals	38408845	5444652	264747287	88467721		
	Producer's Accuracy	95.8%	97.7%	96.9%	90.2%		

#### Senescence-Stage RGB U-Net Performance

Class	Precision	Recall	F1-Score	Model Accuracy
AutumnOlive	0.799	0.958	0.871	95.3%
Barren	0.874	0.977	0.923	
LowVeg	0.985	0.969	0.977	
OtherTree	0.942	0.902	0.922	
Weighted Average	0.956	0.953	0.954	

Table 21: Senescence-stage RGB U-Net confusion matrix (top); Senescence-stage RGB U-Net performance metrics (bottom)

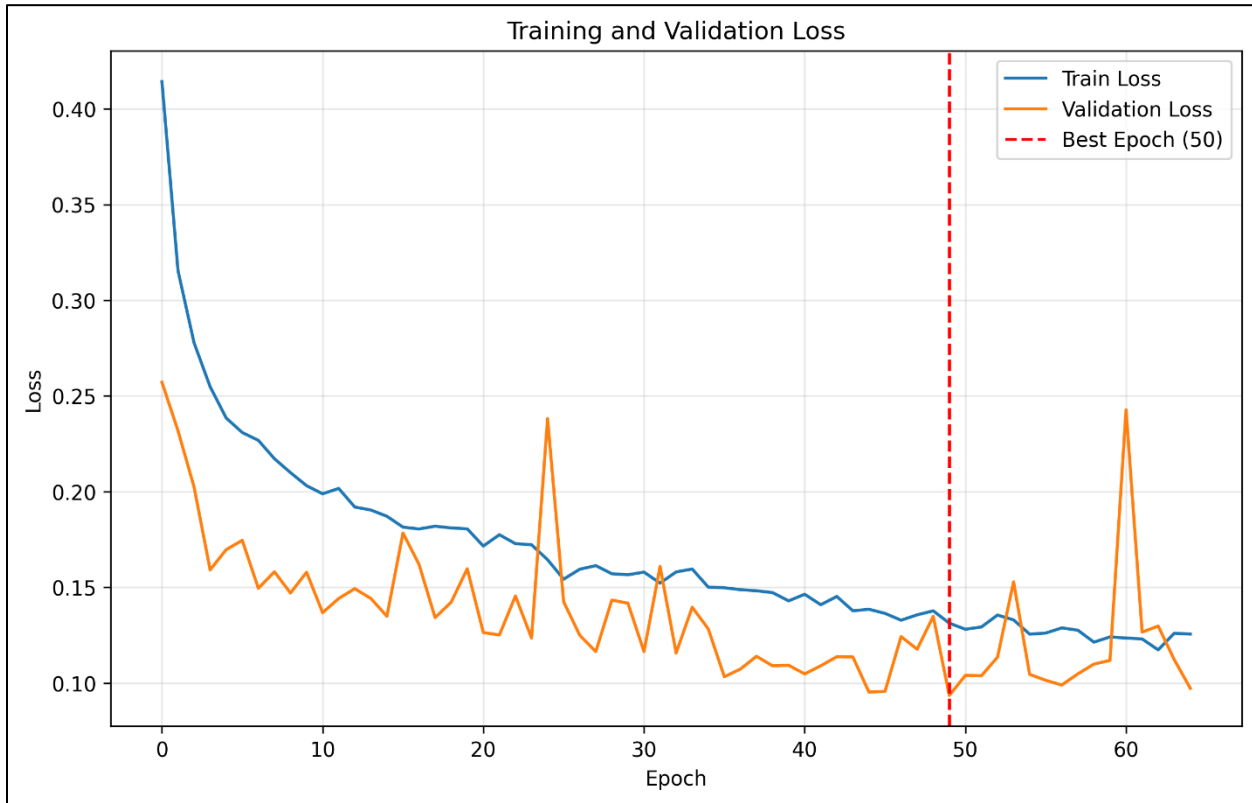


Figure 46: Early-stage RGB U-Net loss

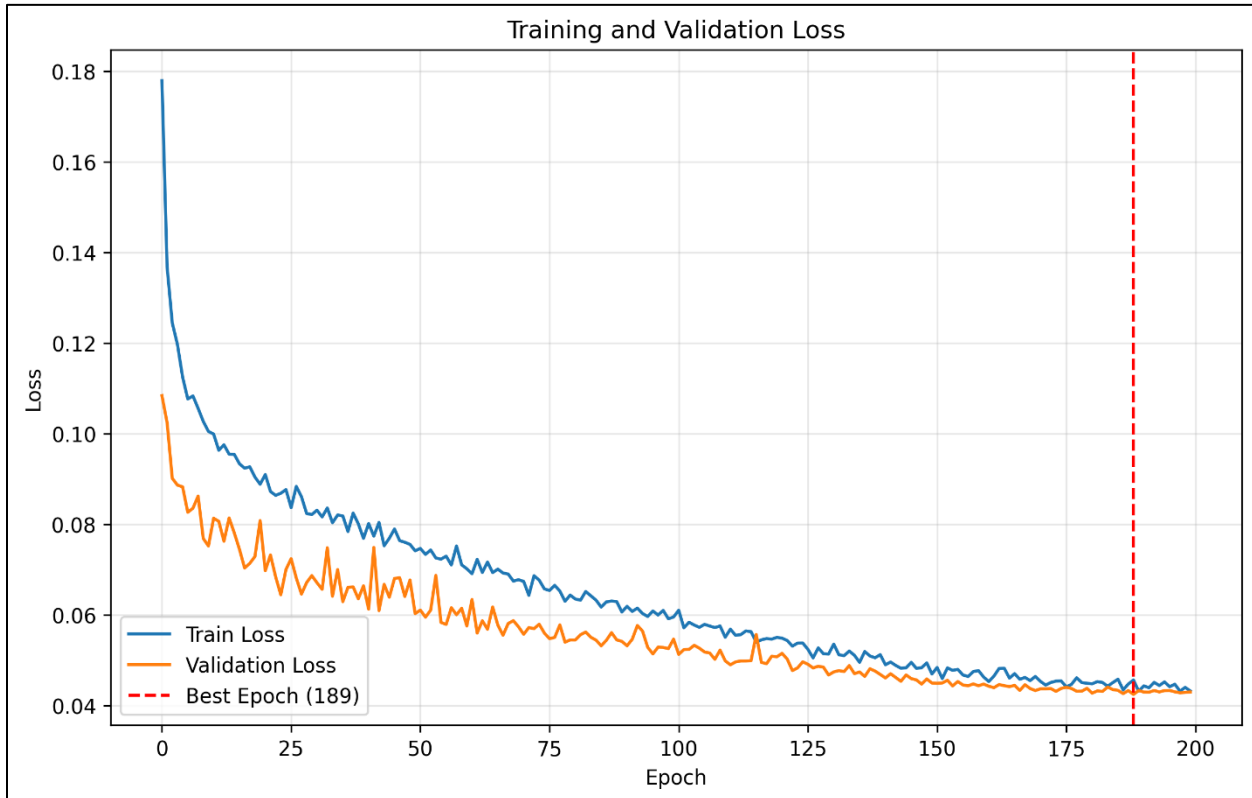


Figure 47: Peak-stage RGB U-Net loss

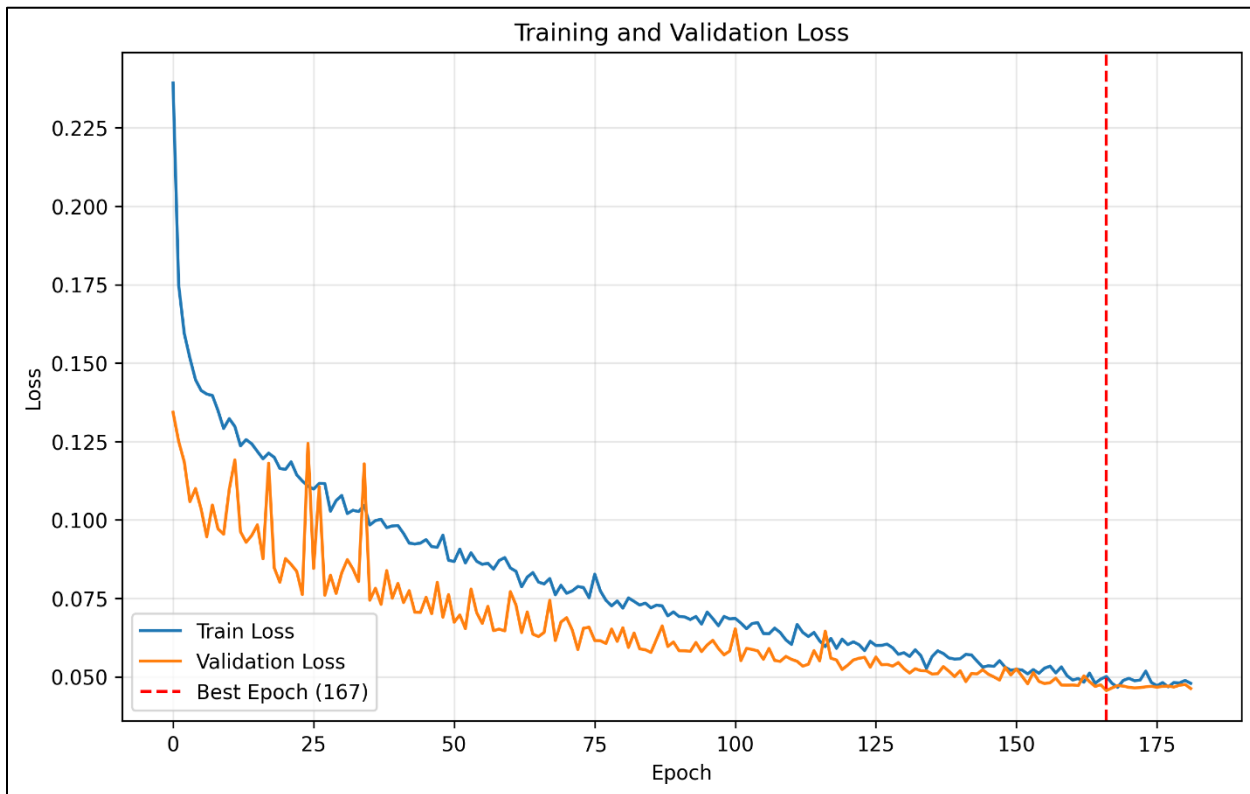


Figure 48: Late-stage RGB U-Net loss

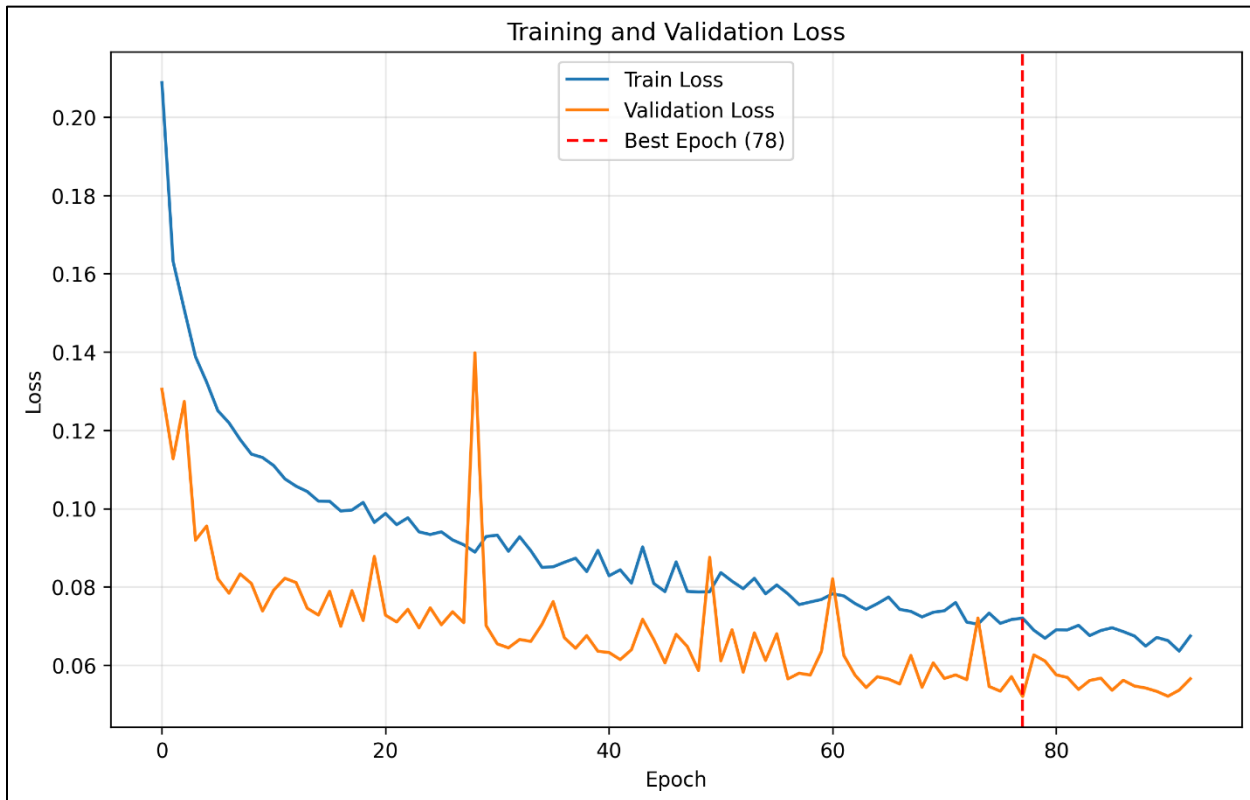


Figure 49: Senescence-stage RGB U-Net loss

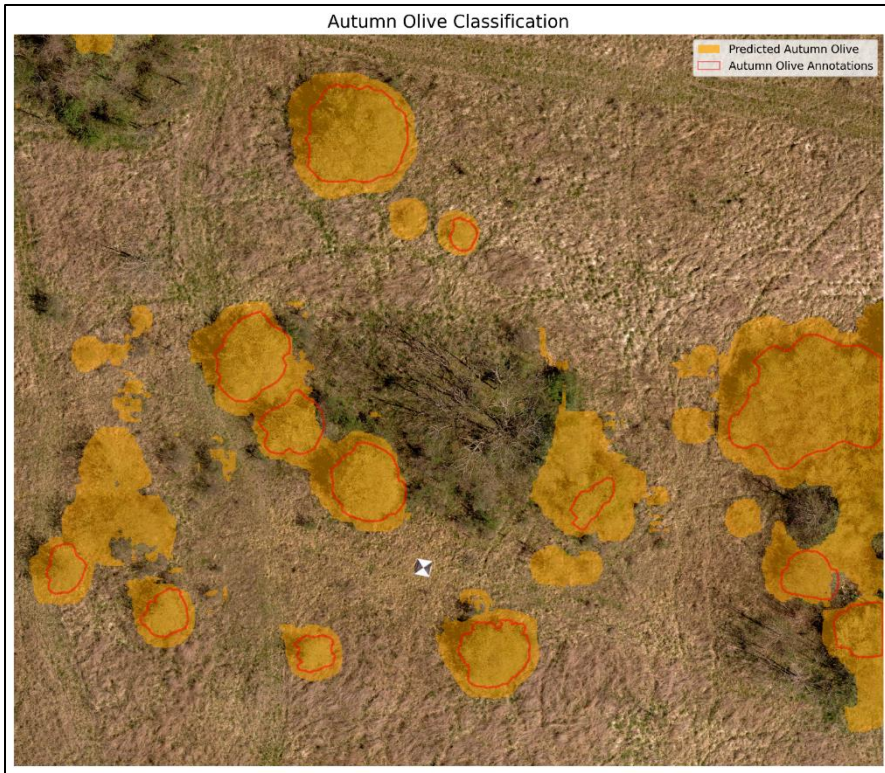


Figure 50: Early-stage RGB U-Net classification (4/13/2023)



Figure 51: Peak-stage RGB U-Net classification (7/19/2023)

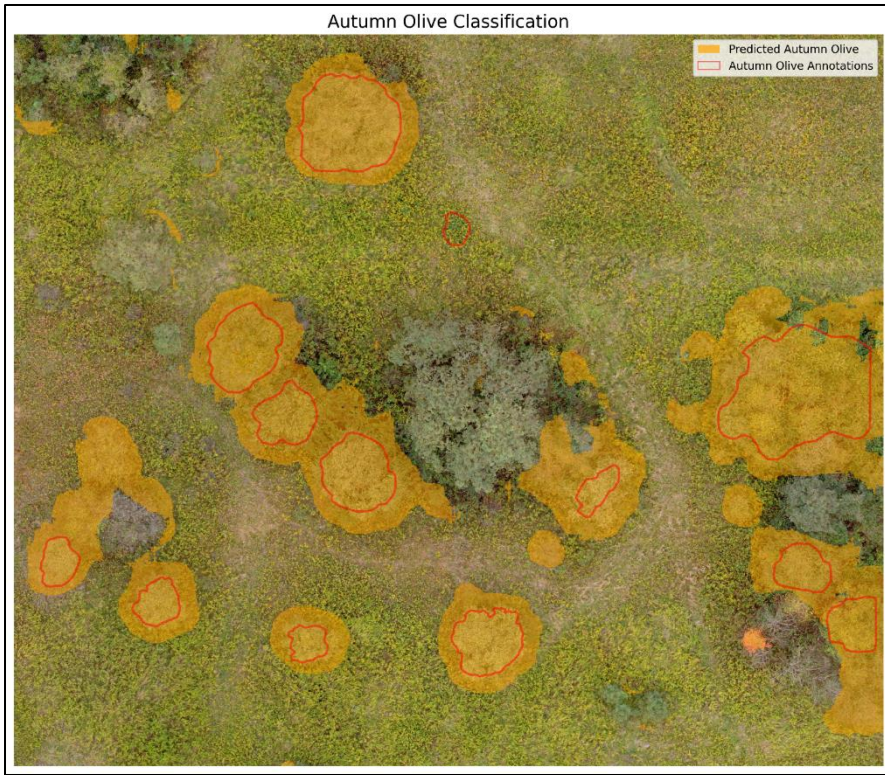


Figure 52: Late-stage RGB U-Net classification (9/26/2024)



Figure 53: Senescence-stage RGB U-Net classification (11/8/2023)

### *U-Net Model Comparison*

The performance evaluation of the Multispectral, VI-Comp, and RGB U-Net models across four phenological stages recorded varied performance levels in their effectiveness for autumn olive detection. Overall accuracy remained consistently high across all models and stages, ranging from 92.0% to 96.9% (Fig. 54). The Multispectral U-Net achieved the highest accuracy during early stage (96.9%), while the RGB U-Net led during peak stage (96.7%). The senescence stage presented the greatest challenge, with the Multispectral U-Net recording the lowest accuracy (92.0%), while RGB models achieved 95.3%.

For autumn olive specifically, F1-scores varied considerably across models and phenological stages (Fig. 55). During early leaf development, the Multispectral U-Net demonstrated the highest performance with an F1-score of 0.911 (87% precision and 95.5% recall), this is compared to the RGB model which achieved an F1-score of 0.893 and the VI-Comp model with 0.871. This advantage is likely from the multispectral data's ability to use the red-edge and NIR bands, and without the confusion that the vegetation indices may introduce during this stage. As vegetation reached peak development, all models achieved their highest seasonal performance. The RGB model led in performance for this stage with an F1-score of 0.927, which was influenced heavily by a recall of 97.7%. The late-stage classification had a shift in model performance. The RGB U-Net recorded the highest F1-score of 0.912 for autumn olive detection, which outperformed both the VI-Comp (0.894) and the Multispectral models (0.844). This result suggests that even without spectral information beyond the visible range, the RGB data was able to capture important visual features that distinguish autumn olive during the beginning of transitional periods. The senescence stage had significant classification challenges across all models, with the RGB model maintaining its stronger F1-score performance (0.871), surpassing both the VI-Comp

(0.792) and Multispectral U-Nets (0.799). All models showed increases in commission errors during this period.

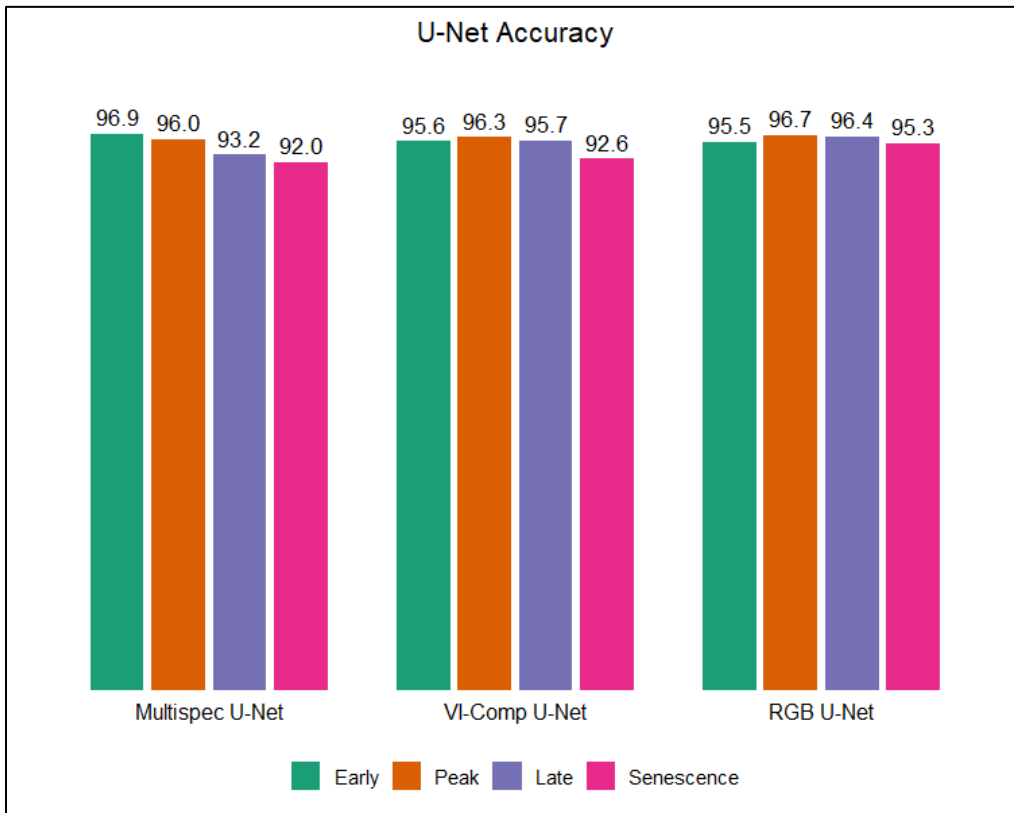


Figure 54: U-Net Model accuracy

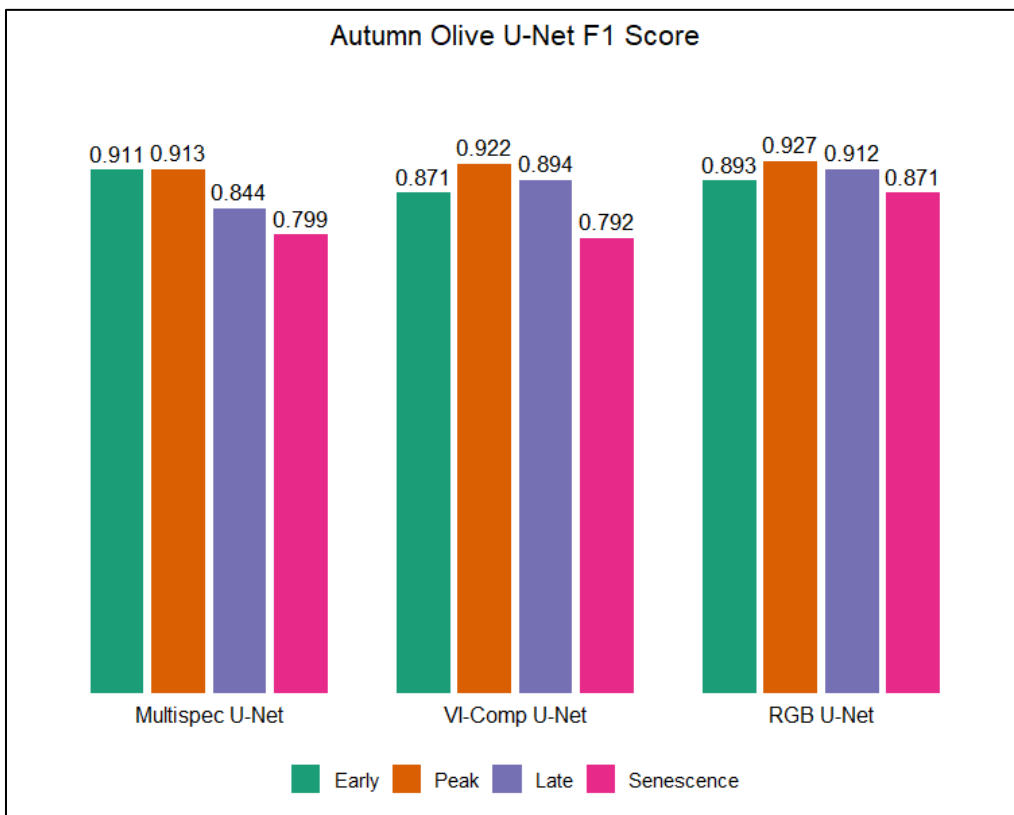


Figure 55: Autumn Olive U-Net F1-score

## **UAAS Treatment**

The UAAS application at the Goshen Road site demonstrated the feasibility and effectiveness of unmanned aerial herbicide treatment for autumn management. Initial calibration using water and blue dye confirmed that application rates of 10 GPA, 12.5 GPA, and 15 GPA provided adequate coverage for targeted canopies (Fig. 56). These preliminary tests were used for determining the range of appropriate spray parameters for the actual herbicide application.

Treatment was conducted on September 11<sup>th</sup>, 2024, with the site divided into three experimental zones corresponding to the different application rates. The UAAS effectively navigated the treatment area using the 3D flight mapping area, though certain limitations were observed. When encountering autumn olive patches with significant height variations, the horizontal obstacle avoidance system would cause the UAAS to interrupt and pause operations when outlying branches were detected. This limitation was observed frequently in densely vegetated areas where canopy heights of non-targeted tree species exceeded the programmed flight altitude of 8.5 feet above targeted canopies.

Post-treatment assessments at 6 days and 15 days showed progressive effectiveness of the herbicide application across all treatment zones. Visual inspection at 6 days post-treatment showed the beginning of chlorosis and wilting of autumn olive foliage, with effects becoming substantially more observable at 15 days following the application. The 15 GPA application rate produced the most rapid effects, though differences between application rates became less distinct at the 15-day assessment.

NDVI analysis derived from the pre- and post-treatment multispectral imagery confirmed reduced photosynthetic activity within the targeted canopies (Fig. 57). The herbicide prescription demonstrated selectivity as intended and minimal impact was observed on adjacent

non-targeted vegetation. Additionally, the propwash effect from the UAAS rotors enhanced the canopy penetration and resulted in a more uniform coverage throughout the outer and inner part of the canopy. This effect was especially noticeable in denser canopies where conventional ground-based application methods may struggle to achieve complete coverage.

No significant drift was observed during application and clear boundaries were maintained between treated autumn olive canopies and neighboring vegetation. These results suggest that UAAS-based herbicide application represents a viable option and more time-effective option for managing autumn olive, particularly in areas with steep terrain and limited accessibility.

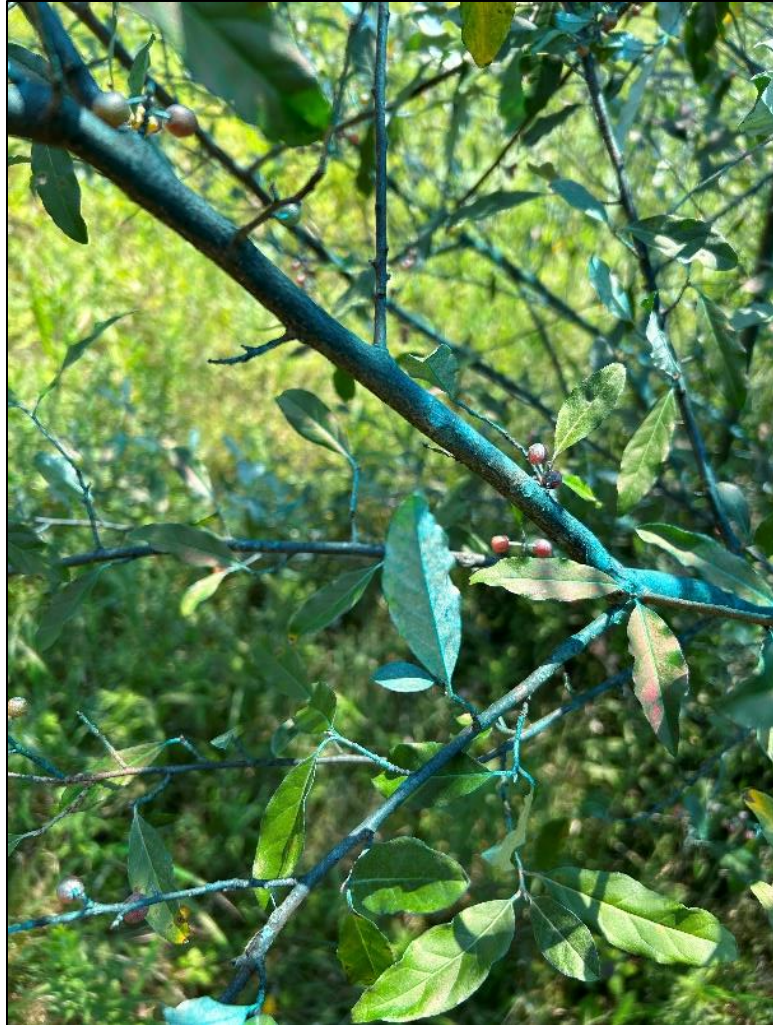


Figure 56: UAAS water and dye treatment (12.5 GPA)

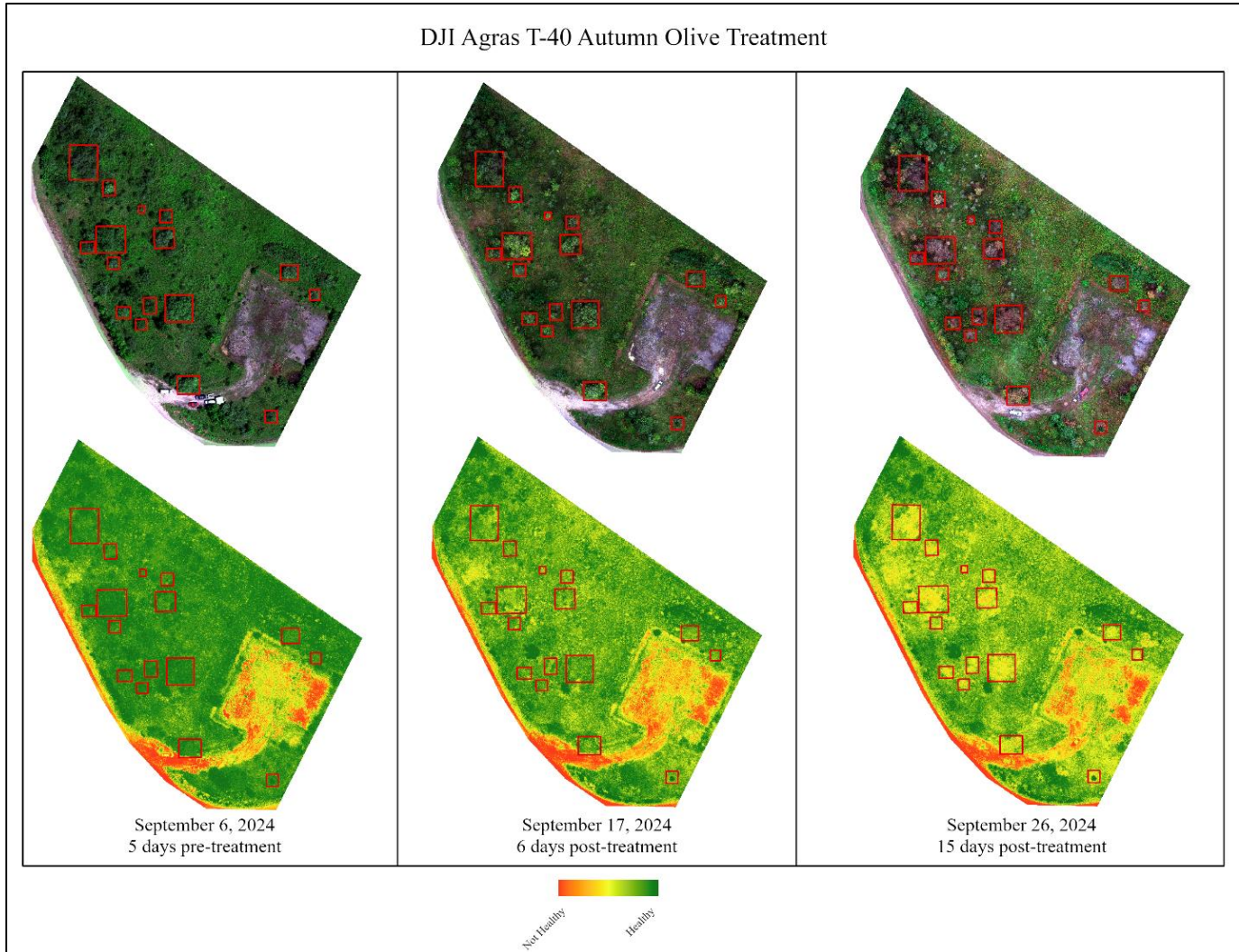


Figure 57: UAAS Goshen Road treatment NDVI (red boxes mark targeted canopies)

## **Discussion**

The integration of UAS technology and machine learning for detecting and managing *Elaeagnus umbellata* represents a novel approach to addressing one of the most persistent challenges in surface mine reclamation. This research evaluated multiple classification algorithms across different phenological stages and demonstrated the feasibility of UAAS herbicide application as a practical and effective management strategy.

One of the most significant findings of this study is the marked variation in detection performance across phenological stages. During peak growing season, all of the classification models tested achieved their highest accuracy for autumn olive detection, with the Random Forest classifier reaching an F1-score of 0.696 and the U-Net models achieving F1-scores of 0.913, 0.922, and 0.927 for the Multispectral, VI-Comp, and RGB models, respectively. This optimal detection window coincides with full canopy development when autumn olive exhibits a distinctive spectral signature with heightened NIR reflectance and a difference in measured index values compared to surrounding vegetation. The late phenological stage also demonstrated strong detection capabilities, particularly with the RGB U-Net model achieving an F1-score of 0.912. This finding corroborates previous research by Oliphant et al. (2016), who noted the extended leaf-on period of the species relative to native deciduous species. Though leaf retention is still maintained for some native species during this time, and senescence is more prominent later in the year, it points towards the subtle changes that may occur during this period that the CNN was able to identify. Our results further quantify this advantage, showing that spectral divergence between autumn olive and native vegetation becomes increasingly pronounced during the late phonological stage. It is also important to note that during this period, senescence may have had an earlier onset than

previous years due to a D4 drought that the state was experiencing (NOAA NRCC, 2024). However, despite these conditions, detection ability remained strong.

Interestingly, the early phenological stage showed varied detection performance (F1-scores ranging from 0.567 for the Random Forest model to 0.911 for the Multispectral U-Net model), despite limited leaf development in most vegetation. This suggests that autumn olive's early leaf emergence, which typically precedes many native species in the Appalachian region (Riffe, 2018), provides another potential detection window with the proper data. This early-season characteristic offers an advantage for EDRR strategies where identification can occur before treatment implementations are prepared.

The senescence stage presented the greatest challenge for autumn olive detection across all classification methods, with substantial commission errors occurring between autumn olive and other tree species. This finding diverges somewhat from the expectation that autumn olive's extended leaf retention, which is still present during this time, would make it more prominent during late autumn. The complexity of the landscape during senescence, with varying degrees of leaf color change and leaf drop among different species, likely created a more heterogenous spectral environment that complicated classification. Franke et al (2018) made similar observations in the challenges of differentiating woody species during transitional phenological periods, attributing this to variable rates of chlorophyll degradation. Additionally, this may also indicate that while the Multispectral and VI-Comp models incorporated NIR data, which strongly reflects chlorophyll production, this may have introduced more noise in the data than meaningful traits that models can learn. The RGB U-Net model for the senescence stage does not include this data and performed significantly higher than the other classifications (F1-score of 0.871 for autumn olive), potentially underlining the effectiveness of simpler data.

The analysis of spectral characteristics and vegetation indices revealed patterns that enhance our understanding of autumn olive's digital reflectance signature. Consistently across phenological stages, autumn olive exhibited higher NIR reflectance compared to other tree species, which aligns with previous findings of the species and other woody invasive species (Huelsman et al., 2023). This heightened NIR response likely results from autumn olive's leaf structure and chlorophyll production. The feature importance methods provided from the Random Forest classification provided valuable insights into which spectral regions and indices contribute most significantly to autumn olive detection. During early and peak phenological stages, combined NIR and red-edge based indices (NDRE, RECI, and LCI) emerged as the most influential predictors. This finding highlights the value of red-edge information for discriminating autumn olive from other vegetation types, particularly when all species are photosynthetically active. Similarly, Amarasingam et al. (2024) found in their study that the inclusion of red-edge and NIR bands and indices is particularly sensitive to the acute changes in reflectance that are observed in exotic species during growing seasons, making these bands and indices incredibly valuable for differing species classification.

During senescence, a significant shift occurred in the index importance measurements, with soil adjusted indices (OSAVI) and visible band indices (GRVI) becoming more valuable for autumn olive detection. This transition reflects the changing spectral dynamics as surrounding vegetation foliage becomes increasingly sparse. The increased importance of soil adjusted indices during this period suggests that background soil reflectance becomes a more significant factor as the overall landscape loses vegetative cover. The inconsistent importance of more commonly used indices like NDVI across phenological stages deserves special attention. Despite its widespread application in vegetation studies, NDVI showed that it provided negative or minimal importance

to the classification during the permutation importance analysis and had a reduced impact on the SHAP importance analysis as well. This finding cautions against the uninformed application of standard vegetation indices for species-specific classification tasks and emphasizes the need for thoughtful index selection based on species characteristics and seasonal context.

The comparison between Random Forest and U-Net classification approaches revealed significant differences in performance and practical applications. The Random Forest classifier, while achieving moderate autumn olive detection accuracy (F1-score of 0.696 during peak stage), provided more meaningful insights through its interpretability and subsequent feature importance analyses. The algorithm's ability to quantify the contribution of different spectral bands and vegetation indices to classification decisions offers practical guidance for sensor selection and data processing in monitoring systems. In contrast, the U-Net models demonstrated substantially higher classification accuracy across all phenological stages, with the F1-scores of autumn olive ranging from 0.792 to 0.927 depending on the model variant and season. This superior performance aligns with findings from other studies that compared the traditional machine learning methods with deep learning approaches for vegetation mapping using high-resolution imagery (Maxwell et al., 2018; Kislov et al., 2021; Amarasingam et al., 2024). The U-Net architecture's ability to learn hierarchical spatial features directly from the imagery, rather than relying on predefined spectral features, likely accounts for much of this performance advantage. However, deep learning methods generally require significant more data in order to be effective and generalize, meaning not to overfit to the training dataset (Pichler and Hartig, 2023). Additionally, while explainable feature analyses like permutation importance and SHAP can be performed on deep learning classifications, the computational requirements for repeated training cycles can be extremely demanding and time consuming (Onishi and Ise, 2021). The advantage that Random Forest

maintains over deep learning architectures like the U-Net is that it is a relatively lightweight algorithm that can be performed repeatedly in a short amount of time without advanced computational resources.

Perhaps the most surprising result was the performance of the RGB U-Net model, which achieved the highest F1-scores for autumn olive during the peak, late, and senescence stages despite utilizing only visible, non-calibrated information. This finding challenges the conventional assumption that multispectral data, particularly the NIR and red-edge regions, is necessary for effective species-level classification. For autumn olive specifically, the distinctive texture caused by the alternating, oval, and wavy leaf structure, and noticeable color differences on either side of the leaves appear to provide sufficient information for accurate detection using standard RGB imagery when implemented with deep learning methods. The resolution of the RGB imagery was 1.5 cm, compared to the 3 cm multispectral imagery, which also underlines the importance of such imagery and its ability to capture these vegetative features. The result of the RGB model does not only provide a efficiency advantage, as the RGB imagery does not need to be calibrated or radiometrically corrected, but a cost savings advantage too. Whereas a multispectral sensor may cost several thousands or tens of thousands of dollars, a standard RGB sensor is much more affordable and available to researchers and land managers. However, it is important to note that the RGB model's performance advantage was not consistent across all stages and metrics. During the early phenological stage, the Multispectral U-Net achieved the highest F1-score (0.911) for autumn olive detection, suggesting that individual bands like the NIR and red-edge regions still remain valuable during periods of limited leaf development and when visible differences between species are less pronounced. Additionally, the RGB model exhibited increased false positives in

some scenarios, which could lead to inefficient allocation of management resources if implemented without verification.

The VI-Composite U-Net model, which integrated the selected vegetation indices with multispectral bands, showed variable performance across phenological stages. While it outperformed the Multispectral model during the peak and late stages, it did not surpass the RGB model in autumn olive detection. Though the VI-Comp model did perform marginally better than RGB on overall accuracy for the early stage. This suggests that pre-calculated vegetation indices, while appealing for their potential to highlight specific vegetation characteristics, may not provide substantial additional value when implemented within the U-Net architecture.

Analysis of the classification maps shows dependable patterns, with particular reliability in the peak phenological stages. The models consistently identified and segmented known autumn olive locations; however, classification boundaries often extended beyond the actual canopy edges into adjacent low vegetation areas. The “buffered effect” on the classifications are possibly a result of two factors: training annotations created through manual digitization rather than a semi or fully unsupervised method such as an object-based or crown-based algorithm, introducing some boundary imprecision; and model generalization that was potentially exacerbated by the progressive dropout layers, which may have limited the model’s ability to learn precise canopy boundary features. Despite the tendency of over-prediction, the models successfully highlighted all known autumn olive studies within the image.

When examining the classification maps, which featured red boundaries of the known autumn olive canopies, several important considerations appeared. While other remote sensing studies often incorporate a separate test dataset in addition to the training and validation dataset, due to the complex pixel mixing between autumn olive and native tree species at very high

resolutions complicates exhaustive labeling. A test dataset without comprehensive autumn olive annotations would likely bias accuracy assessments towards commission errors of the background classes. Interestingly, the classifications frequently identified small autumn olive canopies that were not included in the training data due to limited visibility and size. This detection of unlabeled but verified autumn olive instances suggests that the models developed effective generalization capabilities despite boundary imprecision, capturing the essential spectral and textural signatures of autumn olive.

Another model classification challenge occurred in areas of partial canopy senescence, where autumn olive individuals exhibited variable leaf retention and color change even within the same stand. This intra-species variability, likely resulting from micro-environmental differences in soil moisture, available nutrients, or light availability, created complex spectral patterns that complicated consistent detection.

The evaluation of the UAS-based herbicide application for autumn olive management demonstrated both the potential and limitations of this novel approach. The UAAS effectively delivered targeted herbicide treatment to identified autumn olive patches, with post-treatment assessments confirming gradual effectiveness across all application rates. The selective nature of the treatment, with minimal impact observed on adjacent non-targeted vegetation, highlights a key advantage of this approach over broader broadcast applications. The UAAS demonstrated several operational advantages compared to traditional ground-based treatment methods. The ability to treat autumn olive in steep terrain and difficult-to-access locations represents a significant benefit for managing invasive species on reclaimed mine lands, which often feature challenging topography. Additionally, the downwash effect from the UAAS rotors enhanced canopy penetration, resulting in more uniform coverage throughout the canopy structure. This effect was

particularly valuable for treating dense autumn olive thickets where ground-based sprayers might struggle to achieve complete coverage. As noted by Takekawa et al. (2023), while this provides an advantage for many scenarios, the operator must take extra care when selecting the GPA and atomization of the treatment in order to avoid the effects of drift on non-targeted species. This also demands that applications take notice of ground wind speed as the drift effect can be aggravated by this and the propwash. Furthermore, these sights can be densely vegetated, which causes difficulty for navigation by treatment crews and can pose a greater disturbance to the local environments. This method avoids these issues almost entirely, with UAASs generally able to navigate through a landscape and over canopies successfully with little interference from the pilot. The application rate testing revealed that while the 15 GPA rate produced the most rapid visible effects, differences between application rates became less distinct at the 15-day assessment. This finding suggests that lower application rates may achieve comparable long-term control while reducing chemical usage and adverse environmental impacts. Further research is needed to determine the optimal application parameters for different invasion densities and environmental conditions, as noted by Byrd et al. (2012) and Meesaragandla et al. (2024) in their reviews of approaches to invasive species management.

The integration of detection and treatment capabilities, while not fully implemented in this study, demonstrates the potential for a comprehensive technological approach to invasive species management. The workflow from UAS-based detection to UAAS-based treatment represents a significant advancement toward more efficient and effective management strategies for reclaimed surface mines. This integrated approach aligns with the Early Detection and Rapid Response framework outlined by Reaser et al. (2019) and satisfies several of the needs identified by Martinez

et al. (2019), providing enhanced capabilities for both the detection and response components of invasive species management.

This research offers significant implications for surface mine reclamation practices. The ability to accurately detect and map autumn olive across reclaimed landscapes provides critical information for assessing reclamation success and planning targeted interventions. As Zipper et al. (2011b) and Franke et al. (2018) recognized, autumn olive can significantly impede native forest regeneration on disturbed lands, undermining ecological and economic objectives. The identification of optimal detection windows during peak and late growing seasons can guide the timing of UAS surveys, while the finding that RGB imagery can achieve comparable accuracy to multispectral data presents opportunities for cost-effective monitoring access to reclamation practitioners with limited resources. The UAAS treatment approach addresses and demonstrates a critical gap in management options for invasive species on reclaimed lands, offering a viable alternative to traditional ground-based methods that are often impractical or prohibitively expensive on challenging terrain. With conventional autumn olive treatment costing up to \$1,166 per hectare (Byrd et al., 2012), the UAAS approach could significantly enhance feasibility and cost-effectiveness of control efforts across the extensive areas affected by surface mining. This methodological framework could also be adapted for other problematic invasive species like tree-of-heaven, multiflora rose, and lespedeza species, supporting comprehensive management plans.

Several limitations should be acknowledged when interpreting these results. The research was conducted at only two reclaimed mine sites in Monongalia County, WV, which may not fully represent the diversity of post-mining landscapes across the Appalachian region. Differences in reclamation practices, time since disturbance, substrate characteristics, and regional vegetation patterns could influence the transferability of these classification approaches. The reliance on

visual interpretation and field-verified reference data introduces potential sources of error, particularly for areas where autumn olive occurs in mixed stands or in the understory canopy. Despite the use of RTK GPS measurements and careful verification, some ambiguity in class boundaries remains inevitable in complex vegetation communities. The temporal coverage of UAS data collection, while spanning multiple phenological stages, may not have captured key transition periods with sufficient sampling or resolution, and climate variability between years likely shifted phenological timing. The U-Net implementation uses a relatively simple architecture compared to more recent advances in deep learning for crown mapping, such as the Mask R-CNN (Weinstein et al, 2019), though the strong performance achieved suggests more complex models may not offer better returns for this application. Finally, the short post-treatment monitoring period of 15 days provides only a preliminary assessment of UAAS efficacy, and seasonal variation in herbicide effectiveness with this application remains unexplored.

This research opens several promising avenues for future investigation. The integration of structural information from LiDAR or photogrammetric point clouds in addition to spectral data could enhance classification accuracy in areas with complex vertical vegetation structure, particularly for understory autumn olive. The creation of standardized and accessible benchmark datasets for invasive and native species would facilitate a more rigorous comparison of detection methods across different sites and conditions. Additionally, such a dataset would provide researchers with an immense amount of data that could already be annotated with species labels, saving an immense amount of time and energy in data collection and labeling. This would also provide the ability to test and compare different architectures and classifiers, while maintaining reproducibility between approaches. Extending beyond single species detection, multi-species models capable of simultaneously mapping several invasive plants alongside native species could

provide a powerful tool for foresters and land managers. Developing real-time detection capabilities, where UAAS mounted edge computing devices could process and classify imagery during a flight, would enable immediate and autonomous management responses that reduce the lag between detection and treatment. The temporal dynamics of detection warrant exploration through more continuous monitoring throughout the growing season, potentially leading to a more robust multi-temporal classification approach that leverages autumn olive's distinct phenology. For UAAS treatments, comparative studies evaluating different herbicide formulations and application parameters would help optimize efficacy while minimizing environmental impacts. The promising results from the RGB U-Net classification suggest opportunities for more accessible monitoring approaches using lower cost platforms and consumer grade cameras, while simplified processing workflows could enhance practical utility for routine monitoring. Economic and practical feasibility studies comparing UAS and UAAS approaches with conventional methods would provide valuable information for practitioners and regulatory agencies, especially as the use of UAASs becomes increasingly popular in the U.S. This convergence of remote sensing, machine learning, and precision application technologies represents an emerging paradigm with applications beyond reclaimed surface mines to other disturbed landscapes facing similar invasive species challenges.

## **Conclusion**

This research demonstrates that the integration of unmanned aerial systems and machine learning presents a viable approach for detecting and managing autumn olive on reclaimed surface mines. The primary objective was to develop and evaluate methodologies for the classification of *Elaeagnus umbellata* using high-resolution multispectral and RGB UAS imagery with machine learning algorithms, and to assess the feasibility of UAAS herbicide applications as a management strategy. The results confirm that both objectives were achieved with varying degrees of success across different phenological stages and model implementations.

The performance of classification models across different phenological stages affirms the importance of temporal considerations for autumn olive detection. During peak growing season, all classification models achieved their highest accuracy, with the RGB U-Net model reaching an F1-score of 0.927 for autumn olive detection. This finding suggests that the distinctive visual characteristics of autumn olive at peak foliage development, including its unique canopy texture and color patterns, provide sufficient information for accurate detection even without multispectral data. The late phenological stage also demonstrated strong detection capabilities, particularly with the RGB model achieving an F1-score of 0.912, as well as the senescence stage which achieved a moderate, yet acceptable, F1-score of 0.871. Both of these results support the previous research by Oliphant et al. (2016) regarding autumn olive's extended leaf-on period relative to native deciduous trees, which highlights its candidacy as a machine classifiable species.

While spectral analysis revealed that autumn olive consistently exhibits higher NIR reflectance than surrounding vegetation, the relative importance of specific indices shifted markedly across seasons. The temporal transition from red-edge indices dominance in early and peak stages to soil-adjusted indices in senescence represents a key insight for implementation. This

pattern suggests that optimal detection strategies should adapt to seasonal changes rather than relying on fixed methodologies year-round. The finding challenges standard approaches that emphasize NDVI regardless of season or target species.

The unexpected superior performance of the RGB U-Net model over the multispectral and VI-Composite models during peak, late, and senescence stages represents this study's most significant methodological contribution. This challenges conventional assumptions about the necessity of multispectral data for species-level classification from UAS imagery and offers significant practical implications for monitoring programs. The ability to achieve high detection accuracy using standard RGB imagery, which does not require calibration or radiometric corrections and can be collected using inexpensive sensors, could substantially reduce the barriers to implementing UAS-based monitoring for invasive species management on reclaimed surface mines.

The UAAS herbicide application demonstrated both the potential and limitations of this novel approach to autumn olive management. The aerial system effectively delivered targeted treatments while minimizing impacts on surrounding vegetation, with post-treatment assessments confirming gradual effectiveness across all application rates. The downwash effect from the UAAS rotors enhanced canopy penetration, resulting in increased uniform coverage throughout dense thickets where ground-based sprayers might struggle to achieve complete coverage as effectively and efficiently. With conventional autumn olive treatments costing up to \$1,166 per hectare (Byrd et al., 2012), the UAAS approach could significantly enhance the feasibility and cost-effectiveness of control efforts across the extensive areas affected by surface mining in the Appalachian region.

Several constraints limit the immediate generalizability of these findings. Data collection was conducted at only two reclaimed mine sites, which are within close proximity to each other.

This may not fully represent the range of post-mining landscapes across the Appalachian region. Differences in reclamation practices, time since the initial disturbance, and regional vegetation diversity could influence the ability to transfer these classification models. When annotating training data for the deep learning models, these annotations were done manually, or by hand, with reference to ground-truth locations of autumn olive. This portion of the methodology, while effective, could be enhanced with an unsupervised method of annotation, whether that be through the use of crown delineation algorithms or object-based segmentation workflows. The latter, object-based segmentation, would benefit greatly from further research as their implementation can be complicated in extremely heterogenous landscapes where canopies overlap and are irregularly shaped. Additionally, the short post-treatment monitoring period of the UAAS opens up the opportunity for a more in-depth analysis of application parameters and their effects.

This work establishes a foundation for expanding technology-enabled environmental management across disturbed landscapes. Future research should explore multi-species detection capabilities, integration of structural data to improve understory detection, real-time processing for immediate treatment responses, and comprehensive cost-benefit analyses comparing these approaches to conventional methods. Development of standardized, accessible benchmark datasets for both invasive species and native species would facilitate more rigorous comparison of detection methodologies across varied sites and conditions using UAS imagery.

By demonstrating an integrated technological framework that spans from detection to treatment, this research advances the Early Detection and Rapid Response framework outlined by Reaser et al. (2019) while addressing critical operational needs identified by Martinez et al. (2019). As reclamation practitioners confront the persistent challenge of invasive species across thousands of disturbed hectares, the methodologies developed here offer a pathway toward more efficient,

effective, and environmentally responsible management strategies that support the restoration of diverse and functional post-mining ecosystems.

### **Code and Data Availability**

The code and analysis scripts developed for this research project are available at  
<https://github.com/smk0061>

## **References**

- Abdollahi, A., & Pradhan, B. (2021). Urban vegetation mapping from aerial imagery using explainable AI (XAI). *Sensors*, 21(14), 4738. <https://doi.org/10.3390/s21144738>
- Adams, M. B., Sanderson, T., Sena, K., Barton, C., Agouridis, C., Angel, P., & Zipper, C. (2019). (rep.). *Managing Invasive Exotic Plant Species on Legacy Mine Lands*. ARRI.
- Agisoft Metashape. (n.d.). Version (2.1.2). *Agisoft Metashape Professional*. Retrieved from <https://www.agisoft.com/>.
- Ahmad, S. D., Sabir, S. M., & Zubair, M. (2006). Ecotypes diversity in Autumn olive (*elaeagnus umbellata*): A single plant with multiple micronutrient genes. *Chemistry and Ecology*, 22(6), 509–521. <https://doi.org/10.1080/02757540601024819>
- Altmann, A., Tološi, L., Sander, O., & Lengauer, T. (2010). Permutation importance: A corrected feature importance measure. *Bioinformatics*, 26(10), 1340–1347. <https://doi.org/10.1093/bioinformatics/btq134>
- Amarasingam, N., Vanegas, F., Hele, M., Warfield, A., & Gonzalez, F. (2024). Integrating Artificial Intelligence and UAV-acquired multispectral imagery for the mapping of invasive plant species in complex natural environments. *Remote Sensing*, 16(9), 1582. <https://doi.org/10.3390/rs16091582>
- Amichev, B. Y., Burger, J. A., & Rodrigue, J. A. (2008). Carbon sequestration by forests and soils on mined land in the Midwestern and Appalachian Coalfields of the U.S. *Forest Ecology and Management*, 256(11), 1949–1959. <https://doi.org/10.1016/j.foreco.2008.07.020>
- Audebert, N., Le Saux, B., & Lefevre, S. (2019). Deep learning for classification of Hyperspectral Data: A comparative review. *IEEE Geoscience and Remote Sensing Magazine*, 7(2), 159–173. <https://doi.org/10.1109/mgrs.2019.2912563>
- Baron, J., Hill, D. J., & Elmiligi, H. (2018). Combining image processing and machine learning to identify invasive plants in high-resolution images. *International Journal of Remote Sensing*, 39(15–16), 5099–5118. <https://doi.org/10.1080/01431161.2017.1420940>
- Barzin, R., Pathak, R., Lotfi, H., Varco, J., & Bora, G. C. (2020). Use of UAS multispectral imagery at different physiological stages for yield prediction and input resource optimization in corn. *Remote Sensing*, 12(15), 2392. <https://doi.org/10.3390/rs12152392>
- Beland, M., Parker, G., Sparrow, B., Harding, D., Chasmer, L., Phinn, S., Antonarakis, A., & Strahler, A. (2019). On promoting the use of lidar systems in Forest Ecosystem Research. *Forest Ecology and Management*, 450, 117484. <https://doi.org/10.1016/j.foreco.2019.117484>
- Belgiu, M., & Drăguț, L. (2016). Random Forest in remote sensing: A review of applications and Future Directions. *ISPRS Journal of Photogrammetry and Remote Sensing*, 114, 24–31. <https://doi.org/10.1016/j.isprsjprs.2016.01.011>
- Bernhardt, E. S., & Palmer, M. A. (2011). The environmental costs of mountaintop mining valley fill operations for aquatic ecosystems of the central appalachians. *Annals of the New York Academy of Sciences*, 1223(1), 39–57. <https://doi.org/10.1111/j.1749-6632.2011.05986.x>
- Black, B., Fordham, I., & Perkins, P. (2005). Autumnberry (*Elaeagnus umbellata*): A potential cash crop. *American Pomological Society*.
- Breiman, L. (2001). Random Forests. *Machine Learning*, 45(1), 5–32. <https://doi.org/10.1023/a:1010933404324>
- Breiman, L., Cutler, A., Liaw, A., & Wiener, M. (2024). randomForestVersion (4.7-1.2). *randomForest: Breiman and Cutler's Random Forests for Classification and Regression*. Retrieved from <https://CRAN.R-project.org/package=randomForest>.
- Brym, Z. T., Lake, J. K., Allen, D., & Ostling, A. (2011). Plant functional traits suggest novel ecological strategy for an invasive shrub in an understorey Woody Plant Community. *Journal of Applied Ecology*, 48(5), 1098–1106. <https://doi.org/10.1111/j.1365-2664.2011.02049.x>
- Burger, J. A. (2011). Sustainable mined land reclamation in the eastern U. S. coalfields: A case for an ecosystem reclamation approach. *Journal American Society of Mining and Reclamation*, 2011(1), 113–141. <https://doi.org/10.21000/jasmr11010113>
- Burger, J., Zipper, C., Angel, P., Evans, D., & Eggerud, S. (2011). Reforestation guidelines for unused surface mined lands: Development, application and adoption. *Journal American Society of Mining and Reclamation*, 2011(1), 90–112. <https://doi.org/10.21000/jasmr11010090>
- Burger, James, Davis, V., Franklin, J., Skousen, J., Barton, C., & Angel, P. (2009). (rep.). *Tree-Compatible Ground Covers for Reforestation and Erosion Control*. ARRI.
- Burger, Jim, Graves, D., Angel, P., & Zipper, C. (2005). (rep.). *The Forestry Reclamation Approach*. ARRI.

- Byrd, S. M., Cavender, N. D., Peugh, C. M., & Bauman, J. M. (2012). Sustainable landscapes: Evaluating strategies for controlling Autumn olive (*elaeagnus umbellata*) on reclaimed surface Mineland at the Wilds Conservation Center in Southeastern Ohio. *Journal American Society of Mining and Reclamation*, 2012(1), 73–81. <https://doi.org/10.21000/jasmr12010073>
- Campos, J., Llop, J., Gallart, M., García-Ruiz, F., Gras, A., Salcedo, R., & Gil, E. (2019). Development of canopy vigour maps using UAV for site-specific management during vineyard spraying process. *Precision Agriculture*, 20(6), 1136–1156. <https://doi.org/10.1007/s11119-019-09643-z>
- Cavender, N., Byrd, S., Bechtoldt, C. L., & Bauman, J. M. (2014). Vegetation communities of a coal reclamation site in southeastern Ohio. *Northeastern Naturalist*, 21(1), 31–46. <https://doi.org/10.1656/045.021.0104>
- Colomina, I., & Molina, P. (2014). Unmanned aerial systems for photogrammetry and Remote Sensing: A Review. *ISPRS Journal of Photogrammetry and Remote Sensing*, 92, 79–97. <https://doi.org/10.1016/j.isprsjprs.2014.02.013>
- Cromwell, C., Giampaolo, J., Hupy, J., Miller, Z., & Chandrasekaran, A. (2021). A systematic review of best practices for UAS Data Collection in forestry-related applications. *Forests*, 12(7), 957. <https://doi.org/10.3390/f12070957>
- Dallaire, K., & Skousen, J. (2019). Early tree growth in reclaimed mine soils in Appalachia USA. *Forests*, 10(7), 549. <https://doi.org/10.3390/f10070549>
- Daniels, N. K., LaBar, J. A., & McDonald, L. M. (2020). Acid mine drainage in Appalachia: Sources, legacy, and treatment. *Appalachia's Coal-Mined Landscapes*, 193–216. [https://doi.org/10.1007/978-3-030-57780-3\\_8](https://doi.org/10.1007/978-3-030-57780-3_8)
- Dash, J. P., Watt, M. S., Pearse, G. D., Heaphy, M., & Dungey, H. S. (2017). Assessing very high resolution UAV imagery for monitoring forest health during a simulated disease outbreak. *ISPRS Journal of Photogrammetry and Remote Sensing*, 131, 1–14. <https://doi.org/10.1016/j.isprsjprs.2017.07.007>
- Davis, V., Burger, J., Rathfon, R., Zipper, C., & Miller, C. (2012). (rep.). *Selecting tree species for reforestation of Appalachian mined lands*. ARRI.
- Dirr, M. A. (1983). *Manual of woody landscape plants: Their identification, ornamental characteristics, culture, propagation and uses*. Stipes.
- DJI. (n.d.). DJI SmartFarmVersion (4.18.1). *DJI SmartFarm App*. Retrieved from <https://www.dji.com/ag-platform>.
- Drummond, M. A., & Loveland, T. R. (2010). Land-use pressure and a transition to forest-cover loss in the Eastern United States. *BioScience*, 60(4), 286–298. <https://doi.org/10.1525/bio.2010.60.4.7>
- Esri. (n.d.). Version (3.4). *ArcGIS Pro*. Retrieved from <https://www.esri.com/en-us/arcgis/products/arcgis-pro/overview>.
- Evans, D. M., Zipper, C. E., Burger, J. A., Strahm, B. D., & Villamagna, A. M. (2013). Reforestation practice for enhancement of ecosystem services on a compacted surface mine: Path toward Ecosystem Recovery. *Ecological Engineering*, 51, 16–23. <https://doi.org/10.1016/j.ecoleng.2012.12.065>
- Evans, D. M., Zipper, C. E., Hester, E. T., & Schoenholtz, S. H. (2015). Hydrologic effects of surface coal mining in Appalachia. *JAWRA Journal of the American Water Resources Association*, 51(5), 1436–1452. <https://doi.org/10.1111/1752-1688.12322>
- Executive Office of the President. (2016). (rep.). *Safeguarding the Nation from the Impacts of Invasive Species* (236th ed., Vol. 81, pp. 88609–88614).
- Ezzarrouqy, K., Sbahi, S., Hejjaj, A., Idlimam, A., & Mandi, L. (2023). A green extraction method of phenolic compounds from olive leaves (*Olea europaea L.*): Evaluation and prediction using multiple linear regression. *International Journal of Environmental Science and Technology*, 21(4), 3761–3774. <https://doi.org/10.1007/s13762-023-05224-w>
- Fan, J., Zhou, J., Wang, B., de Leon, N., Kaepller, S. M., Lima, D. C., & Zhang, Z. (2022). Estimation of maize yield and flowering time using multi-temporal UAV-based Hyperspectral Data. *Remote Sensing*, 14(13), 3052. <https://doi.org/10.3390/rs14133052>
- Federal Aviation Administration. (1965). Agricultural aircraft operations, 14 C.F.R. Part 137. Retrieved from <https://www.ecfr.gov/current/title-14/chapter-I/subchapter-G/part-137>
- Federal Aviation Administration. (2016). Operation and certification of small unmanned aircraft systems, 14 C.F.R. Part 107. <https://www.ecfr.gov/current/title-14/chapter-I/subchapter-F/part-107>
- Federal Aviation Administration. (2025). General operating and flight rules, 14 C.F.R. Part 91. <https://www.ecfr.gov/current/title-14/chapter-I/subchapter-F/part-91>
- Federal Interagency Committee for the Management of Noxious and Exotic Weeds. (2003). A national early detection and rapid response system for invasive plants in the United States: Conceptual design. Washington, DC: FICMNEW.

- Feng, Q., Yang, J., Liu, Y., Ou, C., Zhu, D., Niu, B., Liu, J., & Li, B. (2020). Multi-temporal unmanned aerial vehicle remote sensing for vegetable mapping using an attention-based recurrent convolutional neural network. *Remote Sensing*, 12(10), 1668. <https://doi.org/10.3390/rs12101668>
- Fields-Johnson, C. W., Zipper, C. E., Burger, J. A., & Evans, D. M. (2012). Forest restoration on steep slopes after coal surface mining in Appalachian USA: Soil grading and seeding effects. *Forest Ecology and Management*, 270, 126–134. <https://doi.org/10.1016/j.foreco.2012.01.018>
- Franke, M. E., Zipper, C., & Barney, J. N. (2018). Invasive autumn olive performance varies in different reclamation conditions: Implications for restoration. *Restoration Ecology*, 27(3), 600–606. <https://doi.org/10.1111/rec.12906>
- Franklin, J. A., Zipper, C. E., Burger, J. A., Skousen, J. G., & Jacobs, D. F. (2012). Influence of herbaceous ground cover on forest restoration of eastern US coal surface mines. *New Forests*, 43(5–6), 905–924. <https://doi.org/10.1007/s11056-012-9342-8>
- Fraser, B. T., & Congalton, R. G. (2018). Issues in unmanned aerial systems (UAS) data collection of Complex Forest Environments. *Remote Sensing*, 10(6), 908. <https://doi.org/10.3390/rs10060908>
- Fraser, B. T., & Congalton, R. G. (2021). Monitoring fine-scale forest health using unmanned aerial systems (UAS) multispectral models. *Remote Sensing*, 13(23), 4873. <https://doi.org/10.3390/rs13234873>
- Gorelick, N., Hancher, M., Dixon, M., Ilyushchenko, S., Thau, D., & Moore, R. (2017). Google Earth Engine: Planetary-scale geospatial analysis for everyone. *Remote Sensing of Environment*, 202, 18–27. <https://doi.org/10.1016/j.rse.2017.06.031>
- Greenwell, B. (2024). fastshapVersion (0.1.1). *fastshap: Fast Approximate Shapley Values*. Retrieved from <https://CRAN.R-project.org/package=fastshap>.
- Greer, B. M., Burbey, T. J., Zipper, C. E., & Hester, E. T. (2017). Electrical resistivity imaging of hydrologic flow through surface coal mine valley fills with comparison to other landforms. *Hydrological Processes*, 31(12), 2244–2260. <https://doi.org/10.1002/hyp.11180>
- Groninger, J., Skousen, J., Angel, P., Barton, C., & Burger, J. (2007). (rep.). *Mine reclamation practices to enhance forest development through natural succession*. ARRI.
- Guo, Y., Zhao, Y., Rothfus, T. A., & Avalos, A. S. (2022). A novel invasive plant detection approach using time series images from unmanned aerial systems based on convolutional and Recurrent Neural Networks. *Neural Computing and Applications*, 34(22), 20135–20147. <https://doi.org/10.1007/s00521-022-07560-3>
- Haering, K. C., Daniels, W. L., & Galbraith, J. M. (2004). Appalachian mine soil morphology and properties. *Soil Science Society of America Journal*, 68(4), 1315–1325. <https://doi.org/10.2136/sssaj2004.1315>
- Hanif, A. S., Han, X., & Yu, S.-H. (2022). Independent control spraying system for UAV-based precise variable sprayer: A Review. *Drones*, 6(12), 383. <https://doi.org/10.3390/drones6120383>
- Harper, K. A., Macdonald, S. E., Burton, P. J., Chen, J., Brosofske, K. D., Saunders, S. C., Euskirchen, E. S., Roberts, D., Jaitah, M. S., & Esseen, P.-A. (2005). Edge influence on forest structure and composition in fragmented landscapes. *Conservation Biology*, 19(3), 768–782. <https://doi.org/10.1111/j.1523-1739.2005.00045.x>
- Harris, R. C., Kennedy, L. M., Pingel, T. J., & Thomas, V. A. (2022). Assessment of Canopy Health with drone-based orthoimagery in a Southern Appalachian Red Spruce Forest. *Remote Sensing*, 14(6), 1341. <https://doi.org/10.3390/rs14061341>
- Hester, E. T., Little, K. L., Buckwalter, J. D., Zipper, C. E., & Burbey, T. J. (2019). Variability of subsurface structure and infiltration hydrology among surface coal mine valley fills. *Science of The Total Environment*, 651, 2648–2661. <https://doi.org/10.1016/j.scitotenv.2018.10.169>
- Howard, J. (2019). Artificial Intelligence: Implications for the future of work. *American Journal of Industrial Medicine*, 62(11), 917–926. <https://doi.org/10.1002/ajim.23037>
- Huelsman, K., Epstein, H., Yang, X., Mullori, L., Červená, L., & Walker, R. (2023). Spectral variability in fine-scale drone-based imaging spectroscopy does not impede detection of target invasive plant species. *Frontiers in Remote Sensing*, 3. <https://doi.org/10.3389/frsen.2022.1085808>
- Hunt, E. R., & Daughtry, C. S. (2017). What good are unmanned aircraft systems for agricultural remote sensing and precision agriculture? *International Journal of Remote Sensing*, 39(15–16), 5345–5376. <https://doi.org/10.1080/01431161.2017.1410300>
- Ioffe, S., & Szegedy, C. (2015). *Batch Normalization: Accelerating Deep Network Training by Reducing Internal Covariate Shift*. <https://doi.org/https://doi.org/https://doi.org/10.48550/arXiv.1502.03167>
- Kattenborn, T., Leitloff, J., Schiefer, F., & Hinz, S. (2021). Review on Convolutional Neural Networks (CNN) in Vegetation Remote Sensing. *ISPRS Journal of Photogrammetry and Remote Sensing*, 173, 24–49. <https://doi.org/10.1016/j.isprsjprs.2020.12.010>

- Kattenborn, T., Lopatin, J., Förster, M., Braun, A. C., & Fassnacht, F. E. (2019). UAV data as alternative to field sampling to map woody invasive species based on combined sentinel-1 and sentinel-2 data. *Remote Sensing of Environment*, 227, 61–73. <https://doi.org/10.1016/j.rse.2019.03.025>
- Kislov, D. E., Korznikov, K. A., Altman, J., Vozmishcheva, A. S., & Krestov, P. V. (2021). Extending deep learning approaches for forest disturbance segmentation on very high-resolution satellite images. *Remote Sensing in Ecology and Conservation*, 7(3), 355–368. <https://doi.org/10.1002/rse2.194>
- Lachowiec, J., Feldman, M. J., Matias, F. I., LeBauer, D., & Gregory, A. (2024). Adoption of unoccupied aerial systems in Agricultural Research. *The Plant Phenome Journal*, 7(1). <https://doi.org/10.1002/ppj2.20098>
- Lemke, D., Schweitzer, C. J., Tazisong, I. A., Wang, Y., & Brown, J. A. (2013). Invasion of a mined landscape: What habitat characteristics are influencing the occurrence of invasive plants? *International Journal of Mining, Reclamation and Environment*, 27(4), 275–293. <https://doi.org/10.1080/17480930.2012.699215>
- Li, X., Stainback, A., Barton, C., & Yang, J. (2018). Valuing the environmental benefits from reforestation on reclaimed surface mines in Appalachia. *Journal American Society of Mining and Reclamation*, 7(1), 1–29. <https://doi.org/10.21000/jasmr18010001>
- Lin, T.-Y., Goyal, P., Girshick, R., He, K., & Dollar, P. (2020). Focal loss for dense object detection. *IEEE Transactions on Pattern Analysis and Machine Intelligence*, 42(2), 318–327. <https://doi.org/10.1109/tpami.2018.2858826>
- Lituma, C. M., Cox, J. J., Spear, S. F., Edwards, J. W., De La Cruz, J. L., Muller, L. I., & Ford, W. M. (2020). Terrestrial wildlife in the post-mined Appalachian Landscape: Status and Opportunities. *Appalachia's Coal-Mined Landscapes*, 135–166. [https://doi.org/10.1007/978-3-030-57780-3\\_6](https://doi.org/10.1007/978-3-030-57780-3_6)
- Liu, Y., Yao, W., Guo, S., Yan, H., Yu, Z., Meng, S., Chen, D., & Chen, C. (2024). Determination of the effective swath of a plant protection UAV adapted to mist nozzles in Mountain Nangguo pear orchards. *Frontiers in Plant Science*, 15. <https://doi.org/10.3389/fpls.2024.1336580>
- Loshchilov, I., & Hutter, F. (2019). *Decoupled Weight Decay Regularization*. <https://doi.org/https://doi.org/10.48550/arXiv.1711.05101>
- Lundberg, S., & Lee, S. I. (2017). *A Unified Approach to Interpreting Model Predictions*. <https://doi.org/https://doi.org/10.48550/arXiv.1705.07874>
- Ma, Y., Zhao, Y., Im, J., Zhao, Y., & Zhen, Z. (2024). A deep-learning-based tree species classification for natural secondary forests using unmanned aerial vehicle hyperspectral images and Lidar. *Ecological Indicators*, 159, 111608. <https://doi.org/10.1016/j.ecolind.2024.111608>
- Marshall Meyers, N., Reaser, J. K., & Hoff, M. H. (2019). Instituting a national early detection and rapid response program: Needs for building federal risk screening capacity. *Biological Invasions*, 22(1), 53–65. <https://doi.org/10.1007/s10530-019-02144-0>
- Martinez, B., Reaser, J. K., Dehgan, A., Zamft, B., Baisch, D., McCormick, C., Giordano, A. J., Aicher, R., & Selbe, S. (2019). Technology innovation: Advancing capacities for the early detection of and rapid response to invasive species. *Biological Invasions*, 22(1), 75–100. <https://doi.org/10.1007/s10530-019-02146-y>
- Maxwell, A. E., & Strager, M. P. (2013). Assessing landform alterations induced by mountaintop mining. *Natural Science*, 05(02), 229–237. <https://doi.org/10.4236/ns.2013.52a034>
- Maxwell, A. E., Warner, T. A., & Fang, F. (2018). Implementation of machine-learning classification in Remote Sensing: An applied review. *International Journal of Remote Sensing*, 39(9), 2784–2817. <https://doi.org/10.1080/01431161.2018.1433343>
- Maxwell, A. E., Warner, T. A., Strager, M. P., & Pal, M. (2014). Combining RapidEye satellite imagery and lidar for mapping of Mining and Mine Reclamation. *Photogrammetric Engineering & Remote Sensing*, 80(2), 179–189. <https://doi.org/10.14358/pers.80.2.179-189>
- Meesaragandla, S., Jagtap, M. P., Khatri, N., Madan, H., & Vadduri, A. A. (2024). Herbicide spraying and weed identification using drone technology in Modern Farms: A comprehensive review. *Results in Engineering*, 21, 101870. <https://doi.org/10.1016/j.rineng.2024.101870>
- Mehendale, N., & Neoge, S. (2020). Review on lidar technology. *SSRN Electronic Journal*. <https://doi.org/10.2139/ssrn.3604309>
- Mesa, A. N., Strager, M. P., Grushecky, S. T., & Kinder, P. (2023). Using unmanned aerial vehicles to evaluate revegetation success on natural gas pipelines. *Environmental Management*, 72(3), 671–681. <https://doi.org/10.1007/s00267-023-01842-9>
- Miao, S., Wang, C., Kong, G., Yuan, X., Shen, X., & Liu, C. (2024). Utilizing active learning and attention-CNN to classify vegetation based on UAV multispectral data. *Scientific Reports*, 14(1). <https://doi.org/10.1038/s41598-024-82248-3>

- Millard, K., & Richardson, M. (2015). On the importance of training data sample selection in random forest image classification: A case study in Peatland Ecosystem Mapping. *Remote Sensing*, 7(7), 8489–8515. <https://doi.org/10.3390/rs70708489>
- Mine Safety and Health Administration, Mine safety and health at a glance: Fiscal year 2022 (2022). Washington, D.C.; U.S. Department of Labor.
- Morisette, J. T., Reaser, J. K., Cook, G. L., Irvine, K. M., & Roy, H. E. (2019). Right place. right time. right tool: Guidance for using target analysis to increase the likelihood of invasive species detection. *Biological Invasions*, 22(1), 67–74. <https://doi.org/10.1007/s10530-019-02145-z>
- Müllerová, J., Bartaloš, T., Brůna, J., Dvořák, P., & Vítková, M. (2017). Unmanned Aircraft in nature conservation: An example from plant invasions. *International Journal of Remote Sensing*, 38(8–10), 2177–2198. <https://doi.org/10.1080/01431161.2016.1275059>
- National Research Council. (2007). Coal: Research and development to support national energy policy. *The National Academies Press*. <https://doi.org/10.17226/11977>
- Nippgen, F., Ross, M. R., Bernhardt, E. S., & McGlynn, B. L. (2017). Creating a more perennial problem? mountaintop removal coal mining enhances and sustains saline baseflows of Appalachian watersheds. *Environmental Science & Technology*, 51(15), 8324–8334. <https://doi.org/10.1021/acs.est.7b02288>
- Office of Surface Mining Reclamation and Enforcement, FY 2020 Annual Report (2020). Washington, D.C.; U.S. Department of Interior.
- Oliphant, A. J., Wynne, R. H., Zipper, C. E., Ford, W. M., Donovan, P. F., & Li, J. (2016). Autumn olive (*elaeagnus umbellata*) presence and proliferation on former surface coal mines in Eastern USA. *Biological Invasions*, 19(1), 179–195. <https://doi.org/10.1007/s10530-016-1271-6>
- Onishi, M., & Ise, T. (2021). Explainable identification and mapping of trees using UAV RGB image and deep learning. *Scientific Reports*, 11(1). <https://doi.org/10.1038/s41598-020-79653-9>
- Palmer, M. A., Bernhardt, E. S., Schlesinger, W. H., Eshleman, K. N., Foufoula-Georgiou, E., Hendryx, M. S., Lemly, A. D., Likens, G. E., Loucks, O. L., Power, M. E., White, P. S., & Wilcock, P. R. (2010). Mountaintop Mining Consequences. *Science*, 327(5962), 148–149. <https://doi.org/10.1126/science.1180543>
- Pascanu, R., Mikolov, T., & Bengio, Y. (2013). *On the Difficulty of Training Recurrent Neural Networks*. <https://doi.org/https://doi.org/10.48550/arXiv.1211.5063>
- Paszke, A., Gross, S., Massa, F., Lerer, A., Bradbury, J., Chanan, G., Killeen, T., & Lin, Z. (n.d.). PyTorchVersion (2.7.0). *PyTorch: An Imperative Style, High-Performance Deep Learning Library*. Retrieved from <http://papers.neurips.cc/paper/9015-pytorch-an-imperative-style-high-performance-deep-learning-library.pdf>.
- Paudel, K., Gyawali, B., Zourarakis, D. P., Gebremedhin, M., & Lucas, S. T. (2024). Use of lidar for monitoring vegetation growth dynamics in reclaimed mine lands in Kentucky. *Remote Sensing Applications: Society and Environment*, 36, 101277. <https://doi.org/10.1016/j.rsase.2024.101277>
- Pederi, Y. A., & Cheporniuk, H. S. (2015). Unmanned aerial vehicles and new technological methods of monitoring and crop protection in Precision Agriculture. *2015 IEEE International Conference Actual Problems of Unmanned Aerial Vehicles Developments (APUAVD)*, 298–301. <https://doi.org/10.1109/apuavd.2015.7346625>
- Pericak, A. A., Thomas, C. J., Kroodsma, D. A., Wasson, M. F., Ross, M. R., Clinton, N. E., Campagna, D. J., Franklin, Y., Bernhardt, E. S., & Amos, J. F. (2018). Mapping the yearly extent of surface coal mining in central Appalachia using landsat and google earth engine. *PLOS ONE*, 13(7). <https://doi.org/10.1371/journal.pone.0197758>
- Phillips, C., Stovall, J., Williams, H., & Farrish, K. (2021). Using the forestry reclamation approach for reclaimed surface Mineland in the Western Gulf: Effects on *pinus taeda* seedling growth and survival. *Forests*, 12(7), 845. <https://doi.org/10.3390/f12070845>
- Pichler, M., & Hartig, F. (2023). Machine learning and deep learning—a review for ecologists. *Methods in Ecology and Evolution*, 14(4), 994–1016. <https://doi.org/10.1111/2041-210x.14061>
- Plass, W. T. (2015). History of surface mining reclamation and associated legislation. *Agronomy Monographs*, 1–20. <https://doi.org/10.2134/agronmonogr41.c1>
- Pádua, L., Antão-Geraldes, A. M., Sousa, J. J., Rodrigues, M. Â., Oliveira, V., Santos, D., Miguens, M. F., & Castro, J. P. (2022). Water Hyacinth (*eichhornia crassipes*) detection using coarse and high resolution multispectral data. *Drones*, 6(2), 47. <https://doi.org/10.3390/drones6020047>
- Pádua, L., Vanko, J., Hruška, J., Adão, T., Sousa, J. J., Peres, E., & Morais, R. (2017). UAS, sensors, and data processing in agroforestry: A review towards practical applications. *International Journal of Remote Sensing*, 38(8–10), 2349–2391. <https://doi.org/10.1080/01431161.2017.1297548>

- Reaser, J. K., Burgiel, S. W., Kirkey, J., Brantley, K. A., Veatch, S. D., & Burgos-Rodríguez, J. (2019). The early detection of and rapid response (EDRR) to invasive species: A conceptual framework and federal capacities assessment. *Biological Invasions*, 22(1), 1–19. <https://doi.org/10.1007/s10530-019-02156-w>
- Resop, J. P., Lehmann, L., & Hession, W. C. (2019). Drone laser scanning for modeling riverscape topography and vegetation: Comparison with Traditional Aerial Lidar. *Drones*, 3(2), 35. <https://doi.org/10.3390/drones3020035>
- Ricketts, T. H. (1999). *Terrestrial ecoregions of North America: A conservation assessment*. Island Press.
- Riffe, E. C. (2018). *A study of autumn olive (*Elaeagnus umbellata*) phenology and associated physiological traits that may facilitate its invasion of the understory of a Southern Appalachian forest* (thesis). Appalachian State University.
- Riitters, K. H., Wickham, J. D., O'Neill, R. V., Jones, K. B., Smith, E. R., Coulston, J. W., Wade, T. G., & Smith, J. H. (2002). Fragmentation of continental United States forests. *Ecosystems*, 5(8), 815–822. <https://doi.org/10.1007/s10021-002-0209-2>
- Riitters, K., Wickham, J., O'Neill, R., Jones, B., & Smith, E. (2000). Global-Scale Patterns of Forest Fragmentation. *Conservation Ecology*.
- Rodriguez-Galiano, V. F., Ghimire, B., Rogan, J., Chica-Olmo, M., & Rigol-Sánchez, J. P. (2012). An assessment of the effectiveness of a random forest classifier for land-cover classification. *ISPRS Journal of Photogrammetry and Remote Sensing*, 67, 93–104. <https://doi.org/10.1016/j.isprsjprs.2011.11.002>
- Rogers, S. R., Manning, I., & Livingstone, W. (2020). Comparing the spatial accuracy of digital surface models from four unoccupied aerial systems: Photogrammetry versus lidar. *Remote Sensing*, 12(17), 2806. <https://doi.org/10.3390/rs12172806>
- Ronneberger, O., Fischer, P., & Brox, T. (2015). U-Net: Convolutional Networks for Biomedical Image Segmentation. *Lecture Notes in Computer Science*, 234–241. [https://doi.org/10.1007/978-3-319-24574-4\\_28](https://doi.org/10.1007/978-3-319-24574-4_28)
- Roscher, R., Bohn, B., Duarte, M. F., & Garske, J. (2020). Explainable machine learning for scientific insights and discoveries. *IEEE Access*, 8, 42200–42216. <https://doi.org/10.1109/access.2020.2976199>
- Ross, M. R., McGlynn, B. L., & Bernhardt, E. S. (2016). Deep impact: Effects of mountaintop mining on surface topography, bedrock structure, and downstream waters. *Environmental Science & Technology*, 50(4), 2064–2074. <https://doi.org/10.1021/acs.est.5b04532>
- Ross, M. R., Nippgen, F., McGlynn, B. L., Thomas, C. J., Brooks, A. C., Shriver, R. K., Moore, E. M., & Bernhardt, E. S. (2021). Mountaintop mining legacies constrain ecological, hydrological and biogeochemical recovery trajectories. *Environmental Research Letters*, 16(7), 075004. <https://doi.org/10.1088/1748-9326/ac09ac>
- Ruggles, T. A., Gerrath, J. A., Ruhm, C. T., Jefferson, A. J., Davis, C. A., & Blackwood, C. B. (2021). Surface mines show little progress towards native species forest restoration following 35 years of passive management after initial reclamation. *Land Degradation & Development*, 32(7), 2351–2359. <https://doi.org/10.1002/lrd.3904>
- Rußwurm, M., & Körner, M. (2018). Multi-temporal land cover classification with sequential recurrent encoders. *ISPRS International Journal of Geo-Information*, 7(4), 129. <https://doi.org/10.3390/ijgi7040129>
- Rußwurm, M., & Körner, M. (2020). Self-attention for Raw Optical Satellite Time Series classification. *ISPRS Journal of Photogrammetry and Remote Sensing*, 169, 421–435. <https://doi.org/10.1016/j.isprsjprs.2020.06.006>
- Schonberger, J. L., & Frahm, J.-M. (2016). Structure-from-motion revisited. *2016 IEEE Conference on Computer Vision and Pattern Recognition (CVPR)*. <https://doi.org/10.1109/cvpr.2016.445>
- Seelig, H. D., Hoehn, A., Stodieck, L. S., Klaus, D. M., Adams III, W. W., & Emery, W. J. (2008). The assessment of leaf water content using leaf reflectance ratios in the visible, near-, and short-wave-infrared. *International Journal of Remote Sensing*, 29(13), 3701–3713. <https://doi.org/10.1080/01431160701772500>
- Selvaraju, R. R., Cogswell, M., Das, A., Vedantam, R., Parikh, D., & Batra, D. (2017). Grad-cam: Visual explanations from deep networks via gradient-based localization. *2017 IEEE International Conference on Computer Vision (ICCV)*, 618–626. <https://doi.org/10.1109/iccv.2017.74>
- Sena, K., Barton, C., Hall, S., Angel, P., Agouridis, C., & Warner, R. (2014). Influence of spoil type on afforestation success and natural vegetative recolonization on a surface coal mine in Appalachia, United States. *Restoration Ecology*, 23(2), 131–138. <https://doi.org/10.1111/rec.12164>
- Sena, K., Franklin, J. A., Swab, R. M., & Hall, S. L. (2020). Plant Communities on appalachian mined lands. *Appalachia's Coal-Mined Landscapes*, 111–134. [https://doi.org/10.1007/978-3-030-57780-3\\_5](https://doi.org/10.1007/978-3-030-57780-3_5)
- Sentera. (n.d.). 6X Sensor Series. Retrieved from <https://senterasensors.com/6x/>

- Singh, K. K., Surasinghe, T. D., & Frazier, A. E. (2024). Systematic Review and best practices for drone remote sensing of invasive plants. *Methods in Ecology and Evolution*, 15(6), 998–1015. <https://doi.org/10.1111/2041-210x.14330>
- Skousen, J., & Zipper, C. E. (2014). Post-mining policies and practices in the Eastern USA Coal Region. *International Journal of Coal Science & Technology*, 1(2), 135–151. <https://doi.org/10.1007/s40789-014-0021-6>
- Skousen, J., & Zipper, C. E. (2020). Coal Mining and Reclamation in Appalachia. *Appalachia's Coal-Mined Landscapes*, 55–83. [https://doi.org/10.1007/978-3-030-57780-3\\_3](https://doi.org/10.1007/978-3-030-57780-3_3)
- Skousen, J., Daniels, W. L., & Zipper, C. E. (2020). Soils on Appalachian coal-mined lands. *Appalachia's Coal-Mined Landscapes*, 85–109. [https://doi.org/10.1007/978-3-030-57780-3\\_4](https://doi.org/10.1007/978-3-030-57780-3_4)
- Sleeter, B. M., Sohl, T. L., Loveland, T. R., Auch, R. F., Acevedo, W., Drummond, M. A., Sayler, K. L., & Stehman, S. V. (2013). Land-cover change in the conterminous United States from 1973 to 2000. *Global Environmental Change*, 23(4), 733–748. <https://doi.org/10.1016/j.gloenvcha.2013.03.006>
- Smith, L. N. (2018). *A Disciplined Approach to Neural Network Hyper-Parameters: Part 1 -- Learning Rate, Batch Size, Momentum, and Weight Decay*. <https://doi.org/https://doi.org/10.48550/arXiv.1803.09820>
- Soulard, C. E., Acevedo, W., Stehman, S. V., & Parker, O. P. (2015). Mapping extent and change in surface mines within the United States for 2001 to 2006. *Land Degradation & Development*, 27(2), 248–257. <https://doi.org/10.1002/lrd.2412>
- Strager, M. P., Hentz, A. M., Kinder, P., & Grushecky, S. (2020). Using unmanned aerial vehicles to model surface runoff during well pad development. *Journal American Society of Mining and Reclamation*, 2020(1), 51–69. <https://doi.org/10.21000/jasmr200100051>
- Suomalainen, J., Oliveira, R. A., Hakala, T., Koivumäki, N., Markelin, L., Näsi, R., & Honkavaara, E. (2021). Direct reflectance transformation methodology for drone-based hyperspectral imaging. *Remote Sensing of Environment*, 266, 112691. <https://doi.org/10.1016/j.rse.2021.112691>
- Takekawa, J. Y., Hagani, J. S., Edmunds, T. J., Collins, J. M., Chappell, S. C., & Reynolds, W. H. (2023). The sky is not the limit: Use of a spray drone for the precise application of herbicide and control of an invasive plant in managed wetlands. *Remote Sensing*, 15(15), 3845. <https://doi.org/10.3390/rs15153845>
- Thomas, C. J., Shriver, R. K., Nippgen, F., Hepler, M., & Ross, M. R. (2022). Mines to forests? analyzing long-term recovery trends for surface coal mines in Central Appalachia. *Restoration Ecology*, 31(5). <https://doi.org/10.1111/rec.13827>
- Thompson, R. L., Vogel, W. G., & Taylor, D. D. (1984). *Vegetation and flora of a coal surface-mined area in Laurel County, Kentucky*. Southern Appalachian Botanical Society.
- Tmušić, G., Manfreda, S., Aasen, H., James, M. R., Gonçalves, G., Ben-Dor, E., Brook, A., Polinova, M., Arranz, J. J., Mészáros, J., Zhuang, R., Johansen, K., Malbeteau, Y., de Lima, I. P., Davids, C., Herban, S., & McCabe, M. F. (2020). Current practices in UAS-based environmental monitoring. *Remote Sensing*, 12(6), 1001. <https://doi.org/10.3390/rs12061001>
- Tompson, J., Goroshin, R., Jain, A., LeCun, Y., & Bregler, C. (2015). Efficient object localization using convolutional networks. *2015 IEEE Conference on Computer Vision and Pattern Recognition (CVPR)*. <https://doi.org/10.1109/cvpr.2015.7298664>
- U.S. Congress. (1977). Surface Mining Control and Reclamation Act of 1977, 30 U.S.C. §§ 1201–1328. <https://www.govinfo.gov/content/pkg/COMPS-1574/pdf/COMPS-1574.pdf>
- U.S. Energy Information Administration. (2024). Annual coal report 2023 (Table 1). U.S. Department of Energy. <https://www.eia.gov/coal/annual/pdf/table1.pdf>
- U.S. Energy Information Administration. (2024). Annual coal report 2023 (Table 5). U.S. Department of Energy. <https://www.eia.gov/coal/annual/pdf/table5.pdf>
- U.S. Energy Information Administration. (2024). Annual coal report 2023 (Table ES1). U.S. Department of Energy. <https://www.eia.gov/coal/annual/pdf/tablees1.pdf>
- U.S. Energy Information Administration. (2024). Annual coal report 2023. U.S. Department of Energy. <https://www.eia.gov/coal/annual/pdf/acr.pdf>
- U.S. EPA. The Effects Of Mountaintop Mines And Valley Fills On Aquatic Ecosystems Of The Central Appalachian Coalfields (2011 Final). U.S. Environmental Protection Agency, Washington, DC, EPA/600/R-09/138F, 2011.
- UNBC GIS Lab. (2024). *Remote Sensing and the electromagnetic spectrum*. Remote sensing and the electromagnetic spectrum. <https://gis.unbc.ca/wp-content/uploads/2024/09/spectrum2024new-web.pdf>

- Ustin, S. L., & Jacquemoud, S. (2020). How the optical properties of leaves modify the absorption and scattering of energy and enhance leaf functionality. *Remote Sensing of Plant Biodiversity*, 349–384. [https://doi.org/10.1007/978-3-030-33157-3\\_14](https://doi.org/10.1007/978-3-030-33157-3_14)
- Wade, G. L., Thompson, R. L., Vogel, W. G., & Vogel, W. G. (1985). *Success of Trees and Shrubs in an 18-Year-Old Planting on Mine Spoil*. <https://doi.org/10.2737/ne-rp-567>
- Walker, M., & Dahle, G. A. (2023). Literature Review of Unmanned Aerial Systems and LIDAR with application to distribution utility vegetation management. *Arboriculture & Urban Forestry*, 49(3), 144–156. <https://doi.org/10.48044/jauf.2023.011>
- Wallace, L., Lucieer, A., & Watson, C. S. (2014). Evaluating tree detection and segmentation routines on Very High Resolution UAV LIDAR DATA. *IEEE Transactions on Geoscience and Remote Sensing*, 52(12), 7619–7628. <https://doi.org/10.1109/tgrs.2014.2315649>
- Wallace, L., Lucieer, A., Watson, C., & Turner, D. (2012). Development of a UAV-LIDAR system with application to Forest Inventory. *Remote Sensing*, 4(6), 1519–1543. <https://doi.org/10.3390/rs4061519>
- Wallace, R. D., Bergeron, C. T., & Reaser, J. K. (2019). Enabling decisions that make a difference: Guidance for improving access to and analysis of Invasive Species Information. *Biological Invasions*, 22(1), 37–45. <https://doi.org/10.1007/s10530-019-02142-2>
- Wang, L., Zhou, Y., Hu, Q., Tang, Z., Ge, Y., Smith, A., Awada, T., & Shi, Y. (2021). Early detection of encroaching Woody Juniperus virginiana and its classification in multi-species forest using UAS imagery and semantic segmentation algorithms. *Remote Sensing*, 13(10), 1975. <https://doi.org/10.3390/rs13101975>
- Wang, S., Xu, S., Yu, C., Wu, H., Liu, Q., Liu, D., Jin, L., Zheng, Y., Song, J., & He, X. (2022). Obstacle avoidance and profile ground flight test and analysis for plant protection UAV. *Drones*, 6(5), 125. <https://doi.org/10.3390/drones6050125>
- Wargo, C. A., Church, G. C., Glaneueski, J., & Strout, M. (2014). Unmanned Aircraft Systems (UAS) research and future analysis. *2014 IEEE Aerospace Conference*, 1–16. <https://doi.org/10.1109/aero.2014.6836448>
- Weathers, K. C., Cadenasso, M. L., & Pickett, S. T. (2001). Forest edges as nutrient and pollutant concentrators: Potential synergisms between fragmentation, forest canopies, and the atmosphere. *Conservation Biology*, 15(6), 1506–1514. <https://doi.org/10.1046/j.1523-1739.2001.01090.x>
- Weinstein, B. G., Marconi, S., Bohlman, S., Zare, A., & White, E. (2019). Individual tree-crown detection in RGB imagery using semi-supervised Deep Learning Neural Networks. *Remote Sensing*, 11(11), 1309. <https://doi.org/10.3390/rs11111309>
- Weinstein, Ben. G., Graves, S. J., Marconi, S., Singh, A., Zare, A., Stewart, D., Bohlman, S. A., & White, E. P. (2020). *A Benchmark Dataset for Individual Tree Crown Delineation in Co-Registered Airborne RGB, Lidar and Hyperspectral Imagery from the National Ecological Observation Network*. <https://doi.org/10.1101/2020.11.16.385088>
- West Virginia facing worst drought in at least two decades.* NOAA Climate.gov. (2024, September 4). <https://www.climate.gov/news-features/event-tracker/west-virginia-facing-worst-drought-least-two-decades>
- Whittier, W. D., Gerken, H. J., & Zipper, C. E. (2010). Management of Cow-Calf Production on Reclaimed Surface-Mined Land. *Virginia Cooperative Extension*.
- Wickham, J. D., Riitters, K. H., Wade, T. G., Coan, M., & Homer, C. (2006). The effect of Appalachian mountaintop mining on Interior Forest. *Landscape Ecology*, 22(2), 179–187. <https://doi.org/10.1007/s10980-006-9040-z>
- Wickham, J., Wood, P. B., Nicholson, M. C., Jenkins, W., Druckenbrod, D., Suter, G. W., Strager, M. P., Mazzarella, C., Galloway, W., & Amos, J. (2013). The overlooked terrestrial impacts of mountaintop mining. *BioScience*, 63(5), 335–348. <https://doi.org/10.1525/bio.2013.63.5.7>
- Wood, D. J., Preston, T. M., Powell, S., & Stoy, P. C. (2022). Multiple UAV flights across the growing season can characterize fine scale phenological heterogeneity within and among vegetation functional groups. *Remote Sensing*, 14(5), 1290. <https://doi.org/10.3390/rs14051290>
- Yang, S., Zheng, Y., & Liu, X. (2019). Research status and trends of downwash airflow of spray uavs in agriculture. *International Journal of Precision Agricultural Aviation*, 2(1), 1–8. <https://doi.org/10.33440/j.ipaa.20190201.0023>
- Yi, Z., Jia, L., & Chen, Q. (2020). Crop classification using multi-temporal sentinel-2 data in the Shiyang River basin of China. *Remote Sensing*, 12(24), 4052. <https://doi.org/10.3390/rs12244052>
- Zeng, L., Wardlow, B. D., Xiang, D., Hu, S., & Li, D. (2020). A review of vegetation phenological metrics extraction using time-series, Multispectral Satellite Data. *Remote Sensing of Environment*, 237, 111511. <https://doi.org/10.1016/j.rse.2019.111511>
- Zhen, Z., Quackenbush, L., & Zhang, L. (2016). Trends in automatic individual tree crown detection and delineation—evolution of LIDAR Data. *Remote Sensing*, 8(4), 333. <https://doi.org/10.3390/rs8040333>

- Zipper C. E. (2020). Appalachian Coal Data. University Libraries, Virginia Tech. Dataset.  
<https://doi.org/10.7294/bda6-7r15>
- Zipper, C. E., Burger, J. A., McGrath, J. M., Rodrigue, J. A., & Holtzman, G. I. (2011a). Forest restoration potentials of coal-mined lands in the Eastern United States. *Journal of Environmental Quality*, 40(5), 1567–1577.  
<https://doi.org/10.2134/jeq2011.0040>
- Zipper, Carl E., Adams, M. B., & Skousen, J. (2020). The Appalachian coalfield in historical context. *Appalachia's Coal-Mined Landscapes*, 1–26. [https://doi.org/10.1007/978-3-030-57780-3\\_1](https://doi.org/10.1007/978-3-030-57780-3_1)
- Zipper, Carl E., Burger, J. A., Skousen, J. G., Angel, P. N., Barton, C. D., Davis, V., & Franklin, J. A. (2011b). Restoring forests and associated ecosystem services on Appalachian Coal Surface Mines. *Environmental Management*, 47(5), 751–765. <https://doi.org/10.1007/s00267-011-9670-z>